

---


Electronic Theses and Dissertations, 2004-2019

---

2004

## Monolithic Integration Of Dual Optical Elements On High Power Semicond

Laurent Vaissie  
*University of Central Florida*

 Part of the [Electromagnetics and Photonics Commons](#), and the [Optics Commons](#)  
Find similar works at: <https://stars.library.ucf.edu/etd>  
University of Central Florida Libraries <http://library.ucf.edu>

This Doctoral Dissertation (Open Access) is brought to you for free and open access by STARS. It has been accepted for inclusion in Electronic Theses and Dissertations, 2004-2019 by an authorized administrator of STARS. For more information, please contact [STARS@ucf.edu](mailto:STARS@ucf.edu).

---

### STARS Citation

Vaissie, Laurent, "Monolithic Integration Of Dual Optical Elements On High Power Semicond" (2004).  
*Electronic Theses and Dissertations, 2004-2019*. 253.  
<https://stars.library.ucf.edu/etd/253>

MONOLITHIC INTEGRATION OF DUAL OPTICAL ELEMENTS  
ON HIGH POWER SEMICONDUCTOR LASERS

by

LAURENT VAISSIE

Diplôme d'Ingénieur, Ecole Nationale Supérieure de Physique de Marseille, 1998  
M.Sc. Optics, University of Central Florida, 2001

A dissertation submitted in partial fulfillment of the requirements  
for the degree of Doctor of Philosophy  
in the College of Optics and Photonics  
at the University of Central Florida  
Orlando, Florida

Fall Term  
2004

## ABSTRACT

This dissertation investigates the monolithic integration of dual optical elements on high power semiconductor lasers for emission around 980nm wavelength. In the proposed configuration, light is coupled out of the AlGaAs/GaAs waveguide by a low reflectivity grating coupler towards the substrate where a second monolithic optical element is integrated to improve the device performance or functionality. A fabrication process based on electron beam lithography and plasma etching was developed to control the grating coupler duty cycle and shape. The near-field intensity profile outcoupled by the grating is modeled using a combination of finite-difference time domain (FDTD) analysis of the nonuniform grating and a self-consistent model of the broad area active region. Improvement of the near-field intensity profile in good agreement with the FDTD model is demonstrated by varying the duty cycle from 20% to 55% and including the aspect ratio dependent etching (ARDE) for sub-micron features. The grating diffraction efficiency is estimated to be higher than 95% using a detailed analysis of the losses mechanisms of the device. The grating reflectivity is estimated to be as low as  $2 \cdot 10^{-4}$ . The low reflectivity of the light extraction process is shown to increase the device efficiency and efficiently suppress lasing oscillations if both cleaved facets are replaced by grating couplers to produce 1.5W QCW with 11nm bandwidth into a single spot a few mm above the device. Peak power in excess of

30W without visible COMD is achieved in this case. Having optimized, the light extraction process, we demonstrate the integration of three different optical functions on the substrate of the surface-emitting laser. First, a 40 level refractive microlens milled using focused ion beam shows a twofold reduction of the full-width half maximum 1mm above the device, showing potential for monolithic integration of coupling optics on the wafer. We then show that differential quantum efficiency of 65%, the highest reported for a grating-coupled device, can be achieved by lowering the substrate reflectivity using a 200nm period tapered subwavelength grating that has a grating wavevector oriented parallel to the electric field polarization. The low reflectivity structure shows trapezoidal sidewall profiles obtained using a soft mask erosion technique in a single etching step. Finally, we demonstrate that, unlike typical methods reported so far for in-plane beam-shaping of laser diodes, the integration of a beam-splitting element on the device substrate does not affect the device efficiency. The proposed device configuration can be tailored to satisfy a wide range of applications including high power pump lasers, superluminescent diodes, or optical amplifiers applications.

*To my wife Pauline who offered me an unwavering support and unconditional love throughout this journey. You are the source of my inspiration and my strength.*

## ACKNOWLEDGMENTS

This work would not have been possible without the help of many individuals I had a chance to meet during the completion of this work. I would first like to thank Dr M.G. “Jim” Moharam and my advisor Dr Eric G. Johnson for facilitating my transition from graduate studies in France to the PhD program at the College of Optics and Photonics four years ago. I am grateful to my advisor for giving me the unique opportunity to work on such an exciting and challenging project and for believing in me from the start. His great efforts to create a state-of-the-art facility in only four years at CREOL made all our work possible. I am thankful to the Defense Advanced Research Projects Agency (DARPA) who funded us for this project through the FLAME and PHOENICS programs and always believed in this technology. I am strongly indebted to Dr Oleg Smolski for the crucial contribution he made to this work by testing most of the devices I designed and fabricated as well as numerous fruitful discussions on device performance. It was a pleasure to team up with somebody so dedicated, passionate and thorough. I would also like to thank Eli Weiss, Hailong Zhou and Greg Zazarra from Coherent Inc. who provided us with some of the best semiconductor laser material available today and who have always expressed interest and support for our work. I am thankful to Mike Devre, Yao-Sheng Lee and David Johnson from Unaxis USA for providing their expert advice on etching and deposition processes. I would like

to thank the members of the Microphotonics laboratory for their help and positive attitude, especially Alok Metha, my laboratory partner for four years, who has been the primary witness of my research maturation process. I am grateful to all the graduate students and staff at CREOL and the Cornell Nanofabrication Facility who helped me during the long hours passed in the cleanroom, including Daniel May-Arrijoja, Robert Illic, Roberto Panepucci, Javier Gonzalez and many others. Finally, last but not least, I would like to thank my family and friends for their never-ending support and cheers.

## TABLE OF CONTENTS

<b>LIST OF FIGURES.....</b>	<b>XII</b>
<b>LIST OF TABLES.....</b>	<b>XVII</b>
<b>LIST OF ABBREVIATIONS AND ACRONYMS .....</b>	<b>XVIII</b>
<b>CHAPTER 1: INTRODUCTION.....</b>	<b>1</b>
1.1    BASICS OF SEMICONDUCTOR LASERS.....	3
1.1.1 <i>The p-i-n junction .....</i>	<i>3</i>
1.1.2 <i>Basic rate equations.....</i>	<i>5</i>
1.1.3 <i>Operational parameters of interest for high power in-plane lasers .....</i>	<i>7</i>
1.1.4 <i>Beam quality parameters.....</i>	<i>9</i>
1.2    LIMITATIONS OF STANDARD FABRY-PEROT CONFIGURATION.....	10
1.2.1 <i>Beam divergence and coupling to optical waveguides .....</i>	<i>10</i>
1.2.2 <i>Catastrophic optical mirror damage (COMD).....</i>	<i>11</i>
1.2.3 <i>COMD improvement using a grating coupler mode transformer.....</i>	<i>14</i>
1.2.4 <i>Conclusion.....</i>	<i>16</i>
1.3    OVERVIEW OF GRATING-COUPLED LASERS RESEARCH.....	17
1.3.1 <i>Towards high efficiency, high power and high brightness devices.....</i>	<i>17</i>
1.3.2 <i>Integration of beam-forming capability with a grating coupler .....</i>	<i>20</i>



1.3.3	<i>Conclusion</i> .....	21
1.4	HIGH POWER DUAL OPTICS SURFACE EMITTING LASER AND AMPLIFIER.....	22
1.4.1	<i>Integration of optical elements on surface-emitting device substrate</i> .....	22
1.4.2	<i>Scope of the dissertation</i> .....	23
<b>CHAPTER 2: NUMERICAL MODELING AND DESIGN .....</b>		<b>25</b>
2.1	SEMICONDUCTOR DEVICE STRUCTURE .....	25
2.1.1	<i>Finite element method analysis of a waveguide structure</i> .....	25
2.1.2	<i>AlGaAs/GaAs Grinsch structure</i> .....	27
2.1.3	<i>Fabry-Perot device performance</i> .....	29
2.1.4	<i>Self-consistent modeling of the broad stripe laser and amplifier</i> .....	30
2.1.4.1	Wave propagation.....	31
2.1.4.2	Numerical implementation by FD-BPM .....	34
2.1.4.3	Solution of the carrier density equation .....	35
2.1.4.4	Thermal effects .....	40
2.2	NUMERICAL MODELING OF AN INTEGRATED GRATING COUPLER .....	41
2.2.1	<i>Grating coupler basic mechanism</i> .....	41
2.2.2	<i>Perturbation technique analysis</i> .....	43
2.2.3	<i>Finite-difference time domain modeling</i> .....	51
2.2.3.1	Numerical Implementation .....	51
2.2.3.2	Modeling of metallic layers .....	53
2.3	GRATING COUPLER DESIGN AND ANALYSIS .....	57
2.3.1	<i>What is the optimum shape for a grating coupler?</i> .....	57
2.3.2	<i>Choice of the grating period</i> .....	59
2.3.3	<i>Theoretical reflectivity of detuned grating coupler</i> .....	60

2.3.4	<i>Effect of low reflectivity mirror on device performance</i> .....	62
2.3.5	<i>Low reflectivity wet-etched structure</i> .....	65
2.3.6	<i>Improvement of grating coupler directionality</i> .....	67
2.3.6.1	FDTD calculation .....	67
2.3.6.2	Experiment .....	69
<b>CHAPTER 3: FABRICATION</b> .....		<b>71</b>
3.1	LASER DIODE FABRICATION .....	71
3.1.1	<i>p-contact processing</i> .....	72
3.1.2	<i>n-contact processing</i> .....	74
3.2	GRATING COUPLER FABRICATION .....	78
3.2.1	<i>Electron beam lithography (EBL)</i> .....	79
3.2.1.1	Electron beam direct-write basic principles .....	79
3.2.1.2	LEO 360 with NPGS versus Leica EBPG 5000+ .....	80
3.2.1.3	The proximity effect .....	83
3.2.1.4	Defining and writing the grating coupler with the Leica EBPG .....	85
3.2.2	<i>Pattern transfer</i> .....	87
3.2.2.1	Inductively coupled plasma (ICP) etching mechanisms .....	88
3.2.2.2	Etching process for GaAs/AlGaAs .....	90
3.2.2.3	Etching process characterization .....	91
3.2.2.4	Soft mask versus hard mask .....	93
3.2.2.5	Aspect ratio dependent etching (ARDE) .....	96
3.2.2.6	Grating metallization and substrate antireflection coating .....	98
3.3	CONCLUSION .....	102
<b>CHAPTER 4: PERFORMANCE ANALYSIS</b> .....		<b>103</b>

4.1	TESTING SET-UP .....	103
4.2	LOW REFLECTIVITY GCSEL PERFORMANCE .....	104
4.2.1	<i>L-I-V characteristics</i> .....	104
4.2.2	<i>Analysis of grating performance</i> .....	107
4.2.2.1	Substrate losses .....	108
4.2.2.2	Passive region losses.....	109
4.2.2.3	Grating efficiency .....	116
4.2.2.4	Estimation of grating effective reflectivity .....	120
4.2.3	<i>Spectral characteristics</i> .....	122
4.2.4	<i>GCSEL Near field and far-field intensity profiles</i> .....	124
4.2.4.1	Near field intensity profile .....	124
4.2.4.2	Far-field profile.....	128
4.2.5	<i>High peak power performance</i> .....	130
4.3	CROSSED-BEAM SUPERLUMINESCENT DIODE (X-SLD).....	131
4.3.1	<i>Device performance</i> .....	132
4.3.2	<i>Influence of stripe geometry on device performance</i> .....	135
4.3.3	<i>High peak power performance</i> .....	140
4.4	CONCLUSION .....	141
<b>CHAPTER 5: INTEGRATION OF BACKSIDE OPTICAL ELEMENT .....</b>		<b>144</b>
5.1	MONOLITHIC LENS INTEGRATION BY FOCUSED ION BEAM (FIB).....	144
5.1.1	<i>Lens fabrication</i> .....	146
5.1.2	<i>Device performance</i> .....	149
5.2	TAPERED SUBWAVELENGTH ANTIREFLECTION COATING .....	153
5.2.1	<i>Tapered 1D subwavelength grating (SWG)</i> .....	154

5.2.2	<i>Fabrication</i> .....	161
5.3	<i>Device performance</i> .....	164
5.3	FAN-OUT ELEMENT.....	167
5.3.1	<i>Design and fabrication</i> .....	169
5.3.2	<i>Performance</i> .....	172
<b>CHAPTER 6: CONCLUSIONS</b> .....		<b>174</b>
6.1	SUMMARY OF THE CONTRIBUTIONS PRESENTED IN THIS DISSERTATION.....	174
6.1.1	<i>High efficiency grating coupler with low effective reflectivity</i> .....	174
6.1.2	<i>Device performance improvement using backside optical element</i> .....	175
6.1.3	<i>Numerical modeling and analysis</i> .....	177
6.1.4	<i>Device applications</i> .....	178
6.2	FUTURE PERSPECTIVES.....	178
6.2.1	<i>Efficiency</i> .....	179
6.2.2	<i>Brightness</i> .....	179
6.3	<i>Backside micro-optical elements</i> .....	182
<b>APPENDIX A: FDTD NUMERICAL FORMULAE</b> .....		<b>184</b>
<b>APPENDIX B: TESTING SET-UP</b> .....		<b>190</b>
<b>LIST OF REFERENCES</b> .....		<b>192</b>

## LIST OF FIGURES

Fig.1: Schematic description of a p-i-n homojunction. a) Energy band diagram with $V = 0$ , b) forward bias $V = \frac{h\nu}{q}$ , c) Built-in refractive index for waveguiding. ....	3
Fig.2: Recombination mechanisms involved in a semiconductor laser diode. ....	4
Fig.3: Typical L-I-V curve of a laser diode. The external differential quantum efficiency and series resistance are defined on the diagram. ....	8
Fig.4: Optical (left) and SEM (right) picture of COMD obtained on uncoated facet of an AlGaAs/GaAs Fabry-Perot laser for an intensity of $3.2\text{MW}/\text{cm}^2$ . ....	13
Fig.5: Surface-emitting laser diode with dual optical elements. Light is outcoupled by a low reflectivity grating coupler. The device substrate is used to improve the device performance and functionality using monolithic integration of optical elements. We demonstrate the integration of a refractive lens, a beam-splitter and a subwavelength antireflection structure. ....	24
Fig.6: Electric field amplitude distribution of the fundamental mode in the designed structure (left). The intensity distribution is compared to the intensity profile propagating in a standard high power laser diode structure (right). ....	28
Fig.7: Influence of the number of terms on a typical profile affected by the optical mode intensity distribution. $\epsilon=10^{-5}$ . The optical power is 20mW. The current density is $1\text{kA}/\text{cm}^2$ . ....	38
Fig.8: Polynomial fit of logarithmic expression for gain of quantum well obtained from [Eriksson 1998]. ....	39
Fig.9: GCSEL general configuration and equivalent wave-vector diagram. ....	42
Fig.10: Radiation losses introduced by a uniform grating coupler. ....	44
Fig.11: Plot of outcoupling length ( $\mu\text{m}$ ) versus grating depth and duty cycle for a rectangular grating coupler predicted by the perturbation technique model. ....	49
Fig.12: Outcoupling length for a 50% duty cycle grating coupler obtained by finite-difference time domain and perturbation technique. ....	50
Fig.13: The Yee cell showing how $H_x$ and $H_z$ are interleaved with $E_y$ to yield accurate numerical derivatives of the magnetic field involved in the calculation of the electric field. ....	52
Fig.14: Benchmark of the lossy dielectric FDTD showing a comparison between theoretical behavior of E-field in lossy medium and FDTD simulation. ....	53
Fig.15: Plot of outcoupling length versus sidewall angle $\theta$ obtained by FDTD modeling. ....	58

Fig.16: Reflectivity of a 100micron long, 50% duty cycle, 250nm deep, 270nm period grating coupler as a function of wavelength. At the emission wavelength of 977nm, the reflectivity is less than $10^{-4}$ .....	61
Fig.17: Plot of the Fabry-Perot device efficiency versus output mirror reflectivity for different lengths of 1mm, 2mm, and 4mm. ....	63
Fig.18: Plot of carrier density (bottom) and electric field intensity (top) inside the cavity of 2mm long by 60 $\mu$ m wide device for I=1A obtained after 19 iteration loops by averaging 5 loops. ....	64
Fig.19: Scanning electron microscope of the wet-etched transition between the active and the passive area where the grating is integrated. ....	66
Fig.20: Intensity profile of the guided mode in the active and passive region obtained by finite element method (left) and FDTD propagation of E field through the modeled wet-etched transition (right). ....	66
Fig.21: Horizontal component of the power flow representing the decay of propagating power inside the waveguide when the grating coupler is coated with gold only (right) or a combination of dielectric and gold layers (left). ....	68
Fig.22: Wet-etch sidewalls profiles of GaAs with respect to the major flats (top). The flats configuration shown is US standard (source: Tyco Electronics). ....	73
Fig.23: p-contact processing prior to grating coupler integration. ....	74
Fig.24: Polishing mechanism of GaAs by NaOCL and ZYGO white light interferometer profiles of GaAs substrate before and after polishing. ....	75
Fig.25: SEM picture of negative resist profile after development and metallization (left) and microscope picture of gold marls used for front to backside alignment (right). ....	77
Fig.26: Elements of an EBL column (example of Leica Vectorbeam writer). ....	80
Fig.27: Proximity effect on densely packed lines. The left SEM show a cross section of patterns written in 400nm thick PMMA. The grating duty cycle on the edge of the pattern is affected by the proximity effect (right). ....	84
Fig.28: Clearing dose as a function of CAD linewidth for a 270nm period grating. The wider features typically require a lower dose to clear because of the proximity effect. The resist used is ZEP 2:1 spun at 3500RPM for 40s. ....	84
Fig.29: CAD design of a 16 level graded grating coupler and SEM of a device with a grating coupler patterned in ZEP. The exposure dose increases from z=0 to z=80 $\mu$ m. ....	86
Fig.30: Diagram of an inductively-coupled plasma source (modified from Unaxis [Unaxis 2003]). ....	89
Fig.31: Etching mechanism of GaAs in BCl <sub>3</sub> /N <sub>2</sub> /Ar chemistry. ....	90
Fig.32: AlGaAs/GaAs etching process parameters for anisotropic etching of submicron features. The Zygo profile of the etched GaAs surface shows a very smooth surface (RMS roughness<1nm) resulting from the high density, low-energy plasma generated by the ICP source for RIE powers of 60W to 100W. ....	92
Fig.33: Typical slanted profile in Si <sub>3</sub> N <sub>4</sub> obtained from standard CF <sub>4</sub> RIE etching using PMMA	

mask. The mask was removed before SEM inspection. ....	94
Fig.34: Etched dielectric sidewalls profile comparison between PMMA (left) and ZEP 520 (right) mask after anisotropic RIE using CHF <sub>3</sub> for passivation of the sidewalls. ....	94
Fig.35: SEM of sidewalls profiles obtained using hard (left) and soft mask (right). The erosion of the soft resist mask compensates for the bowing effect. The drawing is modified from [Hagberg 1994]. ....	96
Fig.36: Characterization of aspect ratio dependent etching in AlGaAs using ZEP resist as a mask (removed before SEM). ....	98
Fig.37: Grating coupler metallization scheme. ....	99
Fig.38: Index of refraction of PECVD grown films versus NH <sub>3</sub> gas flow. Gas flow 1=4sccm, gas flow 2= 6sccm, gas flow 3=8sccm. The lowest reflectivity is obtained for a film of index close to 1.78 which corresponds to 8sccm NH <sub>3</sub> gas flow. ....	100
Fig.39: SEM of typical grating profile with high reflection coating. The nonconformal coating of the dielectric layer produces a “keyhole” feature in the profile which may cause some additional scattering losses. ....	101
Fig.40: Typical L-I-V curve for a 2mm long, 60μm wide stripe GCSEL with AR dielectric coating on the substrate. ....	105
Fig.41: Lasing threshold current densities for 2mm long GCSEls with HR/AR coatings on grating and substrate respectively. The cleaved facet is left uncoated. ....	106
Fig.42: Linear fitting of transmission through n-doped GaAs substrate. ....	108
Fig.43: Device configuration for characterization of passive losses. The exponential gain and losses are taken into account for the derivation of the external differential efficiency. The effective reflectivity between active and passive region is neglected. ....	111
Fig.44: Theoretical (plot) and experimental (table) external differential efficiency as a function of passive region loss coefficient $\alpha_p$ . The loss coefficient is estimated to be between 2.8 and 5 cm <sup>-1</sup> . ....	113
Fig.45: Near-field intensity profiles at different current levels highlighting the saturable absorption of the quantum well. Weak coupling was obtained with a 200nm deep grating with low duty cycle to investigate the passive region losses at low power levels more accurately. ....	115
Fig.46: Typical optical power measured from the various device outputs before integration of the grating and substrate coatings. The power measured at output #3 is negligible. The grating duty cycle varies from 20% to 55% on 80μm for a maximum depth of 275nm. ....	118
Fig.47: Typical normalized spectrum for a 2mm long GCSEL as a function of pumping current. The resolution of the spectrum analyzer for this measurement is 0.2nm. The pulse width is 500ns and the repetition rate is 1kHz. ....	123
Fig.48: Effect of ARDE on grating decay coefficient $\alpha$ . The coupling between grating depth and linearly increasing duty cycle produces a slow rising coupling coefficient which produces nearly symmetric near-field intensity profile. ....	125
Fig.49: Experimental near-field intensity profiles from gratings with uniform versus graded duty	

cycle. The duty cycle is varied from 20% to 55%, the grating depth varies accordingly from 210nm to 275nm. ....	126
Fig.50: Near-field intensity profile obtained by finite-difference time domain compared to experimental data. ....	127
Fig.51: Intensity profile modeling of a 2mm long, 60 $\mu\text{m}$ wide GCSEL inside the active region (left) and along the grating (right) for 1A pumping current. ....	128
Fig.52: Far-field profile of 2mm GCSEL at 600mA CW pumping current. The divergence angle in the X direction is affected by the multimode behavior of the broad area device while the amplified spontaneous emission bandwidth controls the divergence angle in the Y direction. ....	129
Fig.53: High peak power operation of a 2mm GCSEL. Maximum power is limited by catastrophic optical damage occurring on the uncoated cleaved facet. ....	130
Fig.54: Schematic of the crossed-beam superluminescent diode (X-SLD). The low reflectivity nonresonant gratings prevent lasing oscillation in the cavity. The grating is metallized to increase efficiency through the substrate. ....	132
Fig.55: L-I curve of a 2mm X-SLD. The bandwidth of the device remains approximately constant up to the apparition of the lasing oscillations above 4A. ....	133
Fig.56: Spatial profile of the overlapped beams captured at 4.7mm above the 2mm long device for 300mA pumping current. ....	135
Fig.57: Peak power as a function of current density (left) and differential quantum efficiency for various cavity lengths of 1mm, 2mm, and 4mm (right). ....	137
Fig.58: Spectrum of a 1mm, 2mm and 4mm long X-SLD for a current density of 1.66kA/cm <sup>2</sup> . The current pulse width is 500nS, repetition rate of 1kHz. The coefficient $\beta$ can then be derived geometrically and is given by [Zhao 1999]. ....	139
Fig.59: High current performance of a 4mm long device with two grating couplers. Thermal effects limit the power to 32W for 60A current. The large grating coupler emitting area eliminates catastrophic optical mirror damage. Above 3.5A, many lasing oscillations can be observed. ....	141
Fig.60: Focused ion beam FEI 200TEM column showing milling and imaging mechanisms (source Alan Kubis, University of Virginia). ....	146
Fig.61: Quantization of the lens for fixed depth increment. ....	148
Fig.62: SEM picture of the device substrate with the integrated microlens and 3D white light interferometer profile of the fabricated lens. ....	149
Fig.63: Full-width half-maximum variation of the intensity profile with respect to distance from the lens (left). The four level contour images captured with (bottom right) and without the lens (top right) after 1mm propagation illustrate the focusing effect of the fabricated microlens. ....	151
Fig.64: Diagram of subwavelength grating integrated on the device substrate. ....	153
Fig.65: Diagram of trapezoidal 1D grating and equivalent film-stack of gradient refractive index. The polarization direction and the incident angle are set by the grating coupler. ....	154



Fig.66: Index of refraction of the effective medium as a function of the fill factor. ....	157
Fig.67: Reflectivity versus SWG depth for two orientations of the grating grooves. The profile is triangular approximated by 200 layers. A minimum reflectivity of $3.5 \times 10^{-4}$ is estimated for a depth of 325nm. ....	159
Fig.68: Reflectivity versus SWG depth for various trapezoidal profiles for $E // K$ configuration. The geometry of the SWG is defined in Fig.65. ....	160
Fig.69: Reflectivity versus wavelength for a triangular profile. The SWG depth is set to $d=320\text{nm}$ and $E // K$ . The effect of the spatial dispersion introduced by the grating coupler is also shown for $\Lambda_g = 270\text{nm}$ . ....	160
Fig.70: SEM pictures of tapered grating transfer in GaAs. The slope created by the mask erosion, shown after 40s of etching, is transferred into the substrate as the etching progresses to create the desired trapezoidal profile. ....	163
Fig.71: Light-current characteristics for GCSEL devices with and without antireflection subwavelength grating. The devices were tested with $1\mu\text{s}$ pulse current pulses at 100kHz repetition rate. ....	165
Fig.72: Diagram of the fan-out integration on the backside of a GCSEL. The fan-out element is a $1.4\mu\text{m}$ period grating etched in GaAs at a depth of 105nm. An SEM profile of the fabricated grating is shown in the inset. ....	168
Fig.73: Phase profile introduced by the fan-out element. ....	169
Fig.74: Diffracted power ratio between +1 and zero <sup>th</sup> order. The depth is corrected by the angle of incidence in the substrate of $4.5^\circ$ . The calculation is based on scalar theory for a $1.4\mu\text{m}$ rectangular grating and 970nm emission wavelength. ....	171
Fig.75: L-I curve for the three diffracted spots. The device was tested with a 500ns pulse at a 1kHz repetition rate. The intensity profile shown in inset was captured 1.36cm above the substrate by imaging a diffuser. The +1 and -1 order spots appear distorted due to the large divergence angle projection. ....	173
Fig.76: Optical intensity distribution under flared contact stripe for 1A pumping current. The structure consists of a $10\mu\text{m}$ wide, $500\mu\text{m}$ long rectangular stripe followed by a $1.5\text{mm}$ long flared stripe corresponding to a $3.43$ degrees taper angle. ....	180
Fig.77: Plot of leakage rate versus distance and corresponding $100\mu\text{m}$ width Gaussian output intensity profile. ....	181
Fig.78: Prism angle needed to obtain vertical emission from the substrate. ....	182
Fig.79: Diagram of testing set-up. The output from the surface-emitting device is captured for spectral, power, and spatial beam profile measurements. ....	191

## LIST OF TABLES

Table 1: Degraded part, cause, and main enhancement factor in LEDs and Lasers [Fukuda 1991]. .....	12
Table 2: Comparison of Catastrophic Optical Damage level for large optical cavity and GCSEL structure compared to standard high power GRINSCH structure. ....	15
Table 3: AlGaAs/GaAs GRINSCH structure grown by Coherent Inc. The substrate is thinned down to a thickness 150 $\mu$ m.....	28
Table 4: Structure parameters calculated or taken from literature for standard InGaAs structure. These parameters can then be plugged in the modeling tool described in paragraph 2.1.4..	33
Table 5: Experimental comparison of high reflection coating performance. ....	70
Table 6: Typical process used to remove Si <sub>3</sub> N <sub>4</sub> dielectric layer before grating integration. ....	78
Table 7: Comparison between SEM based NPGS system and Leica EBPG 5000+.....	82
Table 8: Process parameters used to deposit SiNH in PECVD chamber provided by Unaxis Inc.. .....	100
Table 9: Grating efficiency versus fabrication methods and grating parameters. The grating efficiency is estimated using an analysis of the losses mechanisms.....	119
Table 10: Effective grating reflectivity estimated from the facet output power measurements. All the other device parameters are identical. The power at the beginning of the grating $P_g$ is assumed to be 1.1W for all devices at 1A of pumping current.....	121

## LIST OF ABBREVIATIONS AND ACRONYMS

$\mathfrak{R}$	Ensemble of real numbers
$\mathbb{N}$	Ensemble of natural integers
$\mathbb{N}^*$	Ensemble of natural integers minus zero
$\mathbb{Z}$	Ensemble of positive and negative integers including zero
$\mathfrak{R}^+$	Ensemble of positive real numbers including zero
$\mathfrak{R}^*$	Ensemble of real numbers minus zero
AR	Antireflection
CCD	Charge-Coupled Detector
COMD	Catastrophic optical mirror damage
CW	Continuous Wave
dB	Decibels
DOE	Diffractive Optical Element
DQE	Differential Quantum Efficiency
EBPG	Electron Beam Pattern Generator
ECR	Electron Cyclotron Resonance
FD-BPM	Finite Difference Beam Propagation Method
FDTD	Finite Difference Time Domain
FIB	Focused Ion Beam
FP	Fabry-Perot
FWHM	Full Width Half Maximum
GCSEL	Grating-coupled Surface Emitting Laser
GCSOA	Grating-Coupled Semiconductor Optical Amplifier
GRINSCH	Graded index separate confinement heterostructure
HR	High Reflection
ICP	Inductively-Coupled Plasma
IPA	Isopropanol
LOC	Large Optical Cavity
MOPA	Master Oscillator Power Amplifier
NPGS	Nabity Pattern Generator System
PML	Perfectly Matched Layer
PMMA	Poly(methyl methacrylate)
QCW	Quasi-Continuous Wave

RMS	Root Mean Square
SOA	Semiconductor Optical Amplifier
TE	Transverse Electric Field polarization
TM	Transverse Magnetic Field polarization
VCSEL	Vertical Cavity Surface Emitting Laser
X-SLD	Crossed-beam Superluminescent Diode

## CHAPTER 1: INTRODUCTION

Semiconductor lasers have enabled many technologies since their invention in 1962 [Basov 1962, Bernard 1962]. Their unique properties enable the emission, amplification and modulation of light for various optical systems. Their compact size, electrical pumping and modulation capabilities, as well as high gain make semiconductor lasers the ideal candidates for being the building block of optical integrated circuits or compact high power systems. Photonics integrated circuits already integrate laser diode sources with elements such as distributed Bragg reflectors, modulators and detectors [Coldren 1995]. In order to complete the chip integration and eliminate bulk optics, the transition from device to free-space must be properly designed to couple the output of the semiconductor diode to other optical components such as waveguides, detectors, or various pumped medium depending on applications. However the output of edge-emitting devices typically suffers from high divergence and astigmatism. Recently, technological improvements have made the integration of complex functions on a single chip possible by diffractive optical elements fabricated using wafer-based micro-fabrication techniques [Larsson 1999]. However, the output power of such devices is typically very limited or the efficiency is very low [Feng 1999, Modh 2003].

In this dissertation, we explore a semiconductor optical device configuration based on a non-resonant diffraction grating coupler with monolithic integration of beam-shaping elements on the

substrate for high power applications at 980nm emission wavelength. The proposed device constitutes a versatile platform suitable for efficient high-power operation, virtuously eliminating catastrophic optical damage typically associated with edge emitting devices while increasing its functionality by enabling monolithic integration of optical functions directly on the chip without efficiency penalty. The organization of the dissertation is as follows. In this chapter, we will first review the basic mechanisms and characterization parameters of a semiconductor laser before discussing the fundamental limitations of the standard Fabry-Perot configurations and the benefits of the dual optics integration of a grating coupler on the p-side and optical elements on the substrate of the device. In the second chapter, the numerical models used to design the waveguide structure and model the active and passive components of the device will be detailed. The fabrication process flow of the grating-coupled surface emitting device will be outlined in chapter 3. The performance analysis will be carried out in chapter 4 to evaluate the grating efficiency and as well as the main losses mechanisms. Finally, we will demonstrate in chapter 5 the integration of three optical elements on the device substrate for focusing, splitting or increasing the device extraction efficiency.

## 1.1 Basics of semiconductor lasers

### 1.1.1 The p-i-n junction

The device is based on a forward biased p-i-n junction shown in Fig.1. The optical gain is provided by electron-hole recombination and the optical feedback is created by cleaved facets in its basic Fabry-Perot (FP) configuration.

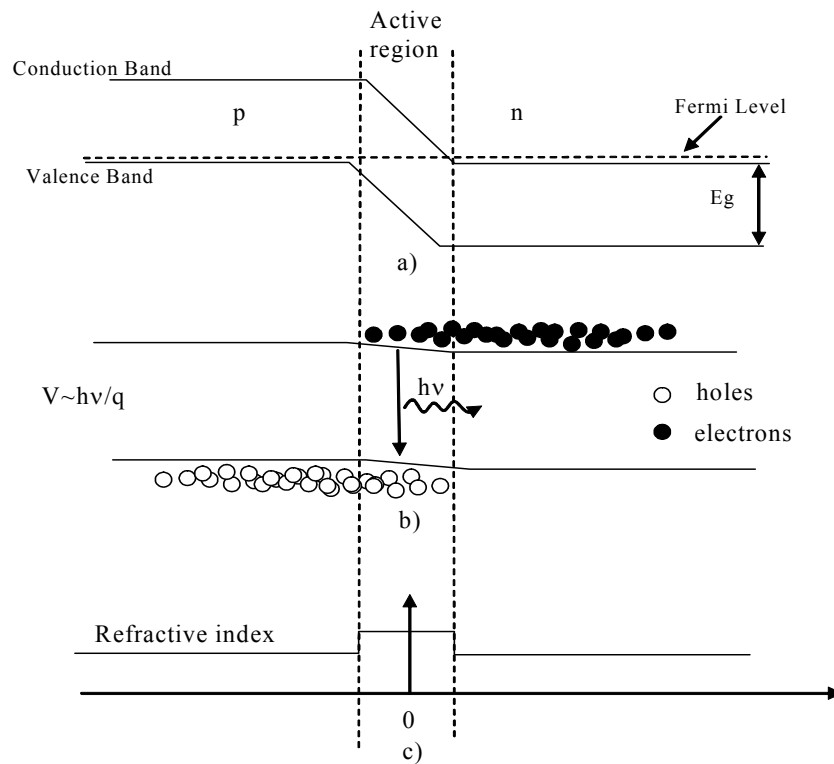


Fig.1: Schematic description of a p-i-n homojunction. a) Energy band diagram with  $V = 0$ , b) forward bias  $V = \frac{h\nu}{q}$ , c) Built-in refractive index for waveguiding.

The performance of the semiconductor lasers were greatly enhanced by the addition of an heterostructure using greater bandgap material to confine the optical mode field and carrier concentration in the gain region around the active region, reducing the lasing threshold current and internal absorption losses. The electron-hole recombination produces a photon through the spontaneous or the stimulated emission process as described in Fig.2.

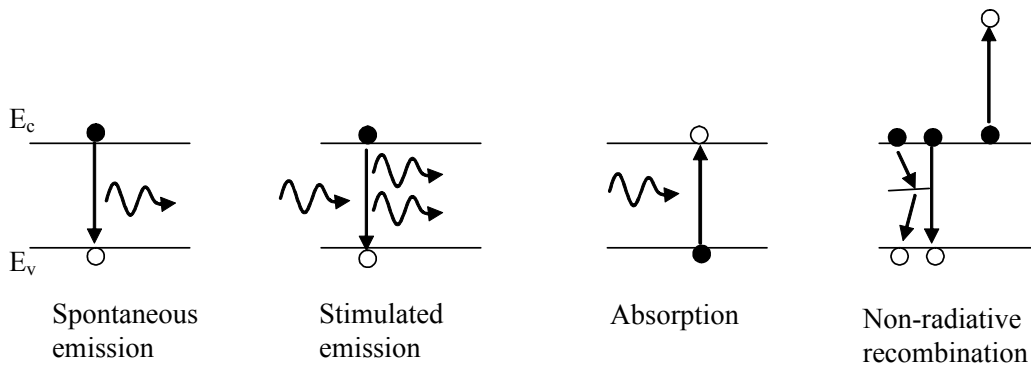


Fig.2: Recombination mechanisms involved in a semiconductor laser diode.

Spontaneous emission creates photons without phase relationships or specific direction. In the stimulated emission mechanism, the electron-hole recombination is triggered by a traveling photon, creating a second photon of same energy, phase and direction. This process, combined with optical feedback, is responsible for coherent emission of light or lasing. When the optical feedback is suppressed, the emission relies on the amplification of the spontaneous emission produced by the device and a broad spectrum is observed due to the lack of coherence of the emitted photons [Lee 1973].



### 1.1.2 Basic rate equations

We showed in Fig.1 how the electrons injected in the active region may recombine to produce photons of energy equal to the bandgap. The electron or carrier density is governed by the general equation

$$\frac{dN}{dt} = \frac{\eta_i I}{qV} - R_{nr} - R_{sp} - R_l - R_{st}, \quad (1.1)$$

where  $\eta_i$  is the internal quantum efficiency,  $I$  the injected current,  $q$  the electron charge and  $V$  the volume of the active region. The recombination terms  $R_{sp}$ ,  $R_{nr}$ ,  $R_l$ , and  $R_{st}$  define the spontaneous emission, non radiative recombination, carrier leakage, and stimulated emission respectively. This equation is also written in the following ways

$$\frac{dN}{dt} = \frac{\eta_i I}{qV} - \frac{N}{\tau} - R_{st} \quad (1.2)$$

where  $\tau$  defines the carrier recombination lifetime, or

$$\frac{dN}{dt} = \frac{\eta_i I}{qV} - \frac{N}{\tau} - \nu_g g N_p = \frac{\eta_i I}{qV} - AN - BN^2 - CN^3 - \nu_g g N_p, \quad (1.3)$$

Where  $\nu_g$  is the group velocity,  $g$  is the gain per unit length,  $N_p$  is the photon density, B the bimolecular recombination rate describing spontaneous emission, and A and C are coefficients describing non-radiative recombination mechanisms. Assuming we know the threshold current  $I_{th}$  needed to overcome the losses in the cavity, the steady state photon density is given by

$$N_p = \frac{\eta_i(I - I_{th})}{qv_g g_{th} V}, \quad (1.4)$$

where  $g_{th}$  is the gain per unit length at threshold defined by

$$g_{th} = \frac{\alpha_i + \alpha_m}{\Gamma} \quad (1.5)$$

Where  $\alpha_i$  is the internal cavity losses,  $\alpha_m$  the mirror losses, and  $\Gamma$  represents the ratio of the active region volume divided by the cavity volume. The output power is then obtained by multiplying the optical energy stored in the cavity multiplied by the energy loss rate at the mirrors, and is given by

$$P = \eta_i \left( \frac{\alpha_m}{\alpha_i + \alpha_m} \right) \frac{h\nu}{q} (I - I_{th}) \quad (1.6)$$

The external differential quantum efficiency is then defined by

$$\eta_d = \eta_i \left( \frac{\alpha_m}{\alpha_i + \alpha_m} \right) \quad (1.7)$$

Or, for  $I > I_{th}$

$$\eta_d = \left( \frac{q}{h\nu} \right) \frac{dP}{dI} \quad (1.8)$$

This quantity defines the number of photons emitted by the laser output as a function of the

number of electrons injected.

### 1.1.3 Operational parameters of interest for high power in-plane lasers

The mirror losses  $\eta_m$ , defined by opposition to the purely internal losses  $\alpha_i$ , are given by

$$\alpha_m = \frac{1}{L} \ln \left( \frac{1}{R_1 R_2} \right) \quad (1.9)$$

It is interesting to note that this term depends on the active length of the device  $L$  and not only the mirrors reflectivity  $R_1$  and  $R_2$ . The internal losses can be defined by

$$\alpha_i = \alpha_{ia} L + \alpha_{ip} L_p \quad (1.10)$$

Where  $L_p$  is the length of a potential passive, unpumped region. The external differential quantum efficiency is then given from (1.7) by

$$\frac{1}{\eta_d} = \frac{\alpha_i}{\eta_i \ln \left( \frac{1}{R_1 R_2} \right)} L + \frac{1}{\eta_i} \quad (1.11)$$

This parameter is a common way of defining the device efficiency but does not include the electric circuit around the laser itself, comprising the junction and metal contacts electrical conductivities and other wire-bonding schemes used to drive laser diodes. In order to assess the actual electrical-to-optical conversion efficiency, the “wall-plug” efficiency was defined as

[Mehuys 1999].

$$\eta_c = \frac{P_{optical}}{P_{electrical}} = \frac{\eta_d (I - I_{th}) \left( \frac{h\nu}{q} \right)}{I \cdot (V_j + R_S I)} \quad (1.12)$$

Where  $V_j$  is the junction voltage defined as  $\frac{h\nu}{q}$  and  $R_s$  the series resistance calculated from the

I-V curve as shown in Fig.3.

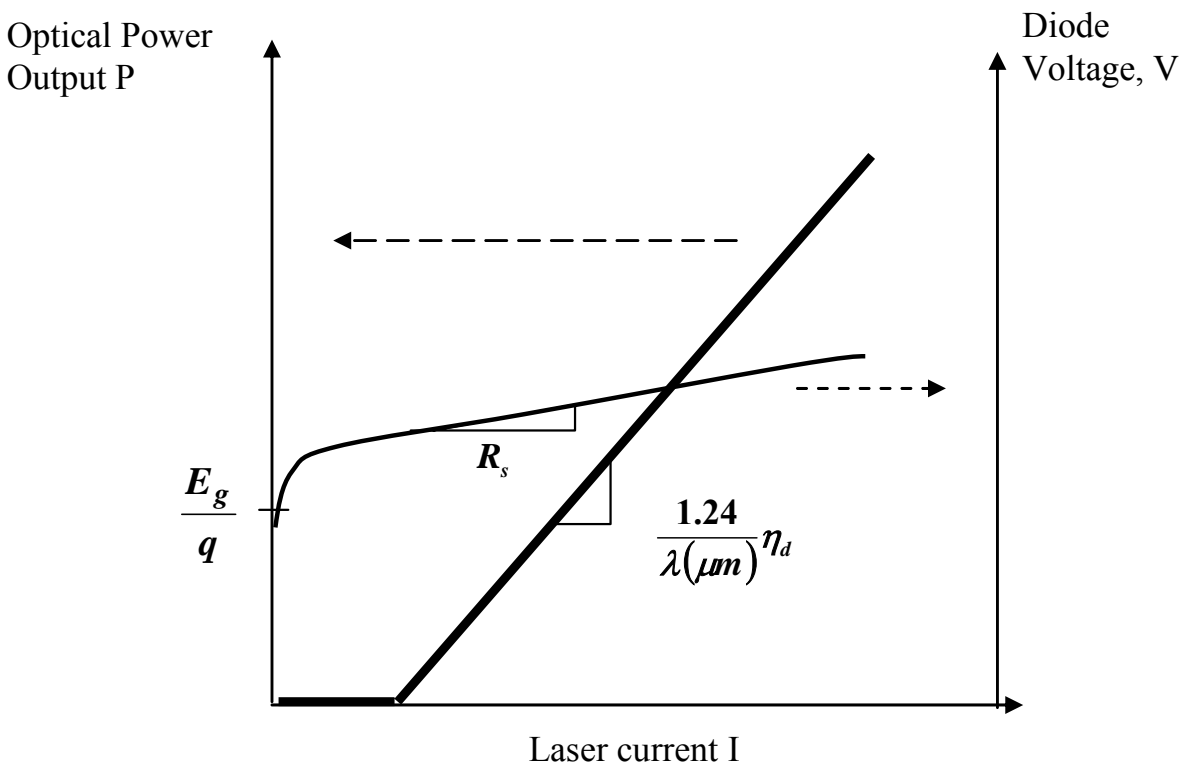


Fig.3: Typical L-I-V curve of a laser diode. The external differential quantum efficiency and series resistance are defined on the diagram.

#### 1.1.4 Beam quality parameters

The quality of an optical source is also evaluated using parameters quantifying the quality of the output beam produced. The photometric brightness, defined as the sum of the time-averaged energy per unit time emerging from a surface  $\delta S$  into a solid angle  $\delta\Omega$  making an angle  $\theta$  with the surface normal can be expressed as [Born 1980]

$$B = \int_{\Omega=0}^{4\pi} \int_S \int_{\theta=0}^{\frac{\pi}{2}} \frac{\delta E}{\cos\theta \delta S \delta\Omega} \quad (1.13)$$

Considering the conservation of energy during propagation, the brightness parameter will be constant throughout propagation. Another beam quality parameter is the  $M^2$  factor. This parameter can be used to characterize spatial multimode beams by looking at the divergence of a beam compared to the diffraction-limited divergence obtained using the beam waist measured at focus. The  $M^2$  method is very useful to characterize optical beams in applications where the light needs to be coupled into a uniform optical waveguide such as an optical fiber, i.e. applications where the ideal spatial profile is close to a gaussian. For special mode matching applications, this technique may not be valid since the desired beam profile may not be a Gaussian but a higher order mode [Vaissie 2002].

## **1.2 Limitations of standard Fabry-Perot configuration**

### **1.2.1 Beam divergence and coupling to optical waveguides**

The divergence of the beam will depend on many laser parameters such as stripe width and lateral index profile. In the plane perpendicular to the junction plane the spatial beam profile is governed by the layers properties (permittivity and thickness) used to confine the optical mode profile in the active region. In the direction parallel to the junction plane the divergence depends mainly on the lateral index variation and the stripe geometry. Typical full width half maximum (FWHM) divergence angles for multimode index guided structures are  $7^\circ \times 35^\circ (\theta_{//} \times \theta_{\perp})$ . This highly divergent and astigmatic beam requires at least two lenses for efficient fiber coupling [Delepine 2002]. The lenses are mostly aligned using an active process, increasing substantially the cost of the final device. Fu proposed to integrate a silicon dioxide ( $\text{SiO}_2$ ) cylindrical lens on the end facet of the laser diode to collimate the beam for 80% direct coupling to single mode fiber [Fu 2000]. However the deposition of  $\text{SiO}_2$  by focused ion beam (FIB) is not wafer-based and therefore is hardly applicable to large production. An alternative approach is to use specialty lensed-fibers. Various configurations have been proposed including fibers with spherical step-index or gradient index profile end, aspheric, tapered, or silica thread on fiber tip [Shiraishi 1995]. The most commonly used lensed fiber to couple high aspect ratio profiles (3 to 5) to single-mode fiber is the wedge-shaped fiber [Yoda 2001]. Although the coupling losses are only

0.15dB at 980nm, such lensed-fiber is limited by its small working distance (6 $\mu$ m) and low tolerance to axial displacement. Another issue is the fabrication cost of such elements and the fabrication technique itself that is not compatible with automated mass-production methods used for semiconductor lasers. A promising approach for low to moderate power is the slab-coupled geometry proposed by Walpole [Walpole 2002]. In this configuration, the mode propagating in the cavity is not confined to the thin quantum well region and coupling efficiency as high as 80 % were reported by simple butt-coupling into a single mode fiber. However, for high power level, this approach may be limited by catastrophic optical damage around 1W of CW optical power.

### **1.2.2 Catastrophic optical mirror damage (COMD)**

Catastrophic failure of the device, also known as catastrophic optical damage (COD) is usually listed as the main limit to power scaling in semiconductor lasers. The different COD mechanisms are outlined in Table 1. We are particularly interested in the facet degradation known as COMD since it is the degradation mechanism that is controlled directly by light. The facet degradation occurs as a result of an oxide film growth on the cleaved facet [Fukuda 1991]. Defects are introduced at the semiconductor/oxide film interface. These defects act as nonradiative recombination centers. The film non-uniformity also makes the facet rougher, increasing scattering and threshold current, decreasing external quantum efficiency. The nonradiative recombination is also responsible for excessive heating of the facet at high optical

power which results in facet degradation by melting. The oxide film thickness is proportional to the square root of the aging time in AlGaAs/GaAs lasers. High optical output power accelerates the film growth and occurrence of COMD. The oxidation is greatly reduced by coating the facets with a dielectric layer such as  $\text{Si}_x\text{O}_y\text{N}_z$ . However the interface coating/semiconductor may itself create defects responsible for catastrophic optical damage. A device with 4%/80% AR/HR coatings typically reaches COMD at an optical power per unit length of  $50\text{mW}/\mu\text{m}$  after a few 100 hours of CW operation [Fukuda 1994].

Table 1: Degraded part, cause, and main enhancement factor in LEDs and Lasers [Fukuda 1991].

<b>PART</b>	<b>CAUSE</b>	<b>MAIN FACTOR</b>
Inner region	Dislocation, precipitation	temperature, current
Facet	Oxidation	<b>Light</b> , moisture
Electrode	Metal diffusion, alloy reaction	Current, ambient temperature
Bonding part	Solder instability (reaction and migration)	Current, temperature
Heat sink	Separation of metal	Temperature, current
Buried Heterostructure (BH)	Defect at BH interface	Current, temperature



Another technique for increasing the COMD level is to fabricate non-absorbing mirrors by a process known as quantum-well intermixing. Using this technique the bandgap of the diode structure is increased at the diode facets. This is done either by locally doping the structure with Si or Zn atoms or by diffusing point defects generated locally at the surface by sputter-deposition of SiO<sub>2</sub>. This method recently showed a 2.6 improvement of COMD level under pulse conditions [Walker 2002]. Significant improvement of the maximum power available was also obtained using a modified epitaxial structure named large optical cavity (LOC). The basic concept is to enlarge the optical mode waist using a broad waveguide structure in order to decrease the energy density at the facet and therefore increase the COMD level.

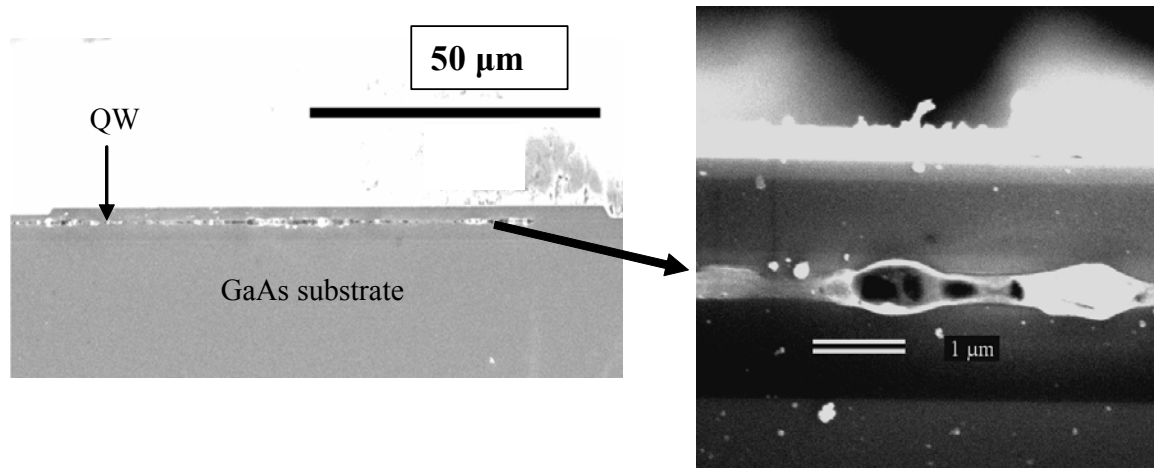


Fig.4: Optical (left) and SEM (right) picture of COMD obtained on uncoated facet of an AlGaAs/GaAs Fabry-Perot laser for an intensity of 3.2MW/cm<sup>2</sup>.

The advantage of this structure is also to decrease the fast axis far-field divergence since it is directly proportional to the square of the beam waist. Such structure produced record output powers greater than 10 W CW in Al-free structures with an internal optical power density at catastrophic optical damage (COMD) of 18MW/cm<sup>2</sup> [Al-Muhanna 1998]. Recently, it was demonstrated that 50W peak power could be obtained from a 100µm wide, 2mm long stripe LOC structure if the device was pulsed with a 40ns pulse [Martinelli 2004]. However, the range of applications of such short pulse pumping is limited and COMD remains the main limiting factor of high power semiconductor laser diodes in most practical cases.

### 1.2.3 COMD improvement using a grating coupler mode transformer

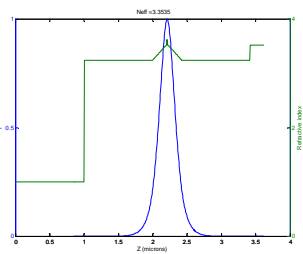
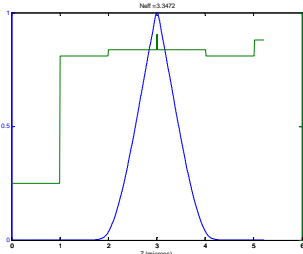
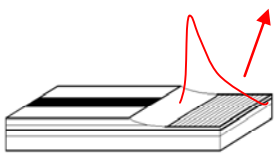
In this section we compare the intensity profiles of the fundamental modes supported in various semiconductor laser structures. The COMD level is reached at the points of maximum optical intensity on the cleaved facet. The limit average power is therefore given by

$$P_{COMD} = \iint_{QW} I_{COMD}(x,y) dx dy = \iint_{QW} A_{COMD} (W / cm^2) \cdot I^N(x,y) dx dy \quad (1.14)$$

Where  $I_{COMD}$  is the intensity distribution, and  $A_{COMD}$  is the intensity peak at which COMD occurs,  $I^N(x,y)$  being the normalized intensity distribution of the optical mode. Considering a standard high power laser structure as our reference, we can compare the power at which COMD will occur in different configurations by simply calculating the integral of the guided

optical mode.

Table 2: Comparison of Catastrophic Optical Damage level for large optical cavity and GCSEL structure compared to standard high power GRINSEL structure.

<u>Laser structure</u>	<u>Power at facet</u>	<u>COMD improvement</u>
<ul style="list-style-type: none"> <li>0.4<math>\mu\text{m}</math> wide GRINSEL Fabry-Perot</li> </ul> 	$\int_{dy} I^N(x_0, y) dy = 1$	$P_{\text{COMD}}$
<ul style="list-style-type: none"> <li>2<math>\mu\text{m}</math> LOC Fabry-Perot</li> </ul> 	$\int_{dy} I^N(x_0, y) dy = 3.12$	$\sim 3X P_{\text{COMD}}$
<ul style="list-style-type: none"> <li>Grating-coupled laser <math>L_{\text{out}}=50\mu\text{m}</math></li> </ul> 	$\left\{ \begin{array}{l} \int_{dy} I^N(x_0, y) dy = 165 \\ I^N(y) = \exp\left(-\frac{y}{L_{\text{out}}}\right) \end{array} \right.$	$\sim 165X P_{\text{COMD}}$

### 1.2.4 Conclusion

We reviewed some basic concepts of semiconductor lasers and introduced the parameters we will use to characterize the devices investigated in this dissertation. We saw that an ideal laser should have the following characteristics:

- High power and high brightness
- High conversion efficiency
- Scalable power
- Low divergence
- Monolithically integrated beam shaping optics

However, standard Fabry-Perot configuration with cleaved facets mirrors typically suffer from:

- Highly divergent spatial beam profile
- Catastrophic Optical Damage

Grating-coupled devices appear to be a very attractive choice to obtain a low divergence high power beam that can be manipulated on the chip. We will now review selected published research on grating-coupled surface emitting lasers to justify the use of integrated grating coupler technology as well as identify the areas where our work may improve the state of the art.

## **1.3 Overview of grating-coupled lasers research**

### **1.3.1 Towards high efficiency, high power and high brightness devices**

The first grating-coupled surface emitting lasers GCSEL device was published by Alferov et al. [Alferov 1973] rapidly followed by others [Burnham 1975, Zory 1975, Reihhart 1975]. These devices used a second order Bragg reflector to provide vertical emission of the light as well as feedback inside the cavity. Following significant progress in the quality of grown material and fabrication processes in the 1980's, a great amount of research was carried out on 1D and 2D coherent arrays of grating-surface-emitters to obtain higher power and narrow linewidths [Evans 1989]. The reader will find a complete review of this work in [Evans 1993] while only selected results are represented here. In 1989, separation of feedback from outcoupling function was achieved by using a first order Bragg grating for master oscillator followed by power amplifiers using detuned second order Bragg grating for outcoupling (GSE-MOPA) [Carlson 1990, Welch 1990(a)]. External differential efficiency of 67% was obtained from a 9 element array using a superlattice reflector grown in the substrate [Mehuys 1991(a)]. Such second order detuned grating, similar to the ones used in this work, showed reflectivity as low as  $10^{-4}$  inside the cavity [Mehuys 1991(b)]. Although the substrate reflector provided the highest GCSEL external differential efficiency reported, it suffers from poor thermal properties in CW operation due to the required p-side up mounting of the device on the heat sink. It was also shown that grating

directionality may be enhanced by blazing the grating couplers but this approach requires tilting the sample inside the chamber and makes the device performance less tolerant to grating parameters variation [Hagberg 1996]. Another approach is to use a  $\lambda/4$  dielectric coating of the grating followed by metallization for light extraction through the substrate. When combined with an anti-reflection coating of the substrate, a 60-63% improvement of the device efficiency through the substrate was reported using this technique [Evans 1989]. We will follow this approach to fabricate high reflection coatings on our grating couplers. However, the beam quality of such array typically suffers from nonuniform wafer flatness that leads to phase incoherence. The beam emitted from GSE arrays is also highly asymmetric due to the multiple emitters' configuration.

As far as single emitters are concerned, surface emitting devices using low reflectivity grating couplers have recently been used successfully in external cavity configurations. Hybrid modelocking producing 22.6ps pulses was demonstrated by Kim et al. Also broad wavelength tunability of 115nm was obtained using an external mirror [Jiang 1999]. We believe the work presented in this dissertation should significantly improve the performance of such applications.

As an alternative to grating couplers, some researchers proposed to use a tilted mirror to reflect light through the substrate [Liau 1985]. This approach does not require the patterning of fine features and minimizes coupling losses and can produce narrow linewidth and low threshold by using a buried mirror in the substrate [Ou 1991]. However, it does suffer from the same COMD limitations than Fabry-Perot devices. Also, the beam still needs to be collimated, in the best case by a lens integrated on the backside, which limits the advantage of having a second surface to

integrate beam shaping elements. Finally, it is difficult to control the angle of the mirror because of GaAs crystalline structure and a slight deviation from 45 degrees ( $\pm 3$  degrees) yields an output extracted up to 20 degrees off-normal due to the high index contrast at the substrate/air interface [Stegmuller 1991].

The spatial beam quality of single emitter GCSEL devices was greatly improved by the use of unstable resonators and flared geometries [Luo 2000] where the forward and backward propagating waves are not conjugate and only one transverse mode is supported in the cavity. Such resonators were either created by integrating curved gratings with a wide contact stripe [Macomber 1996] or by shaped electrodes, either in bow-tie [Bedford 2000] or flared configuration [Eriksson 2001] to maintain a single spatial mode. In this case, the grating curvature must be adjusted to the phase function of the output wave and is negatively affected by the thermal lens function created in CW operation and moderate pumping conditions. Another approach recently proposed by Bedford [Bedford 2002] consists in using a grating aperture smaller than the stripe width of a flared amplifier in order to optimize the coupling to the single mode ridge. A 40% increase of the device differential quantum efficiency was reported using this technique compared to infinite aperture grating coupler. Please note that in our work, we will not focus on the transverse mode quality but on the device efficiency and integration of monolithic optical elements. However the technology presented in this dissertation is largely independent of the contact stripe geometry, except for the need to write curved gratings to collimate the output beam, and the spatial mode profile could be improved by choosing one of the above mentioned solutions.

### 1.3.2 Integration of beam-forming capability with a grating coupler

Although waveguide holograms were first demonstrated by Suhara in 1976 [Suhara 1976] using holographic techniques, the flexibility of electron beam lithography tools gave birth of new concepts that were not achievable with standard holography. The possibility of integrating beam-forming elements directly with a grating coupler was first proposed by Li [Li 1996]. In this innovative scheme, the phase shift is applied by the grating coupler by locally dislocating the grating into cells that are shifted by an amount that corresponds to the local phase shift applied to the output beam. A focusing grating coupler as well as a spot array generator was created using this technique [Eriksson 2001]. However the spot size produced by the array generator was found to be much larger than the spot size produced by the focusing grating. It was then shown that dislocation of the grating can lead to significant amount of feedback inside the cavity even if the grating is detuned from resonance, leading to filamentation inside the unstable resonator. The reflectivity from an array generator was shown to be around 100 times higher than a collimating coupler [Modh 2002]. One approach to solve this problem was to use a MOPA configuration with a beam-forming element to avoid the reflection into the oscillator but very low power, around 10mW for 1mm long SOA has been reported by the authors [Feng 1998]. Modh independently optimized the characteristics of the beam-shaping grating coupler for feedback and outcoupling. His group obtained a significant improvement of the beam quality from a spot array generator integrated with an unstable resonator [Modh 2002]. However the new design is responsible for decreasing the device efficiency by 40%, probably due to increased scattering



from the nonuniform grating coupler. Another issue with the dislocated grating approach is that strong sidelobes can be observed in the image plane along the direction of the contact stripe that are attributed to the exponential decay of the electric field due to the grating coupling [Feng 1998]. Finally, since a single beam shaping element is used, only amplitude or phase of the output beam can be shaped. Also, the angle of diffraction from the detuned grating coupler cannot be corrected for normal emission on the chip. It would therefore be beneficial to the device performance and functionality to decouple outcoupling from other functions aimed at controlling and shaping the output beam. Such a combination was proposed by Sheard et al. in 1996 [Sheard 1996]. Sheard proposed to integrate a diffractive doublet on a passive waveguide made of a grating coupler directing light towards a diffractive lens fabricated  $4\mu\text{m}$  above the grating. The same group also reported the combination of a grating coupler and a fan-out element on a passive waveguide [Liao 1997]. However, such a combination has never been implemented on active devices until now.

### **1.3.3 Conclusion**

The integration of diffractive optical elements into semiconductor lasers opened the way to compact, high brightness devices with increasing complex beam forming capabilities. We outlined the advantages and drawbacks of each configuration, and it should be noted that all devices with beam forming capability reported only very low efficiency and powers. In this dissertation, we propose to decouple outcoupling and beam shaping functions by integrating a

high efficiency low reflectivity grating coupler close to the waveguide and monolithic optical elements on the device substrate. The distance between the two optical elements, usually larger than 100 $\mu\text{m}$ , enables independent optimization of both elements according to an analysis of waveguide diffractive doublets reported by Liao et al. [Liao 1998].

## **1.4 High power dual optics surface emitting laser and amplifier**

### **1.4.1 Integration of optical elements on surface-emitting device substrate**

The integration of an optical element on the device substrate was first demonstrated by Liao [Liao 1990]. He and his colleagues demonstrated the fabrication of a bifocal microlens to collimate and provide feedback inside the laser cavity using a single element. A collimating lens was also integrated by Stegmüller and al. [Stegmuller 1991] with a first order grating providing the feedback necessary to lasing. In both cases, light was extracted from the device by an angled mirror etched at 45 degrees at the end of the device. The problem with this approach, compared to grating coupling, is that the output angle cannot be controlled accurately in a reproducible manner which leads to angle deviation as high as 17 degrees in the air for mirror angle deviation as small as three degrees [Stegmuller 1991]. Also, the highly diverging beam limits the functionality of the backside element since collimating is required. Finally, the emitting area is as narrow as in the edge-emitting configuration, therefore limiting the high power operation by

COMD, the level of which is decreased by the recombination centers created by surface roughness inherent to the fabrication process. At moderate power levels, vertical surface emitting lasers (VCSELs) offer a much more attractive choice.

The first monolithic integration of ion-milled Fresnel lenses on the substrate of VCSELs arrays was demonstrated by Rastani and al. [Rastani 1991]. A more complex diffractive optical element, namely a 4X4 array generator, was integrated by Martinsson and al. monolithically on a VCSEL with 29% diffraction efficiency and spot sizes less than 400 $\mu$ m and this work was pursued by Karlsson to transfer continuous relief elements in GaAs [Karlsson 2003].

VCSELs are clearly very good candidates for low power levels optical interconnects. However the in-plane geometry offers the possibility of integrating more functions such as modulators, tunability [Coldren 1995] as well as high power and therefore was chosen as the platform of choice for this work.

#### **1.4.2 Scope of the dissertation**

The scope of this dissertation is to design and fabricate high power high efficiency broad area lasers with monolithically integrated micro- and nano-optical elements. The devices are emitting at a wavelength around 980nm. The proposed configuration decouples for the first time the outcoupling and beam-shaping functions by using a low reflectivity tapered grating coupler to diffract a low divergence beam towards the substrate where it interacts with a second optical element such as a focusing lens, splitter or subwavelength anti-reflection grating.

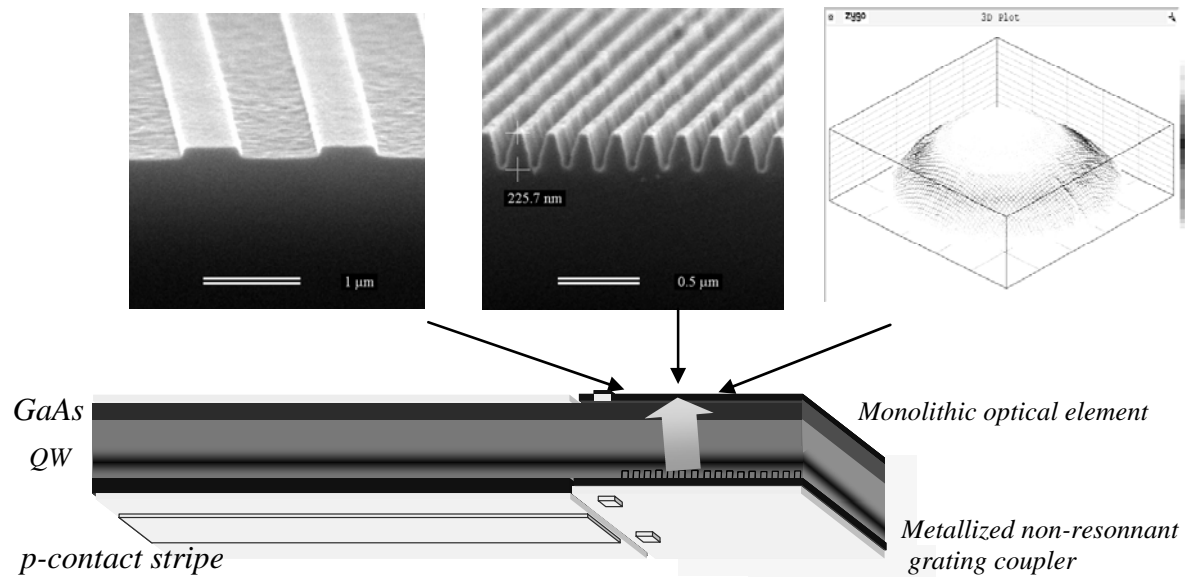


Fig.5: Surface-emitting laser diode with dual optical elements. Light is outcoupled by a low reflectivity grating coupler. The device substrate is used to improve the device performance and functionality using monolithic integration of optical elements. We demonstrate the integration of a refractive lens, a beam-splitter and a subwavelength antireflection structure.

The main points being addressed in this dissertation are

- Design and fabrication of low reflectivity, high efficiency grating coupler
- Impact of the low reflectivity grating coupler integration on the device characteristics (COMD, spectrum, near-field intensity profile).
- Experimental analysis of the losses mechanisms involved in the device performance and evaluation of the grating coupler efficiency
- Improvement of the device performance by monolithic integration of diffractive and refractive optical elements on the substrate

## **CHAPTER 2: NUMERICAL MODELING AND DESIGN**

The design and analysis of a grating-coupled surface emitting laser involves the implementation of various numerical models to analyze both passive and active elements of the device. We will first detail the waveguide AlGaAs/GaAs structure used for this work to obtain both good confinements and efficient interactions with the grating coupler. A self-consistent model of the semiconductor laser is then described to understand the nonlinear effects inside the semiconductor material that affect the spatial transverse beam profile in the direction perpendicular to the contact stripe. We will then describe the mechanisms involved with a grating coupler and determine the optimum parameters that produce an efficient grating coupler. The numerical tools used to analyze and design the grating coupler, based on a perturbation technique and finite-difference time domain model will be described.

### **2.1 Semiconductor device structure**

#### **2.1.1 Finite element method analysis of a waveguide structure**

Due to the polarized nature of the gain in slab waveguide geometry semiconductor laser, we will only consider the TE case, the electric field being perpendicular to the structure, in our analysis.

The transverse electric field (TE) may be written as

$$E(y,z) = E_0(y) \cdot \exp(j\beta z) \quad (2.1)$$

where  $\beta$  is the propagation constant and  $\omega = \frac{2\pi\lambda}{c}$  is the angular frequency. From Maxwell equations, in a stack of layer of refractive index distribution  $n(y)$ , the wave equation may be written

$$\nabla^2 E_0 + (k_0^2 n^2 - \beta^2) E_0 = 0 \quad (2.2)$$

The method of weighted residuals, where the electric field is decomposed on a set of basis functions, is used to find the electric field distribution of the guided modes in the laser transverse structure. Following the Galerkin method [Kawano 2001], we are using the sinusoidal basis set as for expansion of  $E_0$  as follows

$$E_0(y) = \sum_{i=1}^N a_i \phi_i(y), \text{ where } \phi_i(y) = \sqrt{\frac{2}{L}} \sin\left(\frac{i\pi y}{L}\right), (i, N) \in N^2 \quad (2.3)$$

where  $L$  defines the width of the domain of expansion. We replace  $E_0$  by its expansion in the wave equation then multiply by  $\phi_j, j \in [1, N]$  and integrate over the domain of expansion. This results in the following eigenvalue equation

$$\sum_{i=1}^N a_i \left( \frac{-m^2 \pi^2}{L^2} \right) \delta_{i,j} + k^2 \sum_{i=1}^N a_i \frac{2}{L} \int_0^L n^2(y) \sin\left(\frac{i\pi y}{L}\right) \sin\left(\frac{j\pi y}{L}\right) dy = \beta^2 \sum_{i=1}^N a_i \delta_{i,j} \quad (2.4)$$

where

$$\left(\frac{-L^2}{M^2\pi^2}\right)\int_0^L \sin\left(\frac{i\pi y}{L}\right)\sin\left(\frac{j\pi y}{L}\right)dy = \delta_{i,j} = \begin{cases} 1 & \text{if } i = j \\ 0 & \text{if } i \neq j \end{cases} \quad (2.5)$$

$\delta_{i,j}$  represents the Kronecker discrete delta function. Equation (2.5) can then be rewritten as

$$[M].[a] = \beta^2[a] \quad (2.6)$$

where  $M$  is a N by N matrix. One can therefore find the eigenvalue(s) of the matrix and the corresponding eigenvector(s) is(are) then used to represent the electric field. The propagating modes are defined by the cut-off condition

$$k_0 n_s < \beta < k_0 n_c \quad (2.7)$$

where  $n_s$  is the refractive index of the core region. We restrict our analysis to the real plane, neglecting the potential imaginary part of the propagation constant that would result from searching eigenvalues in the complex plane. We will now see how the fundamental mode calculated by the Galerkin method is used to evaluate the grating strength using a perturbation technique.

### 2.1.2 AlGaAs/GaAs Grinsch structure

We are considering an AlGaAs/GaAs structure with a 8nm thick InGaAs quantum well for emission around 980nm. The structure was grown by Coherent Inc.. The refractive index of each layer is shown below in 3. This structure was analysed using the Galerkin method described

above.

Table 3: AlGaAs/GaAs GRINSCH structure grown by Coherent Inc. The substrate is thinned down to a thickness 150 $\mu\text{m}$ .

Layer #	Material	Layer Description	Thickness ( $\mu\text{m}$ )
0	n-GaAs Substrate		
1	GaAs	buffer layer	0.200
2	$\text{Al}_y\text{Ga}_{1-y}\text{As}$	n-cladding	1.200
3	$\text{Al}_y\text{Ga}_{1-y}\text{As} \rightarrow \text{Al}_x\text{Ga}_{1-x}\text{As}$ graded	waveguide	<b>0.200</b>
4	GaAs	buffer layer	0.010
5	<b><math>\text{In}_{1-x}\text{Ga}_x\text{As}</math></b>	<b>QW</b>	<b>0.008</b>
6	GaAs	buffer layer	0.010
7	$\text{Al}_x\text{Ga}_{1-x}\text{As} \rightarrow \text{Al}_y\text{Ga}_{1-y}\text{As}$ graded	waveguide	<b>0.200</b>
8	$\text{Al}_y\text{Ga}_{1-y}\text{As}$	p-cladding	<b>0.250</b>
9	<b>InGaP</b>	<b>etch -stop</b>	<b>0.020</b>
10	$\text{Al}_y\text{Ga}_{1-y}\text{As}$	p-cladding	0.750
11	GaAs	p-contact	0.200

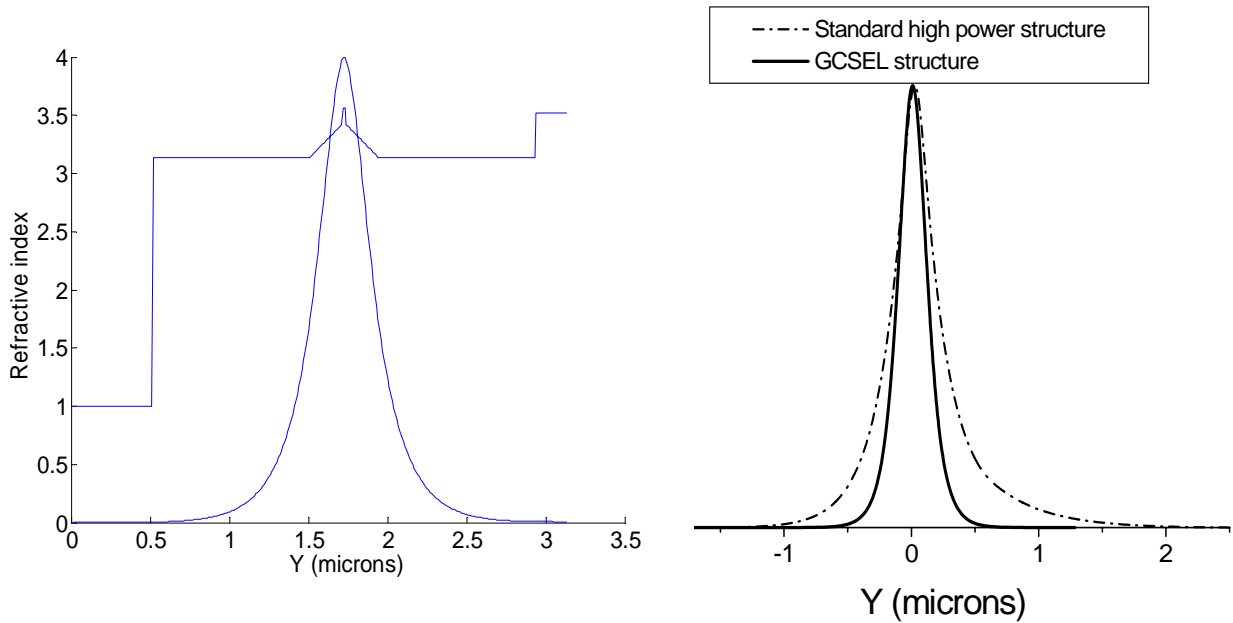


Fig.6: Electric field amplitude distribution of the fundamental mode in the designed structure (left). The intensity distribution is compared to the intensity profile propagating in a standard high power laser diode structure (right).



The quantum confinement factor is found to be 2.71% and the effective index of the fundamental mode was calculated to be 3.31. About 6.5% of the electric field amplitude distribution is confined in the p-cladding, which was found to be enough to obtain a 50 micron outcoupling length with a 250nm deep grating.

The intensity profile of the fundamental mode propagating in the structure is shown in Fig.6 and is compared to a standard high power AlGaAs/GaAs structure grown by another leading diode manufacturer. One can see that the field guided in a standard high power structure extends significantly in the p-doped and n-doped claddings. The main benefit of such structures is to increase the COMD level by decreasing the optical intensity at the cleaved facet. However, in grating-coupled surface-emitting lasers, the optical mode is transformed by the grating coupler and therefore optical intensity is distributed over a wider area which in turn virtually eliminates material damage as it was explained in Chapter 1.

### **2.1.3 Fabry-Perot device performance**

The fundamental performance parameters of Fabry-Perot devices were measured experimentally to determine a reference when evaluating the performance of the grating-coupled devices. The external differential quantum efficiency was measured for uncoated devices of different lengths. The results were used to calculate the internal efficiency and internal losses of the device using a linear fit to equation (1.11). The devices showed an average internal efficiency  $\eta_i$  of 95.6% and

internal losses  $\alpha_i$  of  $2.5 \text{ cm}^{-1}$ . Also, devices show an average series resistance of  $2.5 \times 10^{-4} \Omega \cdot \text{cm}^2$ , measured from the derivative of the voltage versus current (I-V) curve. These parameters are used to investigate the device performance using a self-consistent model of the semiconductor laser as explained in the next section.

#### **2.1.4 Self-consistent modeling of the broad stripe laser and amplifier**

The near-field intensity profile along the direction perpendicular to the grating grooves can be accurately predicted using this technique. However, in the transverse direction, the near-field intensity profile is governed by the laser cavity and modeling a complete two dimensional intensity profile therefore requires an understanding of the laser behavior. Several authors have proposed a self-consistent model based on beam-propagation method [Agrawal 1984] in order to simulate gain-guided axially nonuniform geometries. In his work, Agrawal solves the coupled equations of propagation and carrier density distribution at every step of the propagation after eliminating the y dimension using the effective index method. Following his approach, several authors proposed to include thermal effects to investigate distortions of the transverse beam profile and filamentation [Hadley 1988, Lang 1993, Dai 1997]. The same approach was used to simulate unstable resonators and GCSELS [Eriksson 1997]. Implementing such a model for GCSELS devices is useful to obtain information on transverse field profile, efficiency of the device, and phase changes that may be corrected by appropriate grating design. The beam-propagation scheme was implemented using Finite-Difference Method (FD-BPM) instead of the

usual fast-fourier transform technique proposed by Agrawal. The nonlinear material gain is represented by a third order polynomial to be linearized in the solution of the carrier density equation. The carrier density equation is solved at every propagation step using Causa's Hermite-Gauss method [Causa 1999] which provides a fast and accurate way of solving the equation for carrier density profiles such as top-hat or gaussian. The thermal effects are quantified using a method proposed by Lang [Lang 1993] where the thermal impulse response of the laser structure is calculated using finite element method and then convolved by the heat terms at every propagation step.

#### 2.1.4.1 Wave propagation

The electric field in the resonator is described by two waves  $\vec{E}_f$  and  $\vec{E}_b$  representing light traveling in the forward (positive  $z$ ) and backward (negative  $z$ ) direction respectively. The field may be written

$$\begin{cases} \vec{E}_f = E_f(x,z)\exp(i(\omega t - \beta z)).\vec{u} \\ \vec{E}_b = E_b(x,z)\exp(i(\omega t + \beta z)).\vec{u} \end{cases} \quad (2.8)$$

After substitution in the wave equation and neglecting  $\frac{\partial^2 E_{f,b}}{\partial z^2}$  we obtain the paraxial wave equation

$$\varepsilon_{f,b} 2ik_0 \frac{\partial E_{f,b}}{\partial z} + \frac{\partial^2 E_{f,b}}{\partial x^2} + k_0^2 (n^2(x,z) - n_{eff}^2) E_{f,b} = 0, \text{ with } \begin{cases} \varepsilon_f = +1 \\ \varepsilon_b = -1 \end{cases} \quad (2.9)$$

The effective index is obtained by the Galerkin method described in the previous section. Here we normalized the electric field so that the power at the output of the laser diode is given by

$$P_{f,b} = T_{f,b} \cdot \int_{-\infty}^{\infty} |E_{f,b}(x, z_{out})|^2 dx \quad (2.10)$$

where  $T_{f,b}$  is the transmission coefficient of the cleaved facet or the grating and  $z_{out}$  equals 0 for  $E_b$  and the cavity length for  $E_f$ . Therefore the quantity  $|E_{f,b}(x, z_{out})|^2$  is in [W/cm]. In order to include the thermal and carrier induced effects on the refractive index distribution, the index distribution  $n(x,z)$  is written as [Eriksson 1998]

$$n(x,z) = n_{eff} + \frac{1}{2k_0} [\Gamma g(x,z) \cdot (i+b) - i\alpha_i] + \alpha_T \Delta T(x,z) \quad (2.11)$$

Assuming small changes of the index of refraction one gets

$$n_{eff}^2 - n^2(x,z) \approx \frac{n_{eff}}{k_0} \cdot \llbracket [\Gamma g(x,z) - \alpha_i] - i[\Gamma g(x,z) \cdot b + k_0 \alpha_T \Delta T(x,z)] \rrbracket \quad (2.12)$$

In this equation, the term  $\Gamma g(x,z)$  represents the modal gain, the other parameters are defined in Table 4. The antiguiding factor  $b$  is mainly responsible for the nonlinear effects creating filamentation and beam profile distortion observed in pulsed conditions while thermal effects are typically responsible for CW operation beam degradation.

Table 4: Structure parameters calculated or taken from literature for standard InGaAs structure. These parameters can then be plugged in the modeling tool described in paragraph 2.1.4.

Parameter	Value	Unit
Wavelength in air $\lambda_0$	$972.10^{-9}$	M
Non radiative recombination rate $\tau_{NR} (1/A)^*$	$5.10^{-9}$	S
Bimolecular recombination rate $B^*$	$1.2.10^{-10}$	$\text{cm}^3/\text{s}$
Auger recombination rate $C^*$	$3.5.10^{-30}$	$\text{cm}^3/\text{s}$
Diffusion coefficient $D^*$	30	$\text{cm}^2/\text{s}$
Antiguinding parameter $b^*$	2.5	
Active layer thickness	$8.10^{-9}$	M
Internal Quantum efficiency $\eta_i$	0.956	
Effective index $n_{\text{eff}}$	3.31	
Confinement factor $\Gamma$	0.0271	
Thermal index coefficient* $\alpha_T$	$3.10^{-4}$	$\text{K}^{-1}$
Intrinsic losses $\alpha_i$	2.5	$\text{cm}^{-1}$
Voltage offset $V_d$	0.16	V
Series resistance $\rho$	$2.5 \times 10^{-4}$	$\Omega.\text{cm}^2$
Current density J	Varies	$\text{A}/\text{cm}^2$

$\Gamma$  is the confinement factor defined as the fraction of power confined to the active quantum well layer (QW)

$$\Gamma = \frac{\int_{QW} |E_y|^2 dy}{\int_{-\infty}^{\infty} |E_y|^2 dy} \quad (2.13)$$

The main device parameters are included in the table below. The parameters shown with an asterisk are standard numbers were taken from the literature [Eriksson 2001] and are used to model the carrier and optical density coupling inside the material.

#### 2.1.4.2 Numerical implementation by FD-BPM

The numerical implementation of the propagation equation was done using the finite-difference beam propagation (FD-BPM) method [Kawano 2001]. The derivatives of the slowly varying envelope  $E_{fb}$  is calculated numerically following the Crank-Nicholson scheme

$$\begin{cases} \frac{\partial^2 \phi}{\partial x^2} = \frac{1}{\Delta x} \left( \frac{\phi_{p+1} - \phi_p}{\Delta x} - \frac{\phi_p - \phi_{p-1}}{\Delta x} \right) = \frac{\phi_{p+1} - 2\phi_p + \phi_{p-1}}{(\Delta x)^2} \\ \frac{\partial \phi}{\partial z} = \frac{\phi_p^{l+1} - \phi_p^l}{\Delta z} \end{cases} \quad (2.14)$$

where we discretized  $x$  and  $z$  as  $\begin{cases} x = p\Delta x, p \in Z \\ z = l\Delta z, l \in Z \end{cases}$ .

By replacing the terms in (2.14) by their discrete expressions we obtain the following matrix

equation

$$[M][\phi_i^{l+1}] = [C_i^l] \quad (2.15)$$

where M is a tridiagonal matrix and  $C_i^l$  is a vector function of  $\{\Phi_{p-1}^l, \phi_p^l, \phi_{p+1}^l\}$ . Because the field is relatively well confined inside the gain-guided region of analysis, we implemented a transparent boundary conditions scheme to the edge of the analysis area (x axis) [Hadley 1992]. At the boundaries the electric fields are reflected and their expressions are given by

$$\begin{cases} E_b(x, z \text{ max}) = \sqrt{R_f} (E_f^*(x, z \text{ max})) \\ E_f(x, 0) = \sqrt{R_b} (E_b^*(x, 0)) \end{cases} \quad (2.16)$$

where  $E^*$  denotes the complex conjugate of  $E$ .

#### 2.1.4.3 Solution of the carrier density equation

The one dimensional time-independent carrier density distribution is governed by

$$D \frac{\partial^2 N(x)}{\partial x^2} = -\eta_i \frac{J(x)}{qd} + AN(x) + BN^2(x) + CN^3(x) + \Gamma g(N(x)) \frac{|E_f|^2 + |E_b|^2}{d\hbar\omega} \quad (2.17)$$

where the gain is expressed as

$$g(N) = g_0 + g_1 N + g_2 N^2 \quad (2.18)$$

The nonlinear differential equation can be rewritten at each step of the propagation as

$$D \frac{\partial^2 N}{\partial x^2} - \frac{N}{\tau(N)} + C(x) = 0 \quad (2.19)$$

With

$$\begin{cases} \tau(N) = 1 / \left( \frac{1}{\tau_{NR}} + \Gamma g_1 \frac{|E_f|^2 + |E_b|^2}{d\hbar\omega} + \left[ B + \Gamma g_2 \frac{|E_f|^2 + |E_b|^2}{d\hbar\omega} \right] \cdot N + \left[ C + \Gamma g_3 \frac{|E_f|^2 + |E_b|^2}{d\hbar\omega} \right] \cdot N^2 \right) \\ C(x) = \frac{J(x)}{qd} - \Gamma g_0 \frac{|E_f|^2 + |E_b|^2}{d\hbar\omega} \end{cases} \quad (2.20)$$

This equation shows how the optical field influences the carrier density distribution by the stimulated emission process where carrier depletion is triggered by propagating photons. Reciprocally, the carrier density affects the optical field distribution through the material gain  $g$ . To solve this equation we follow Causa's Hermite-Gauss method [Causa 1999]. The carrier density is expressed as a finite sum of Hermite-Gauss polynomials as

$$N = \sum_{k=0}^M a_k f_k(x), M \in \mathbf{Z} \quad (2.21)$$

where

$$f_k(x) = C_k H_k\left(\frac{x}{w_0}\right) \exp\left(-\frac{x^2}{2w_0^2}\right) = \sqrt{\frac{1}{w_0 2^k k! \sqrt{\pi}}} H_k\left(\frac{x}{w_0}\right) \exp\left(-\frac{x^2}{2w_0^2}\right) \quad (2.22)$$

is the normalized Hermite-Gauss polynomial of order  $k$  of width  $w_0$ . This basis set is



particularly suitable to represent the variety of supergaussian carrier density distributions profiles, especially in tapered structures. To avoid numerical errors due to the representation of rectangular profile by a finite expansion we chose to represent the current density by a supergaussian function to obtain a flat-top profile with rounded edges. The equation (2.19) is then solved iteratively. First  $\tau(N)$  is assumed constant, and the collocation method is used instead of the classic orthogonalization procedure to find the weighting coefficients  $\mathbf{a}_k$  [Causa 1999]. In the collocation method, equation (2.19) is written at  $M$  particular points  $x_i$ , where  $x_i$  are the zeros of the  $M$ th order Hermite Gauss polynomial. This is written

$$D \frac{\partial^2 N}{\partial x^2} \Big|_{x_i} - \frac{N(x_i)}{\tau(N_c)} + C(x_i) = 0 \quad (2.23)$$

where  $N_c$  is assumed to be a known function of the carrier density. We obtain then a  $M$  by  $M$  matrix defined by

$$M_{HG}(i,j) = f_{j-1}(x_i) \cdot \left( \frac{D}{w_0^2} \cdot (-x_i^2 + 1 + 2 \cdot (j-1)) + \frac{1}{\tau(N_c(x_i))} \right), (i,j) \in [1,M]^2 \quad (2.24)$$

The  $\mathbf{a}_k$  coefficients are calculated as eigenvectors of the matrix eigenvalue equation. The expression for the carrier density calculated from (2.21) is used to update  $N_c$  until a stable carrier density distribution is obtained. The stability condition used is

$$\int_{-\infty}^{\infty} \left| \frac{\sqrt{\left| |N_c^{i+1}|^2 - |N_c^i|^2 \right|}}{\max(N_c^i)} \right| dx \leq \varepsilon_{err}, \varepsilon_{err} \in \mathfrak{R}^{+*} \quad (2.25)$$

We found that  $M=40$  is usually enough to obtain stable and relatively accurate distribution after only three or four iterations as shown in Fig.7. Also, using the fact that the carrier density profile is slowly varying along the longitudinal direction, the time required to complete a propagation round-trip may be enhanced significantly by considering the carrier density obtained at the step  $z$  as the guess profile for step  $z+\Delta z$ . In that case the profile is generally correctly updated after a single iteration with accuracy greater than  $1.10^{-4}$ .

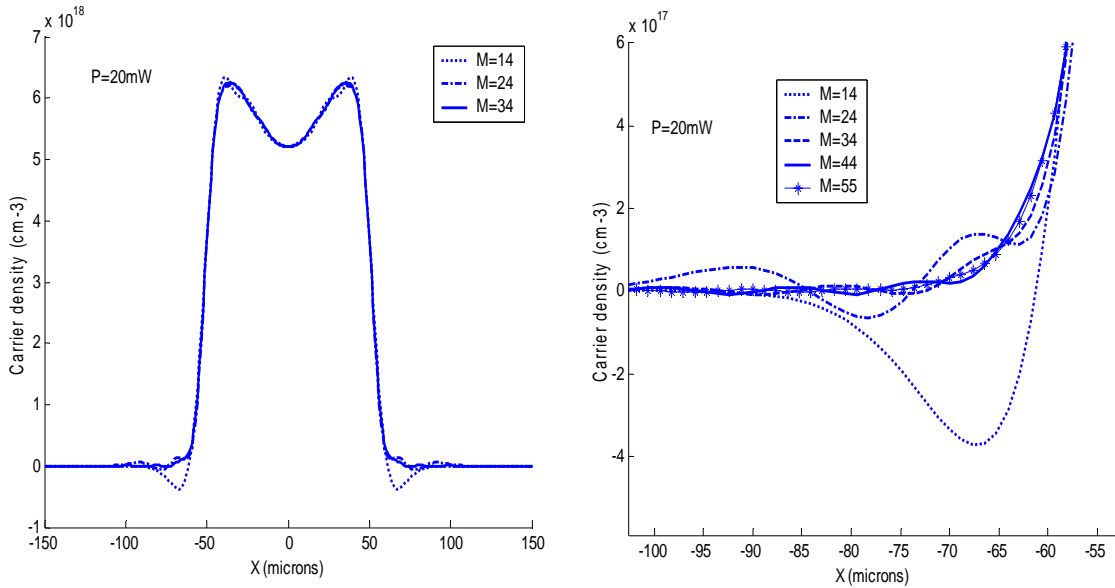


Fig.7: Influence of the number of terms on a typical profile affected by the optical mode intensity distribution.  $\varepsilon=10^{-5}$ . The optical power is 20mW. The current density is  $1\text{kA}/\text{cm}^2$ .

The number of Hermite-Gauss polynomials is critical to the accuracy of the complex profiles obtained when the optical field profile influences the carrier density distribution as shown in Fig.7 since the high frequencies of the profile require a higher number of terms to be accurately represented. This is the case for high power devices.

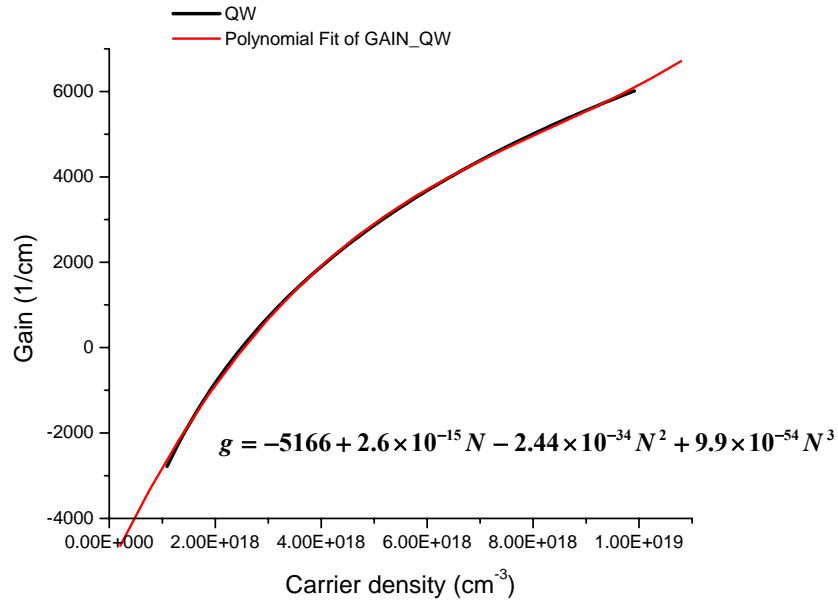


Fig.8: Polynomial fit of logarithmic expression for gain of quantum well obtained from [Eriksson 1998].

Although initial work used a linear approximation of the gain as a function of the carrier density [Agrawal 1984], experimental data shows that the modal gain is actually closer to a logarithmic function of the carrier density [Bossert 1996]. In order to combine the actual variation of the gain with the Hermite-Gauss method, we fitted a third order polynomial to the expression of the logarithm gain expression found in [Eriksson 1998]. The nonlinear correction shown in Fig.8 is not very important around threshold but is critical when investigating the behavior of the

amplifier or laser at high pumping current and carrier densities.

#### 2.1.4.4 Thermal effects

We neglected the thermal effects in this work although the phase induced by the temperature elevation can create important change in the far-field divergence of the device. We briefly mention how Lang proposed a simple method to integrate temperature effects into the model for completeness. For high-power devices, heating becomes a major problem in CW operation that is usually responsible for a saturation of the output power. The heating effect is generated by two physical phenomena. The first one is related to the injected electrons in the structure and depends of the device resistance. The second is due to the absorption of photons due to the intrinsic losses. On the other hand stimulated emission is carrying away some of the electrical energy, therefore decreasing the magnitude of the first term responsible for heating. This process is also known as “photon cooling”. The local heat load can then be written as [Lang 1993]

$$Q(\text{W} / \text{cm}^2) = V \cdot J(x, z) + (\alpha_i - \Gamma g(N)) \left( |E_f|^2 + |E_b|^2 \right) \quad (2.26)$$

with

$$V = \frac{\hbar \omega}{q} + V_d + \rho J \quad (2.27).$$

$\rho$  and  $V_d$  are respectively the series resistance and voltage offset obtained from current versus

voltage characteristics. The effect of this heat load on the laser will depend of the thermal properties of the layers used to make the laser. In order to characterize this effect, Lang proposed to determine the thermal impulse response of the device by calculating the temperature elevation of a cross section x-y of the device resulting from a spatial delta function of unit power distribution. The restriction of the impulse response flux  $f(x, y)$  (K.cm<sup>2</sup>/W) to the active layer  $f(x)$  may then be convolved by the heat load  $Q(x, z)$  to determine the temperature elevation inside the active region at each propagation step without having to simulate the structure again.

$$\Delta T(x, z) = f(x) * Q(x, z) \quad (2.28)$$

The temperature elevation is then plugged into

$$n_{eff}^2 - n^2(x, z) \approx \frac{n_{eff}}{k_0} [\Gamma g(x, z) - \alpha_i - i(\Gamma g(x, z)b + k_0 \alpha_T \Delta T(x, z))] \quad (2.29)$$

## **2.2 Numerical modeling of an integrated grating coupler**

### **2.2.1 Grating coupler basic mechanism**

The grating coupler is an important component of integrated optics. It is generally used to couple light into or out of a waveguide. Unlike tilted Bragg gratings written in photosensitive optical fibers [erdogan 1996], most grating couplers used in integrated optics are surface relief grating

that scatter the electric field guided in the waveguide using a periodically corrugated surface. The period is chosen such that light is coupled into radiation modes diffracted towards the substrate and in the air. This is opposed to distributed feedback (DFB) or distributed Bragg reflector (DBR) lasers where the first diffracted order is coupled back into the cavity for narrow spectral filtering according to the classical equation:

$$m\lambda = 2n_{eff}\Lambda, m \in \mathbb{N}^* \quad (2.30)$$

where  $\lambda$  is the wavelength in air,  $n_{eff}$  is the effective index of the propagating medium and  $\Lambda$  is the grating period (Fig.9). In the general case, the grating lines are not exactly perpendicular to the direction of propagation in the waveguiding structure, either voluntarily to decrease reflectivity or by fabrication error.

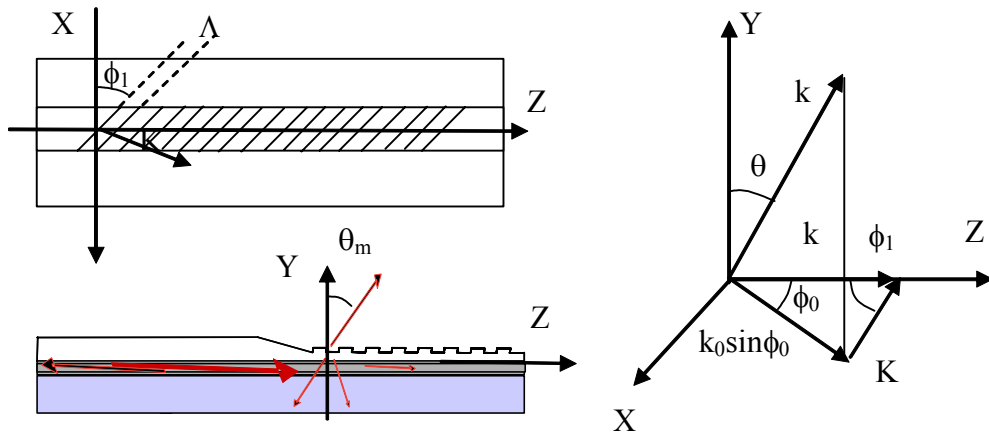


Fig.9: GCSEL general configuration and equivalent wave-vector diagram.

By the phase-matching condition the angle of the diffracted order  $m$  is given by [Evans 1993]

$$\sin \theta_m = \frac{\sqrt{n_{eff}^2 - \frac{(2n_{eff}m\lambda \cos \phi_1)}{\Lambda} + \frac{m^2 \lambda^2}{\Lambda^2}}}{n_0} \quad (2.31)$$

where  $n_0$  is the index of the substrate or superstrate material. This equation can also be used to determine the acceptance angle of the radiation outcoupled by the grating coupler since  $\phi_1$  can also represent the angle of the rays inside the cavity. In the simple and practical case where one keeps the diffracted beam in the plane perpendicular to the stripe, the diffracted orders angle equation then reduces to

$$\sin \theta_m = \frac{n_{eff} - m \frac{\lambda}{\Lambda}}{n_0} \quad (2.32)$$

This equation can be used to find the proper conditions where only one order is diffracted in the superstrate (generally air) and one order is diffracted in the substrate.

### 2.2.2 Perturbation technique analysis

The interaction between the diffraction grating and the guided electric field can be evaluated in first approximation using a perturbation technique following [Tamir 1977] and [Streiffer 1976]. We detail here the application of this technique to a GRINSCH multilayer structure. The refractive index of a multilayer structure can be written

$$\begin{cases} n^2(x, z) = n_{g,0}^2(x) + \sum_{\substack{q=-\infty \\ q \neq 0}}^{\infty} A_q(x) \exp(i \frac{2\pi q z}{\Lambda}) \\ n_{g,0}^2(x) = \begin{cases} A_0 & \text{if } 0 < y < t_g \\ n_i^2 & \text{for } x_{i-1} < y < x_{i+1} \text{ otherwise} \end{cases} \end{cases} \quad (2.33)$$

where  $A_q$  represent the Fourier coefficients of the periodic index profile expansion.

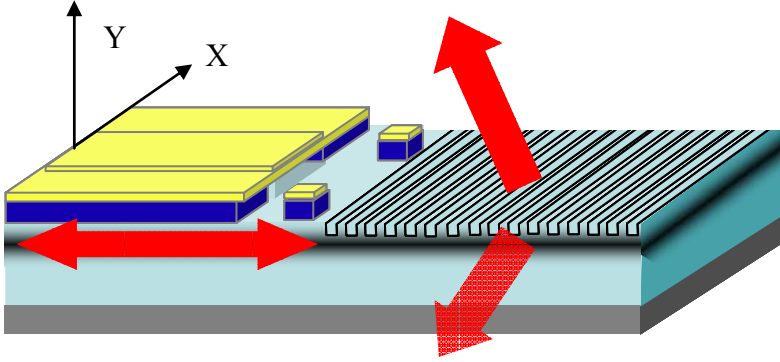


Fig.10: Radiation losses introduced by a uniform grating coupler.

The electric field can be written as an infinite sum of partial waves

$$E_0(x, z) = \sum_{m=-\infty}^{\infty} E_m(x) \exp(i\beta_m z) \quad (2.34)$$

By replacing this expression in equation (2.2) one obtains

$$\frac{d^2 E_m}{dy^2} + (k_0^2 n_{g,0}^2(x) - \beta_m^2) E_m = -k_0^2 \sum_{\substack{q=-\infty \\ q \neq 0}}^{\infty} A_{m-q}(x) E_q(x), m \in Z \quad (2.35).$$

In the perturbation technique analysis, (2.35) is first solved for the fundamental mode



propagating in the structure ( $m=0$ ) by using the Galerkin method as described in the previous section. The grating layer is approximated by a uniform layer of refractive index  $\sqrt{A_0}$  for this purpose and the power of the propagating mode is normalized to unity. The electric field distribution  $E_0$  and propagation constant  $\beta_0$  are then used in (2.35) to derive the fields for the other partial waves corresponding to the diffracted orders. In the grating layer of the diode structure, the transverse electric field is approximated by counter-propagating plane waves and a perturbation term is added following the equation

$$\frac{d^2 E_m}{dy^2} + (k_0^2 n_{g,0}^2(y) - \beta_m^2) E_m = A_m(x) E_0(x) \quad (2.36)$$

The result is a first-order approximation since the coupling between the diffracted orders is neglected. It is important to note that only the fundamental mode multiplied by the Fourier coefficient of the grating profile is used to derive the electric field of the various diffracted orders. This method is expected to provide relatively accurate estimation of the grating behavior in the case where only one diffraction order is allowed. However, its accuracy is limited by the derivation of the fundamental mode considering the grating as a uniform medium since, when light hits the grating, it has not yet been transformed to that mode. The radiation losses to diffracted orders are quantified through the time-averaged power  $P_m$  expressed as

$$P_m = \frac{1}{2\omega\mu_0} \operatorname{Re} \left( \sqrt{k_0^2 n_g^2 - \beta_m^2} |E_m(t_g)|^2 \right) T_{g,u}^m + \frac{1}{2\omega\mu_0} \operatorname{Re} \left( \sqrt{k_0^2 n_g^2 - \beta_m^2} |E_m(0)|^2 \right) T_{g,l}^m \quad (2.37)$$

where  $T_{g,u}^m$  and  $T_{g,l}^m$  represent the transmission coefficients of the power of diffracted order  $m$

through the layers above the grating-superstrate boundary and below the grating-residual layer respectively. The coefficients  $T_{g,u}^m$  and  $T_{g,l}^m$  for a multilayer structure are derived by “peeling off” the layers to find the equivalent impedance of the layers below or above the grating respectively. The field reflection coefficient between layer  $i$  and layer  $i+1$  for TE diffracted order  $m$  may be expressed as

$$r_{i \rightarrow i+1}^m = \frac{Y_{i+1}^m - Y_i^m}{Y_{i+1}^m + Y_i^m}, \text{ where } Y_i^m = \frac{k_x^{i,m}}{\omega \mu_0} \quad (2.38)$$

Then the equivalent impedance of the layer  $i$  and  $i+1$  can be expressed as

$$\frac{1}{Y_{eq,i+1}^m} = \frac{1}{Y_{i+1}^m} \frac{1 + r_{i \rightarrow i+1}^m \exp(i 2k_z^{i+1,m} t_{i+1})}{1 - r_{i \rightarrow i+1}^m \exp(i 2k_z^{i+1,m} t_{i+1})} \quad (2.39)$$

where  $t_{i+1}$  is the thickness of the layer  $i+1$ . Then by replacing  $Y_i^m$  by  $Y_{eq,i+1}^m$ , the reflection coefficient between layer  $i$  and layer  $i+2$  is given by

$$r_{i \rightarrow i+2}^m = \frac{Y_{i+2}^m - Y_i^m}{Y_{i+2}^m + Y_i^m} \quad (2.40).$$

This scheme is implemented iteratively to derive the reflection coefficient for any number of layers used to represent the laser diode structure. The losses due to power transferred to diffracted orders are quantified by a parameter  $\alpha$  ( $\text{cm}^{-1}$ ) representing the exponential decay of the propagating electric field during its interaction with the grating coupler. The guided energy coupled to radiated modes is equivalent to an absorption coefficient in the guiding medium so

that the wavevector of the guided mode can be rewritten

$$k_z = \beta_0 + i\alpha \quad (2.41)$$

Consequently all the partial waves diffracted by the grating decay at the same rate since their wavevector is given by

$$k_z^m = k_z + \frac{2\pi m}{\Lambda} = \beta_0 + i\alpha + \frac{2\pi m}{\Lambda} \quad (2.42)$$

The power of the propagating mode along the direction  $z$  perpendicular to the grating grooves may then be written

$$P(z) = P_0 \exp(-2\alpha z) \quad (2.43)$$

where  $P_0$  represents the power of the field before propagating in the grating area. By deriving equation (2.22) one gets

$$\frac{dP}{dz} = -2\alpha P = - \sum_{m=-\infty}^{+\infty} P_m \quad (2.44)$$

The total radiation losses introduced by the grating coupler through the leakage rate  $\alpha$  can be estimated as a sum of the radiated powers of the multiple diffracted orders normalized to the input power  $P_0$ .

$$\alpha(1/\mu m) = \frac{\sum_{\substack{m=-\infty \\ m \neq 0}}^{\infty} P_m}{2 \left( \frac{\beta_0}{2\omega\mu_0} \right) \int_{-\infty}^{+\infty} [E_0(x)]^2 dx} \quad (2.45)$$

Please note that the parameter  $\alpha$  is sometimes defined in the literature as the power leakage rate and therefore is twice the value obtained by equation (2.24). The grating strength may also be represented by the outcoupling length  $L(\mu m)$ , expressed as the length of interaction such that the power of the propagating mode has decayed to  $\frac{1}{e}$  and therefore

$$L(\mu m) = \frac{1}{2\alpha} \quad (2.46)$$

The modeling of a 275nm period rectangular grating integrated on the structure shown in Table 3 provides an estimation of the outcoupling length as a function of grating duty cycle and depth as shown in Fig.11. It is interesting to note that the shortest outcoupling length is obtained for duty cycles around 40% for deeper gratings. Indeed, for high duty cycles, the effective index of the grating coupler is lower which results in decreasing the energy propagating in the p-cladding by creating a strongly asymmetric cladding around the guided mode. This physical effect is actually exaggerated by the perturbation technique since the guided mode is calculated by approximating the grating coupler by a uniform medium to derive the decay coefficient. In reality, the guided mode interacting with the grating coupler is coming from the unpumped region where the full p-cladding is present. Thus the asymmetric cladding effect is expected to be less pronounced for

real devices as shown in simulations performed by finite-difference time-domain technique where the transition from the active to passive region is modeled.

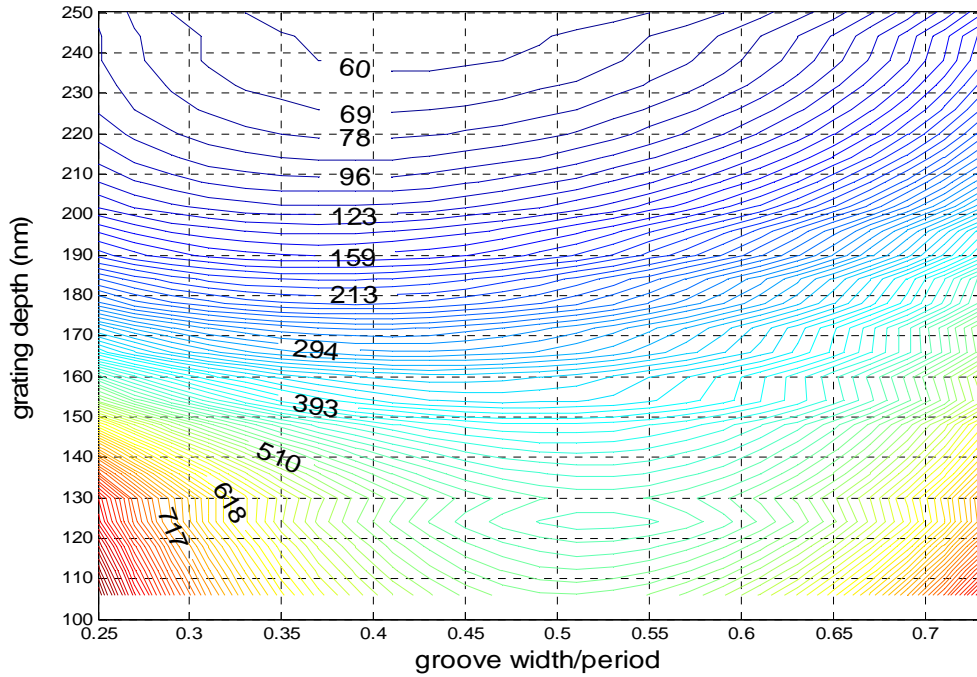


Fig.11: Plot of outcoupling length ( $\mu\text{m}$ ) versus grating depth and duty cycle for a rectangular grating coupler predicted by the perturbation technique model.

Nevertheless, good agreement is found between calculations made with FDTD and perturbation technique for 50% duty cycle as show in Fig.12. The analyzed grating length was limited to 50 microns for the FDTD model which may explain the higher disparities seen for longer outcoupling lengths.

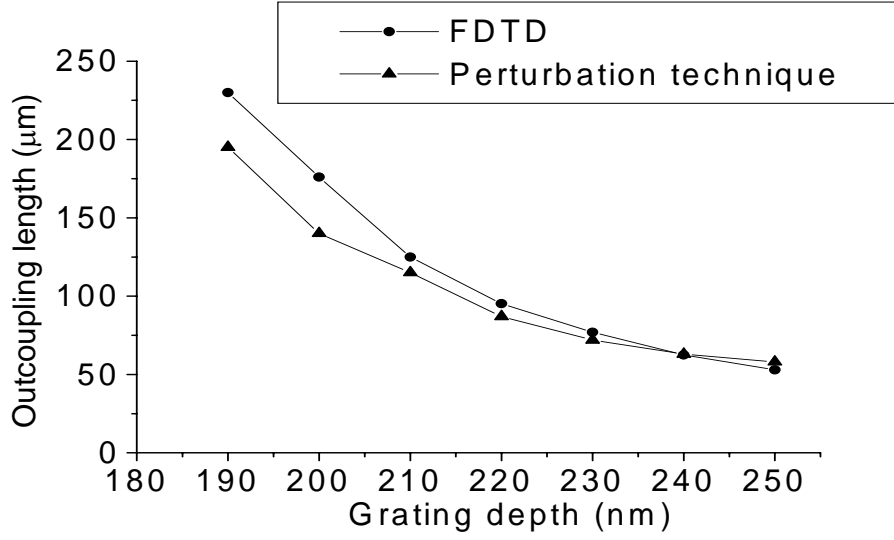


Fig.12: Outcoupling length for a 50% duty cycle grating coupler obtained by finite-difference time domain and perturbation technique.

For a given order  $m$ , the directionality of the coupler in the substrate may be estimated by

$$\eta_m^l = \frac{\text{Re}\left(\sqrt{k_0^2 n_a^2 - \beta_m^2} |E_m(t_g)|^2\right) \cdot T_{g,u}^m}{\text{Re}\left(\sqrt{k_0^2 n_a^2 - \beta_m^2} |E_m(t_g)|^2\right) \cdot T_{g,u}^m + \text{Re}\left(\sqrt{k_0^2 n_s^2 - \beta_m^2} |E_m(0)|^2\right) \cdot T_{g,l}^m} \quad (2.47)$$

or by the ratio of power diffracted in the air (substrate) divided by the power diffracted in the substrate (air). The directionality typically oscillates around 0.5 as a function of grating depth following an interference phenomenon created by the effective refractive index change of the grating coupler as a function of the grating parameters. This formula does not take reflection or substrate losses into account. Also it is assumed that the interaction length is long enough so all the power is coupled out of the waveguide. A nonsymmetric profile such as a blazed grating will enhance the directionality of the grating by diffracting more light into the air or into the substrate

[Hagberg 1996].

### 2.2.3 Finite-difference time domain modeling

The perturbation technique is a useful tool to estimate the influence of the grating and the structure parameters on coupling. However, its accuracy is limited in cases where the grating is not uniform spatially or in the case where a metal coating is used to enhance the grating directionality. Consequently, we developed a modeling tool based on finite-difference time domain to obtain a full-vectorial solution of the grating coupling problem. This approach is also suitable to examine complex geometries as well as structures including lossy dielectric or metallic materials.

#### 2.2.3.1 Numerical Implementation

The detail of the derivation of the electric field and magnetic field can be found in appendix A. From these equations we understand that it is important to have E and H interleaved in a so-called Yee cell [Yee 1966] since the values of the electric field and magnetic field are linked through derivatives in the Maxwell equations. For example, since we are using  $\frac{\partial H_z}{\partial x}$  and  $\frac{\partial H_x}{\partial z}$  to calculate  $E_y$ , these terms will be accurately represented at the point  $E_y(\mathbf{i}, \mathbf{j})$  if the derivatives

of the magnetic field are derived using the values of  $H_x(i, j \pm 0.5)$  and  $H_x(i \pm 0.5, j)$ . This scheme is represented in Fig.13. The numerical grid used for this work is typically 10nm to model the grating period with 27 points.

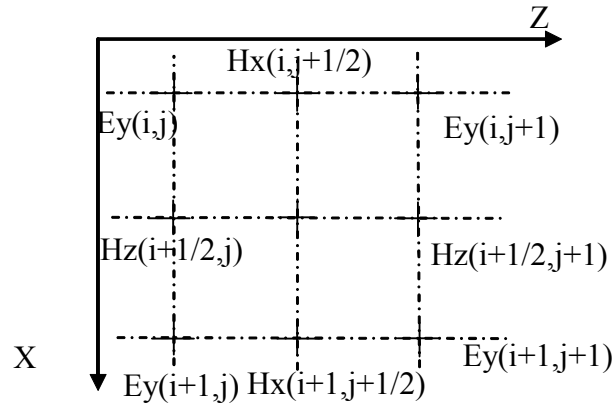


Fig.13: The Yee cell showing how Hx and Hz are interleaved with Ey to yield accurate numerical derivatives of the magnetic field involved in the calculation of the electric field.

- Benchmark with analytical solution of lossy dielectric interface

We derived the equations for lossy dielectric medium in order to introduce the conductivity parameter in the possible material to analyze. In order to benchmark the program, we simulated a CW Gaussian amplitude planar phase-front impinging on a medium with finite conductivity and compared the results obtained from the FDTD program written with the theoretical decay of the electric field given for a medium of permittivity  $\epsilon_{\text{complex}} = \epsilon_r + i * \sigma$  by the following equation:



$$\alpha = \frac{2\pi}{\lambda} \sqrt{\frac{\epsilon_r}{2} \left( \sqrt{1 + \left( \frac{\sigma}{\omega\epsilon} \right)^2} - 1 \right)} \quad (2.48)$$

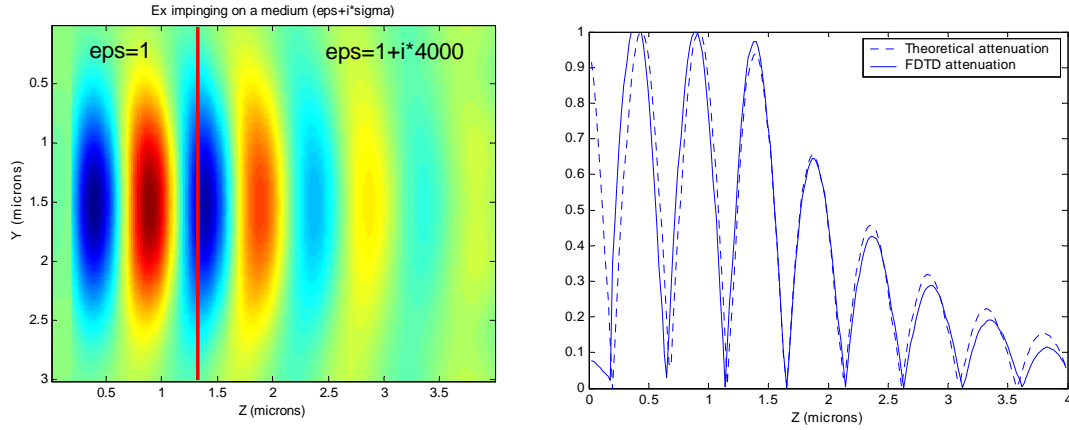


Fig.14: Benchmark of the lossy dielectric FDTD showing a comparison between theoretical behavior of E-field in lossy medium and FDTD simulation.

### 2.2.3.2 Modeling of metallic layers

The modeling of metallic materials involved in the high reflection coating of the grating coupler requires a modification of the equations presented above since losses induced by metals cannot usually be represented by a simple conductivity term. The complex refractive Index of a metal

can be written as  $n_c = n + i.k = \frac{ck}{\omega}$ , where  $c$  is the velocity of light,  $k$  the wavenumber and

$\omega = \frac{2\pi c}{\lambda}$  the angular frequency. The permittivity is then given by

$$\varepsilon_r^i = \varepsilon_1 + i.\varepsilon_2 = \varepsilon_r - i \frac{\sigma}{\varepsilon_0 \omega} = n_c^2 \quad (2.49)$$

So the permittivity and conductivity are given by

$$\begin{cases} \varepsilon_r = n^2 - k^2 \\ \sigma = 2nk\varepsilon_0\omega \end{cases} \quad (2.50)$$

and therefore the index of refraction can be expressed as

$$\begin{cases} n^2 = \frac{1}{2}\varepsilon_1 \left( \left[ 1 + \left( \frac{\varepsilon_2}{\varepsilon_1} \right)^2 \right]^{\frac{1}{2}} + 1 \right) \\ k^2 = \frac{1}{2}\varepsilon_1 \left( \left[ 1 + \left( \frac{\varepsilon_2}{\varepsilon_1} \right)^2 \right]^{\frac{1}{2}} - 1 \right) \end{cases} \quad (2.23)$$

The real part of the permittivity of metals such as gold are less than one in the spectrum region close to the 980nm wavelength of interest for this work. This causes instability of the numerical model due to a negative permittivity and requires the application of the Drude-Lorentz mode for metals to the FDTD scheme. The Lorentz model for Gold gives a frequency dependent expression of the permittivity that prevents the instability induced by having a negative real part of the permittivity. In this model the permittivity is given by

$$\boldsymbol{\varepsilon} = \boldsymbol{\varepsilon}_r + \frac{\boldsymbol{\varepsilon}_1}{\boldsymbol{\varepsilon}_2 + 2j\delta_0\left(\frac{\boldsymbol{\omega}}{\boldsymbol{\omega}_0}\right) - \left(\frac{\boldsymbol{\omega}}{\boldsymbol{\omega}_0}\right)^2} \quad (2.52)$$

The electric flux density is then given by

$$D_y(\boldsymbol{\omega}) = \boldsymbol{\varepsilon}_r \tilde{E}_y(\boldsymbol{\omega}) + \frac{\boldsymbol{\varepsilon}_1}{\boldsymbol{\varepsilon}_2 + 2j\delta_0\left(\frac{\boldsymbol{\omega}}{\boldsymbol{\omega}_0}\right) - \left(\frac{\boldsymbol{\omega}}{\boldsymbol{\omega}_0}\right)^2} \tilde{E}_y(\boldsymbol{\omega}) \quad (2.53)$$

One can introduce the an auxiliary variable  $S(\boldsymbol{\omega})$  so that

$$D_y(\boldsymbol{\omega}) = \boldsymbol{\varepsilon}_r \tilde{E}_y(\boldsymbol{\omega}) + S(\boldsymbol{\omega}) \quad (2.54)$$

Using the auxiliary differential equation (ADE) method one gets in the discrete form in time domain

$$\omega_0^2 \boldsymbol{\varepsilon}_2 \cdot S^{n-1} + 2\delta_0 \omega_0 \frac{S^n - S^{n-2}}{2\Delta t} + \frac{S^n - 2S^{n-1} + S^{n-2}}{\Delta t^2} = \omega_0^2 \boldsymbol{\varepsilon}_1 \cdot \tilde{E}_y^{n-1} \quad (2.55)$$

where  $S^{n-1}$  describes  $S$  at  $t=n-1$ . Thus one obtains the electric field value by the following set of equations

$$\begin{cases} S^n = \frac{(2 - \Delta t^2 \omega_0^2 \boldsymbol{\varepsilon}_2)}{(1 + \Delta t \omega_0 \delta_0)} S^{n-1} - \frac{(1 - \Delta t \omega_0 \delta_0)}{(1 + \Delta t \omega_0 \delta_0)} S^{n-2} + \frac{\Delta t^2 \omega_0^2 \boldsymbol{\varepsilon}_1}{(1 + \Delta t \omega_0 \delta_0)} \tilde{E}_y^{n-1} \\ \tilde{E}_y^n = \frac{D_y^n - S^n}{\boldsymbol{\varepsilon}_r} \end{cases} \quad (2.56)$$

The magnetic field is then obtained by (2.47). If  $\boldsymbol{\varepsilon}_2 = \mathbf{0}$  the Lorentz model reduces to the Drude

model for metals

$$\varepsilon = \varepsilon_d - \frac{\omega_p^2}{\omega \left( \omega + \frac{i}{\tau} \right)} = \varepsilon_d - \frac{\omega_p^2 \tau}{i\omega} + \frac{\omega_p^2 \tau}{i\omega - \frac{1}{\tau}} \quad (2.57)$$

where

$$\begin{cases} \varepsilon_1 = 1 \\ \omega_0^2 = \omega_p^2 \\ \delta_0 = \frac{-1}{2\tau\omega_0} \end{cases} \quad (2.58).$$

Finally, an important part of the FDTD success resides in an efficient way of handling the boundaries of the computation domain. The energy flowing through the boundaries must be tackled in a way that no artificial reflection is created that could interfere with the analyzed signal. The most common method to do so is to implement a perfectly matched layer (PML) scheme that is based on artificial medium properties to obtain perfect impedance matching at the boundaries interfaces as first described by Berenger [Berenger 1994]. It was empirically shown that the best PML results are obtained by varying the conductivities as a cubic function of the penetration inside the PML region. This graded impedance produces the best results and the lowest reflectivity at the boundaries interfaces. The coefficients  $C_1^D$  and  $C_2^D$  vary from 1 to 0.33 inside the PML region that was set to 10 cells. Similar coefficients are found for the magnetic field solution.

## **2.3 Grating coupler design and analysis**

### **2.3.1 What is the optimum shape for a grating coupler?**

Although the wave equation is approximated to obtain an analytical solution of the grating coupling strength, the perturbation technique helps get some insight into the grating behavior for design purposes. A good example is the approximation of the grating decay parameter  $\alpha$  as a function of the grating shape. It can indeed be shown, by solving equation (2.36) that the grating leakage rate for the  $m^{\text{th}}$  diffracted order is directly proportional to the square of the  $m^{\text{th}}$  component of the grating Fourier decomposition [Tamir 1977]. Considering a trapezoidal profile, the leakage rate is proportional to

$$\left\{ \begin{array}{l} Q_n = \left( \frac{\sin(n\pi\delta)}{n\pi\delta} \cdot \sin \left[ n\pi \left( \frac{d_1}{d} - \delta \right) \right] \right)^2 \\ \delta = \frac{d_1 - d_2}{2d} \end{array} \right. \quad (2.59)$$

Where  $d$  is the grating period, and  $d_1$  and  $d_2$  the trapezoid base and top widths respectively. This result demonstrates that the leakage rate is optimal for a rectangular profile where  $d_1 = d_2$  and a duty cycle defined of 50% the duty cycle being defined in this dissertation as the percentage of removed material within one grating period. In fact this effect is counterbalanced slightly by the fact that a grating with a high duty cycle has a lower average index than low duty cycle gratings, which consequently tends to shift the energy of the guided mode away from the grating,

decreasing the amount of modal intensity interacting with the corrugated surface and therefore decreasing the leakage rate. The highest leakage rates are therefore observed for a duty cycle between 40% and 50% as shown in Fig.11. An FDTD analysis of the radiation produced by gratings with four different sidewall profiles is shown in Fig.15. The exponential increase of the outcoupling length as a function of the sidewall angle confirms that rectangular gratings provide higher coupling coefficient.

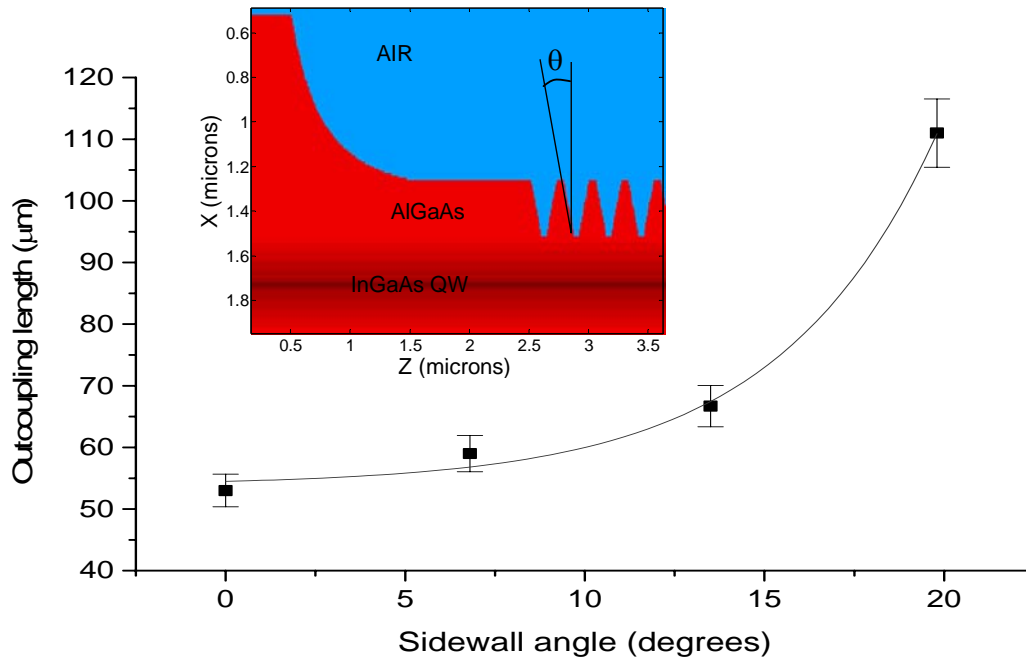


Fig.15: Plot of outcoupling length versus sidewall angle  $\theta$  obtained by FDTD modeling.

### 2.3.2 Choice of the grating period

The period of the grating coupler must be chosen to satisfy the following two requirements:

- maximize the coupling efficiency into one order
- decrease the effective relectivity

The period of the grating coupler must then be chosen so that only one order of diffraction is allowed in the substrate. This condition is met by the following condition

$$\Lambda < \frac{2\lambda}{n_{eff} + n_s} \quad (2.60)$$

where  $\lambda = 980nm$  ,  $n_s = 3.54$ , and  $n_{eff} = 3.31$  , then  $\Lambda < 286nm$  .

Gratings with two different periods 275nm and 325nm were fabricated on a AlGaAs/GaAs structure grown by IQE corporation. The power diffracted into the -1 order in the air and the substrate was measured and summed. Despite chip to chip variations, the results showed that the slope efficiency is about 45% larger for a 275nm period grating. This confirms the study done by [Hagberg 1995] that indicated larger slope efficiencies are obtained for negative detuning with respect to the second order Bragg resonance at 290nm by suppressing the second diffracted order in the substrate. Consequently, we decided to focus our efforts on negatively detuned grating couplers with 270nm or 275nm periods.

### 2.3.3 Theoretical reflectivity of detuned grating coupler

One of the key advantages of the detuned grating coupler is the low reflectivity obtained when coupling light outside the cavity. Using coupled mode theory, the in-plane power reflection coefficient is given by [Yariv 1973]

$$R = \frac{\kappa^2 \sinh^2(\alpha L)}{\alpha^2 \cosh^2(\alpha L) + \delta \sinh^2(\alpha L)} \quad (2.61)$$

where  $L$  is the grating length,  $\kappa$  is the grating coupling coefficient,  $n_e$  the effective index. The attenuation  $\alpha$  and detuning coefficient  $\delta$  are given by

$$\begin{cases} \alpha = \sqrt{\kappa^2 - \delta^2} \\ \delta = \beta - \beta_0 = 2\pi \left( \frac{1}{\lambda} - \frac{n_e}{\lambda_B} \right) \end{cases} \quad (2.62)$$

$\lambda_B$  is the second order Bragg wavelength for the grating period considered. In the practical case investigated in this dissertation, we consider a 270nm grating period, an effective index of refraction of 3.31 and therefore the Bragg wavelength for this grating is located at

$$\lambda_B = n_e \Lambda = 894nm \quad (2.63)$$

The period provides an 83nm detuning from the emission wavelength located at 977nm. The coupling coefficient  $\kappa$  is given by

$$\kappa = \frac{1}{\Lambda} \left( \frac{\Delta n_e}{n_e} \right) \quad (2.64)$$



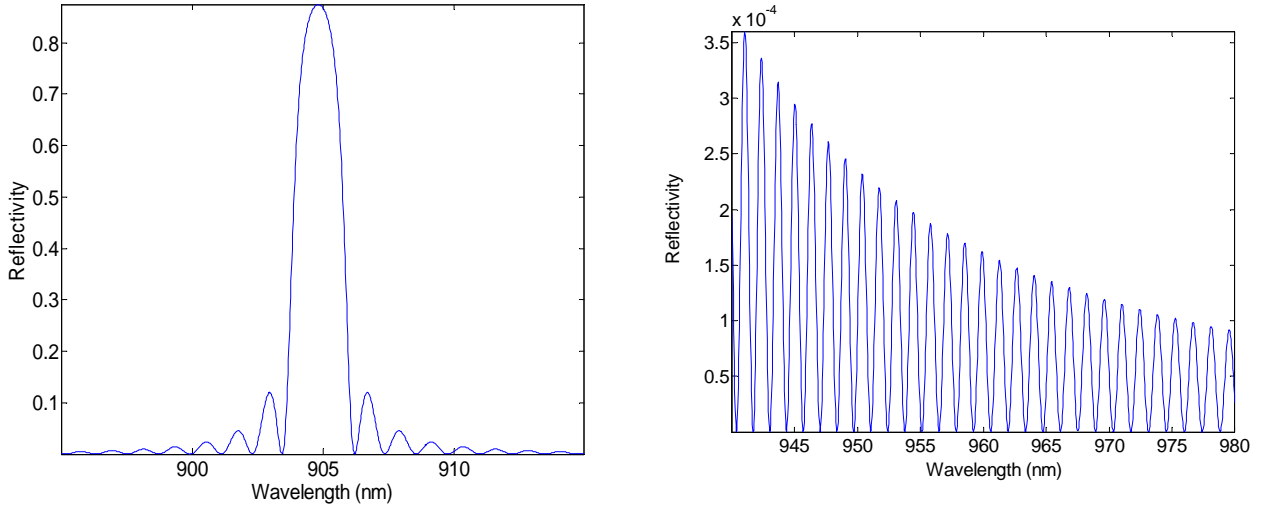


Fig.16: Reflectivity of a 100micron long, 50% duty cycle, 250nm deep, 270nm period grating coupler as a function of wavelength. At the emission wavelength of 977nm, the reflectivity is less than  $10^{-4}$ .

This result is in agreement with other numerical methods [Butler 1982]. To calculate the coupling coefficient, one needs to calculate the variation of effective index between the mode supported in the tooth of the grating and the mode supported in the groove. These two modes can be calculated using the Galerkin method and the resulting coupling coefficient, assuming a 50% duty cycle rectangular grating, is given by

$$\kappa = \frac{1}{\Lambda} \left( \frac{\Delta n_e}{n_e} \right) = 170 \text{cm}^{-1} \quad (2.65)$$

The reflectivity provided by a 100 micron long grating is shown in Fig.17 as a function of wavelength. A length of 100 micron was considered since power drops at  $1/e^2$  at this distance

of interaction.

### 2.3.4 Effect of low reflectivity mirror on device performance

The external differential efficiency of the device depends strongly on the facet coatings that control the mirror output losses. Usually a 95%/HR and 2-4%/AR coatings are deposited on the facets to increase the power output from one side. In the case of the GCSEL, the grating coupler reflectivity reaches values as low as  $10^{-4}$ . Given the mirror's reflectivity  $R_1$  and  $R_2$ , the differential efficiency is given by

$$\eta_a^{-1} = \eta_i^{-1} + \frac{\alpha_i L}{\eta_i \cdot \ln\left(\frac{1}{R_1 R_2}\right)} \quad (2.66)$$

where internal quantum efficiency  $\eta_i = 0.956$  and losses  $\alpha_i = 2.5\text{cm}^{-1}$ . To understand the effect of the low reflectivity on the device behavior, we modeled the GCSEL device by replacing one cleaved facet by a low reflectivity of  $10^{-4}$  to simulate the grating effective reflectivity. The device active region is 2mm long and 60  $\mu\text{m}$  wide. The effect of the length of the grating is neglected. The reflectivity of the uncoated back facet is 0.32. The carrier density is calculated using 40 Hermite-Gauss polynomials. Temperature effects were neglected.

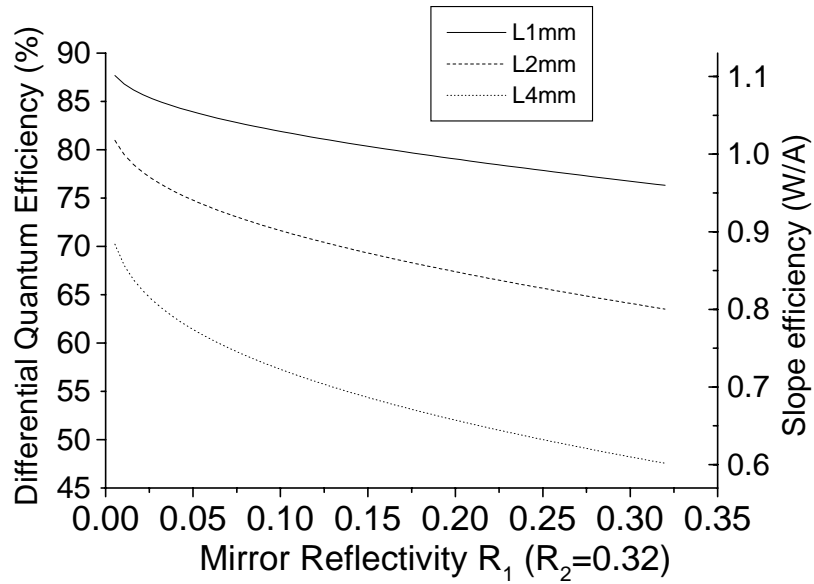


Fig.17: Plot of the Fabry-Perot device efficiency versus output mirror reflectivity for different lengths of 1mm, 2mm, and 4mm.

The propagation step of the finite-difference beam propagation model is  $2\mu\text{m}$  and 240 points are used to sample the contact stripe in the X direction. The calculation starts by launching a 5mW Gaussian beam inside the cavity that will propagate for 19 iterative loops. The large difference between the power measured at the back facet and the grating side stems from the large difference in effective reflectivity between the two facets. As a result the COD level of the uncoated facet GCSEL device is increased since the intensity level hitting the uncoated back facet is lowered by a factor of 27 when compared to power measured at the beginning of the grating. The carrier density distribution follows closely the electric field intensity since both are coupled through the stimulated emission process.

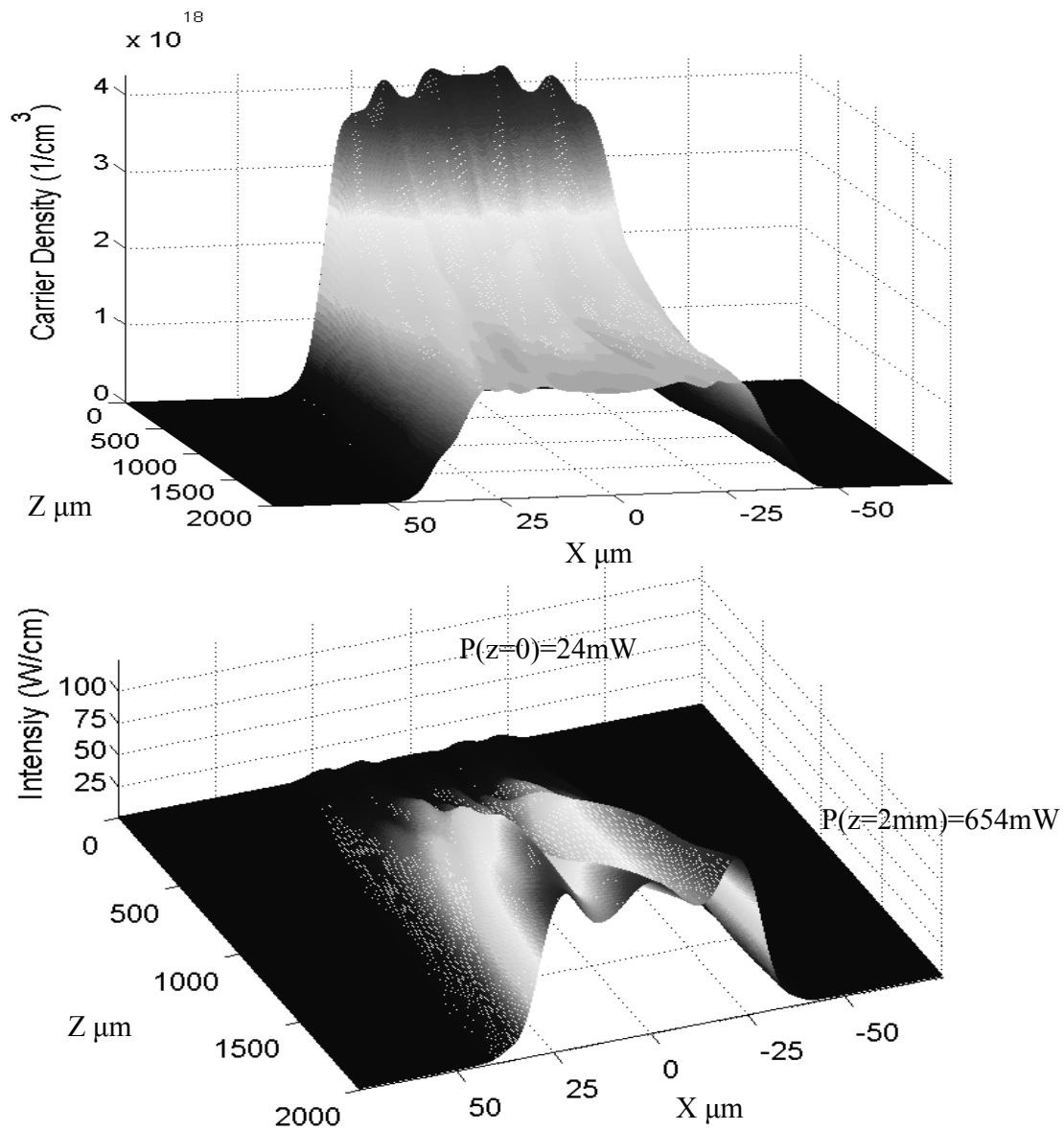


Fig.18: Plot of carrier density (bottom) and electric field intensity (top) inside the cavity of 2mm long by 60μm wide device for I=1A obtained after 19 iteration loops by averaging 5 loops.

The nonlinear effects triggered by the antiguiding factor are responsible for the filaments propagating inside the cavity. The intensity distribution is typical of a single pass gain device.

Because the filaments are not stable modes of the cavity, it is necessary to average over a few round trips to obtain the intensity distribution inside the device [Marciante 1996]. Each round trip takes 44ps to complete. The intensity shown in Fig.18 is therefore averaged over 220ps. This model is useful to investigate the effect of the stripe geometry on the spatial transverse mode profile. However, the model only cares for one wavelength and does not include the amplified spontaneous emission process occurring over the length of the device and responsible for the increase of power experimentally observed between 1mm long and 2mm long GCSEL devices.

### **2.3.5 Low reflectivity wet-etched structure**

The InGaP wet-etch stop layer is located at 250nm above the top of the GRINSCH so that the overlap between the modes propagating in the active and passive region is maximized while good outcoupling is performed by gratings with reasonable aspect ratio. In our structure, a 50% duty cycle, 250nm deep grating, corresponds to a 50 $\mu$ m outcoupling length. Finite-difference time domain was used to determine the effective reflectivity of the step as shown in Fig.19. More than 99.8% of the input power is found to be transmitted into the passive region. The difference in effective index between the active and wet-etched passive region, obtained by the Galerkin method, is  $1.1 \times 10^{-3}$ , giving a theoretical effective Fresnel power reflectivity at this interface of  $2 \times 10^{-7}$ . The excellent overlap between the mode profiles propagating in the active and passive region results in suppressing effectively any feedback inside the cavity from this interface and also enhances the device efficiency by decreasing scattering losses.

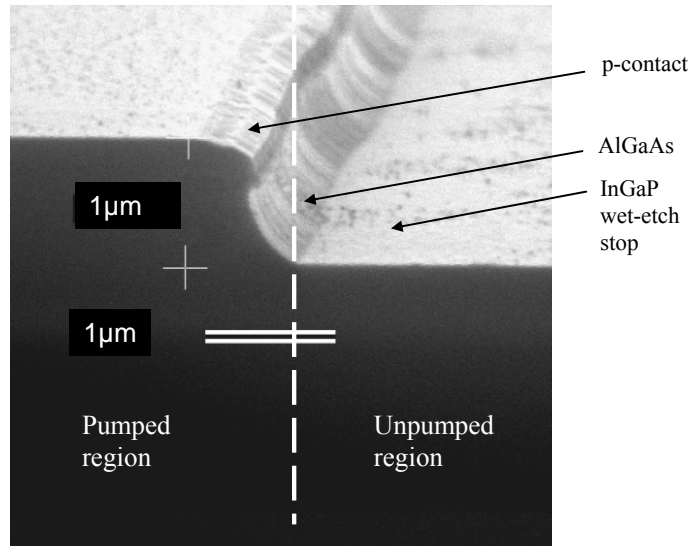


Fig.19: Scanning electron microscope of the wet-etched transition between the active and the passive area where the grating is integrated.

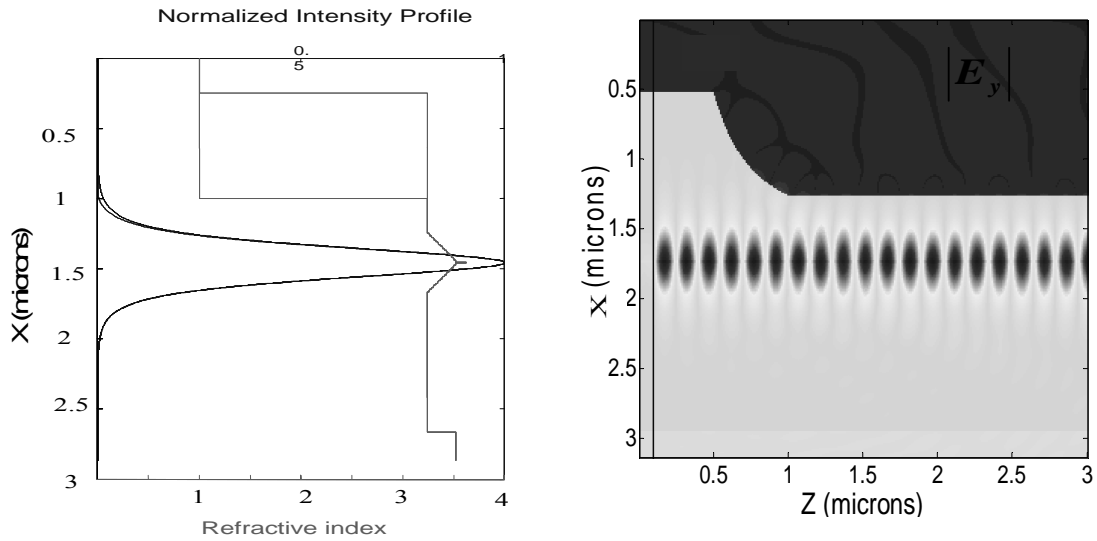


Fig.20: Intensity profile of the guided mode in the active and passive region obtained by finite element method (left) and FDTD propagation of E field through the modeled wet-etched transition (right).

## 2.3.6 Improvement of grating coupler directionality

### 2.3.6.1 FDTD calculation

We applied the FDTD modeling of metallic layers to the analysis of high reflection coating deposited on the grating coupler. This analysis aims at determining which scheme will be employed to obtain highly directional emission towards the substrate and potential second optical element. We considered a 250nm deep grating with 50% duty cycle, covered by either a layer of gold or a combination of dielectric and gold [Evans 1989]. The refractive index of the dielectric was taken to 1.78 while the permittivity of gold was given by (2.57) with the following standard parameters for Gold around 1 $\mu$ m emission wavelength:

$$\left\{ \begin{array}{l} \varepsilon_d = 8 \\ \omega_p = 8eV / \hbar \\ \tau = \frac{1}{0.008\omega_p} \end{array} \right. \quad (2.67)$$

We assumed a perfectly planarized coating with filled grating grooves. The dielectric thickness on top the grating grooves is set to 130nm. The grating length was set to 50 $\mu$ m. The outcoupling length is greatly reduced, in the case of gold layer alone, to 24  $\mu$ m. The losses associated with the gold coating are estimated by calculating the value of the vertical component of the power flow

at the lower edge of the calculation domain when 67% of the propagating light is outcoupled

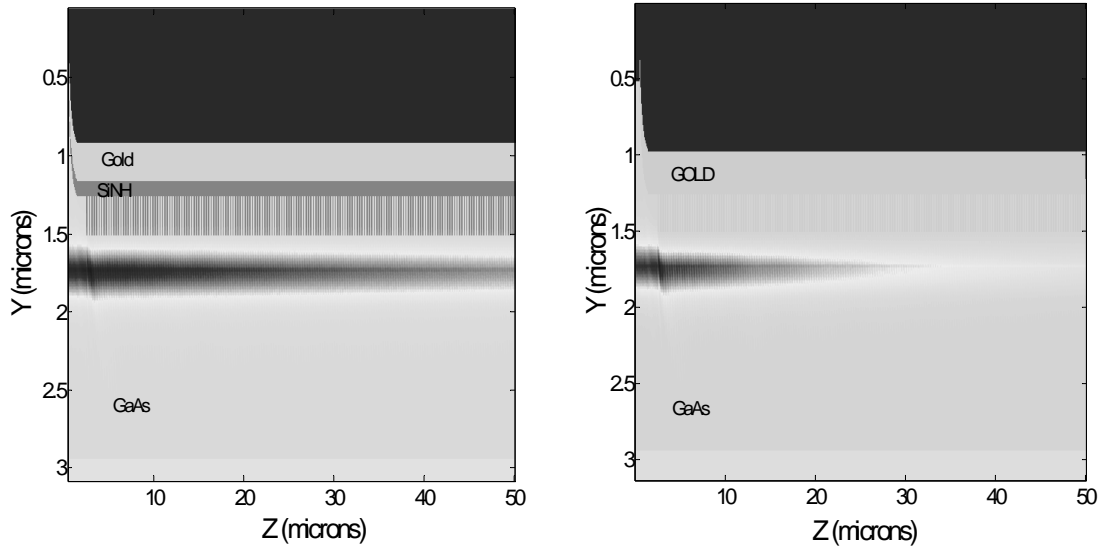


Fig.21: Horizontal component of the power flow representing the decay of propagating power inside the waveguide when the grating coupler is coated with gold only (right) or a combination of dielectric and gold layers (left).

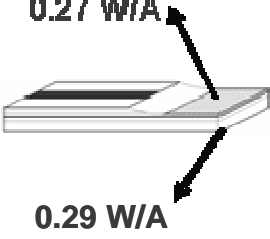


Compared to the dielectric and gold combination, the gold only coating scheme generates 28% more losses according to the FDTD calculation. The reflectivity, given by the horizontal component of the power flow calculated at the beginning of the propagation, is also increased by almost an order of magnitude from 0.3% to 2% in the case of the gold only coating. The outcoupling length for the dielectric and gold combination is  $62\mu\text{m}$ , a slight increase when compared to outcoupling without high reflection coating due to the decrease in index contrast.



### 2.3.6.2 Experiment

To verify experimentally the claim that dielectric and gold layer combination provides a more efficient high reflection coating, a few devices were coated with a 130nm dielectric layer. Before being placed inside the thermal evaporator, the dielectric layer was removed from the top of the p-contact. Other devices from the same wafer were also placed inside the thermal evaporator but did not have the dielectric coating on top of the grating. A 225nm layer of gold was deposited on both sets of devices. The active length for all devices was 1.7mm. The substrate of all devices was coated with 130nm antireflection SiNH dielectric layer. The output power transmitted through the substrate was measured with 500ns pulse at 1kHz repetition rate and compared to total power coupled in the air and through the substrate for devices without HR coating on the grating and AR coating on the substrate. The results are summarized in table 5. The combination of dielectric and gold layers is more than twice more efficient than the case of Gold alone. When compared to the FDTD calculation, the extra losses associated with the gold only configuration could be due to clipping of portion of the light by the n-contact caused by a 10 $\mu$ m shift of the peak intensity occurring after propagation in the substrate. Since the gold only HR coating outcouples light faster, more light is expected to be clipped by the n-type metal contact. Using the ratio between powers measured from the back cleaved facet and the grating output, we calculated that effective reflectivity for the dielectric and gold HR scheme was between three and ten times lower than for the gold only HR coating.

Table 5: Experimental comparison of high reflection coating performance.

HR coating	NO	Au	SiNH + Au
Slope Efficiency	 <p>0.27 W/A</p> <p>0.29 W/A</p>	 <p>0.24 W/A</p>	 <p>0.57 W/A</p>

Following this analysis, we conclude that it is important to use the dielectric and gold combination to enhance the directionality of the emission output. This combination eliminates the extra losses associated with depositing gold inside the grooves.

## CHAPTER 3: FABRICATION

The fabrication of a grating-coupled surface emitting laser involves features ranging from 30nm to several microns and a wide range of micro-fabrication equipment for deposition, patterning and etching. All processes are wafer-based and leverage off the experience accumulated in the integrated circuit industry so that several hundreds of devices can be produced out of a single batch. We will start by detailing the processes involved in the wafer processing of laser diodes. We will then explain the grating coupler fabrication steps, including patterning by electron beam lithography and etching. We will emphasize the singularities associated with fabricating sub-micron features, such as proximity effect and aspect ratio dependent etching.

### 3.1 Laser diode fabrication

In this work, laser diodes are gain-guided with stripes ranging from 10micron to 100 $\mu$ m wide. The standard process for laser diodes has to be modified to accommodate the integration of the grating coupler and the light extraction through the substrate. The wafer used in this work was grown by Molecular Beam Epitaxy (MBE) by Coherent Inc on (100) GaAs substrate. The wafer flats are oriented according to European standards, the major flat being oriented parallel to the (011) plane, unlike the US standard where the major flat is parallel to the (0 $\bar{1}\bar{1}$ ) plane.

### 3.1.1 p-contact processing

The following steps were performed by Coherent Inc. due to the high temperature required to evaporate the metals used for p-contact. The processing starts by defining the stripe width and length by contact lithography, followed by wet-etching of the area where the grating coupler will be patterned. A 20nm InGaP etch-stop layer was integrated in the growth at 250nm above the graded AlGaAs waveguide to enable precise positioning of the grating coupler with respect to the quantum well (Kjellberg 1993). Since the stripes are typically perpendicular to a major flat, the etched sidewalls profiles may be inverted as shown in Fig.22. This may create some contact problems if not taken into consideration during photolithography. This problem is usually not critical for the wide stripes used for this work but becomes important when the current is injected through a bonding pad in single-mode ridge lasers for instance. The experimental profiles shown in Fig.22 were obtained by a solution of  $\text{H}_3\text{PO}_4:\text{H}_2\text{O}_2:\text{H}_2\text{O}$  at ratios of 0.75:1:3 for 2minutes. The difference between the sidewall profiles orientation is highlighted on the SEM pictures. A 100nm thick layer of  $\text{Si}_3\text{N}_4$  is then deposited using Plasma Enhanced Chemical Vapor Deposition (PECVD) to insulate the contact around the stripe. The dielectric layer is removed from the top of the contact stripe using another contact lithography step and a reactive ion etcher (RIE) to enable ohmic contact as shown in Fig.23. The metal layers (Ti/Pt/Au) are then evaporated on the wafer and lifted off at both edges of the stripe to enable the integration of the grating coupler.

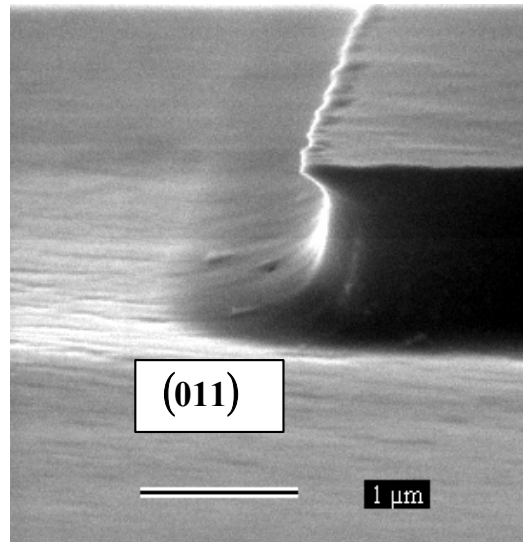
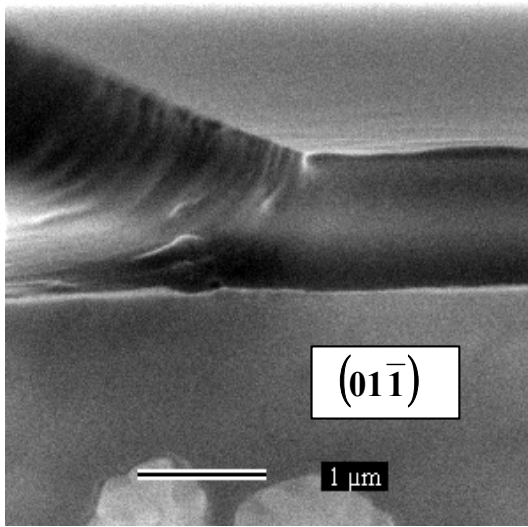
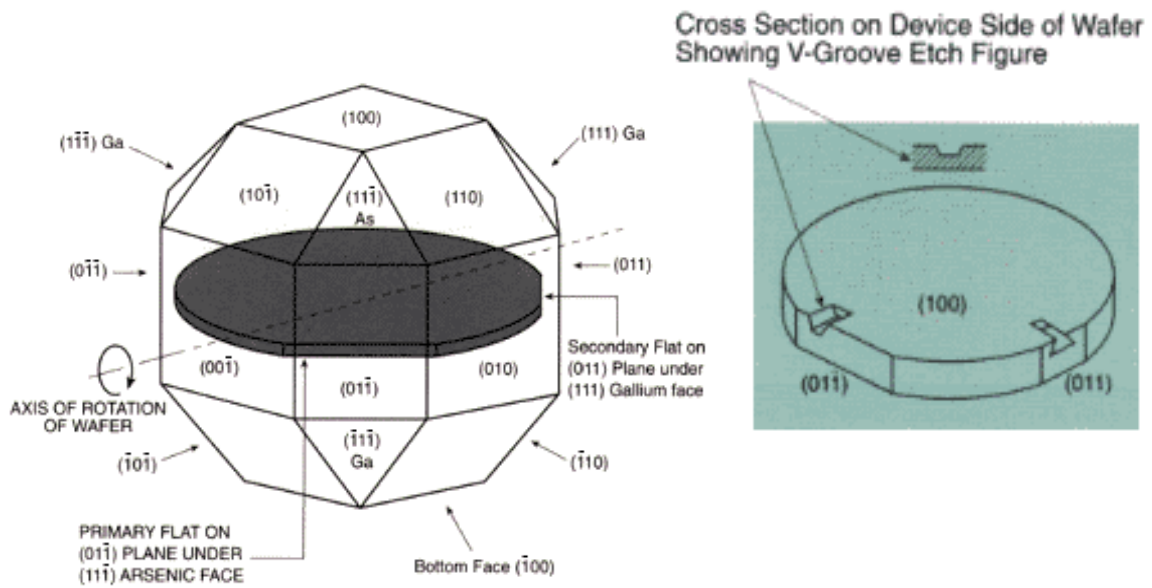


Fig.22: Wet-etch sidewalls profiles of GaAs with respect to the major flats (top). The flats configuration shown is US standard (source: Tyco Electronics).

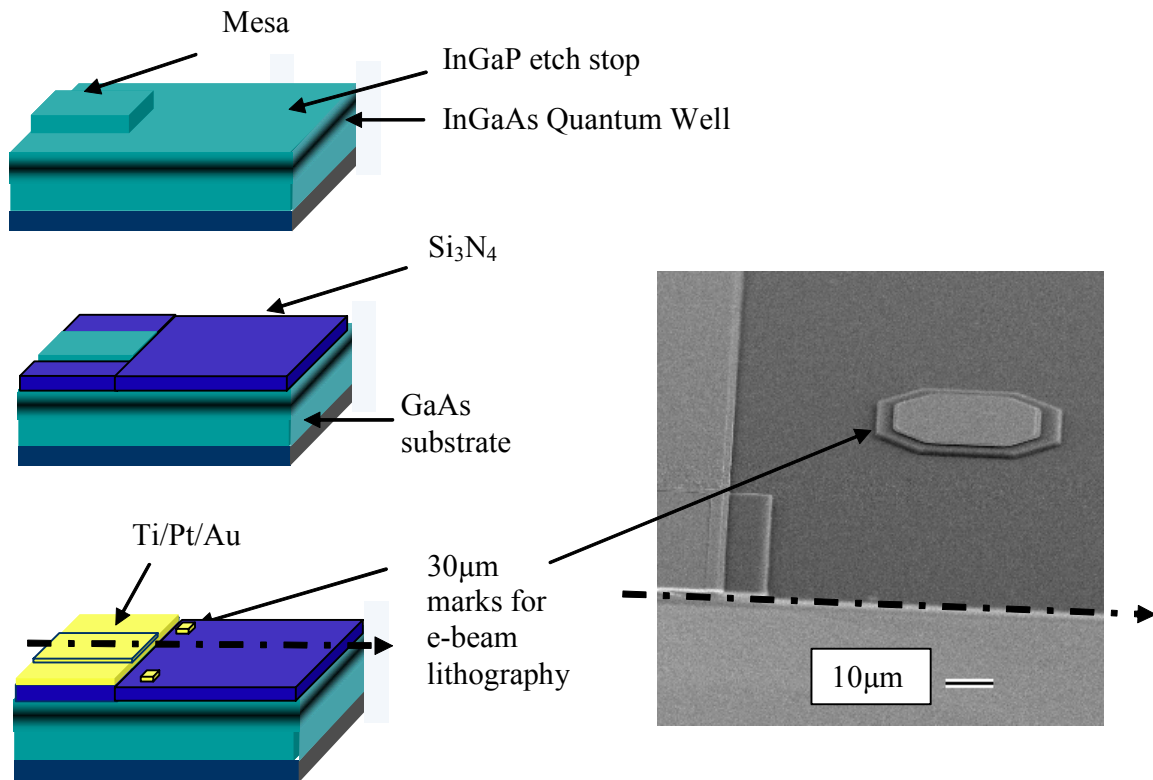


Fig.23: p-contact processing prior to grating coupler integration.

### 3.1.2 n-contact processing

The wafer is thinned down to 150 µm to decrease the device resistivity and enable good cleaving. Another polishing step was added at CREOL in order to remove pits created by the standard laser diodes polishing step and enable integration of optical elements on the GaAs substrate. The wafer was first polished with 0.3 µm Al<sub>2</sub>O<sub>3</sub> powder that was mixed to distilled water for about

15minutes. The sample was kept rotating to produce a flat surface. Then NaOCl was added for a few minutes to produce a mirror-like finish. This technique was introduced as early as 1964 by Reisman and Rohr but the mechanism was only explained in 1989 by Higuchi using Raman spectroscopy. The technique is known as chemical-mechanical polishing since the reaction products  $\text{Ga}_2\text{O}_3$  and  $\text{As}_2\text{O}_3$  created by the active oxygen are removed by the friction due to the polishing cloth. The basic chemical equations are shown in Fig.24.

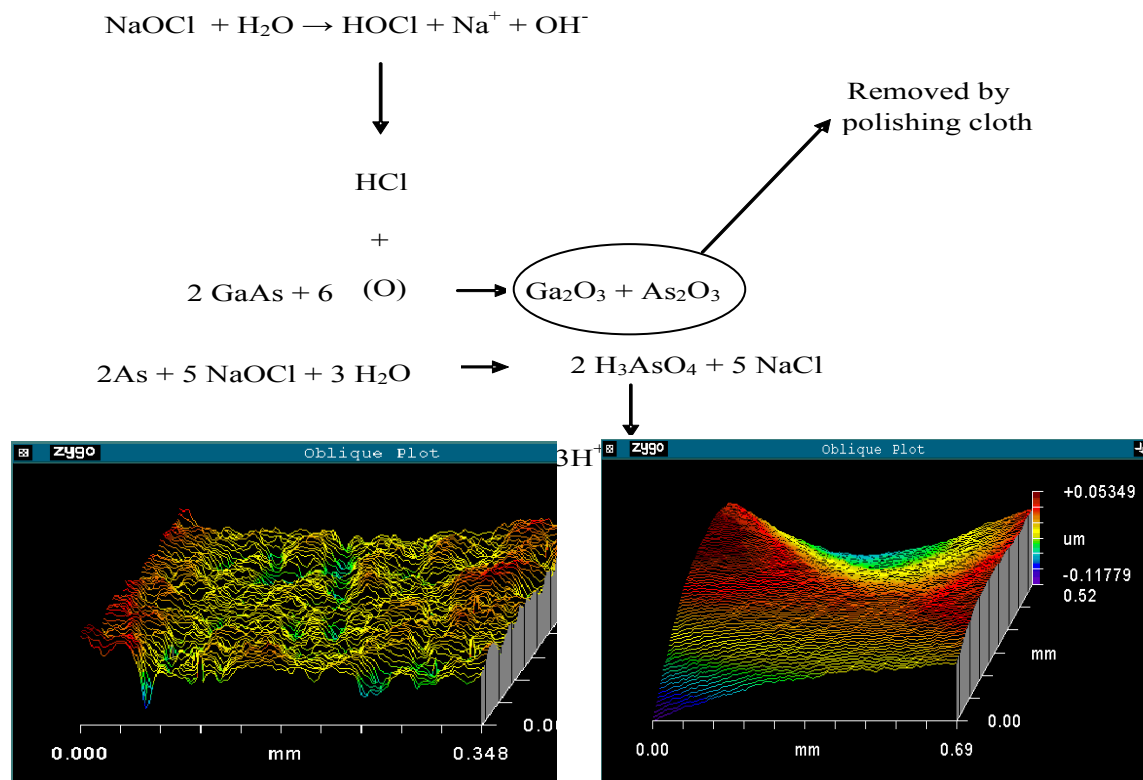


Fig.24: Polishing mechanism of GaAs by NaOCL and ZYGO white light interferometer profiles of GaAs substrate before and after polishing.

The polished GaAs substrate was then inspected using a white light ZYGO interferometer. The waviness seen on the right profile in Fig.24 is due to a non perfectly flat sample. The height variation is approximately 125nm over a 500 $\mu$ mX500 $\mu$ m area and may affect the wavefront exit angle. This problem may be solved by using a high-end polishing tool dedicated to wafer polishing. After polishing, the sample is cleaned with acetone and isopropanol before being plunged in a 10% HCl solution for 1min to remove any oxide layer created during the polishing step. The sample is then mounted p-side down on a piece of GaAs using PC3 coating from Futurex to avoid breaking the thin sample. A 1 $\mu$ m thick layer of negative resist NR7-1000PY from Futurex is spun on the sample and baked at 150°C for 1min. The sample is then mounted on a 4" silicon wafer using crystal bond and placed on a Quintel front to back aligner. Using infrared viewers, the p-contact gold marks are aligned to the n-side mask and exposed for 8s at a wavelength of 365nm. If the sample is smaller than 1 inch in diameter, only one viewer can be used but it is usually enough for correct alignment down to approximately 10 microns accuracy. The sample is then post-baked at 100°C for 1min and demounted from the silicon wafer by sliding the sample gently during post-bake. The pattern is developed in a 3:1 solution of RD<sub>6</sub>:H<sub>2</sub>O for 80s and rinsed with distilled water for 30s and then blow dried with nitrogen. The resist NR7-1000PY was chosen for its unique properties that enable proper metal lift-off by creating an inward sidewall profile after development as shown Fig.25. After developing the pattern, the sample is placed inside an Edwards thermal evaporator where a standard Ni/Ge/Au n-metal contact is deposited with thickness of 4nm, 20nm and 350nm respectively. The Ni layer is used as an adhesion layer and Ge is used to allow diffusion of the contact inside GaAs during



annealing.

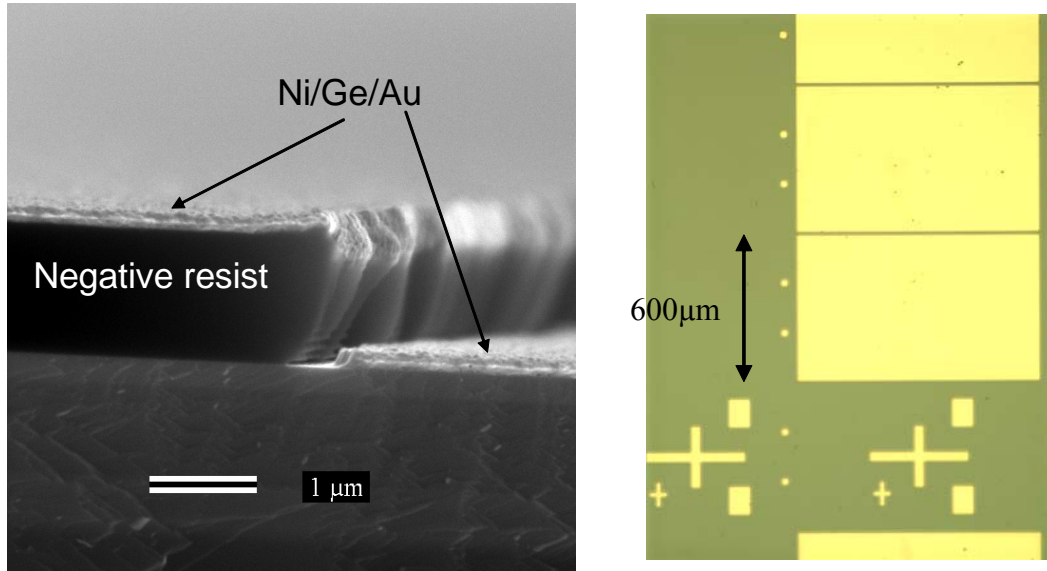


Fig.25: SEM picture of negative resist profile after development and metallization (left) and microscope picture of gold marls used for front to backside alignment (right).

The sample is then placed in an acetone bath overnight and finally in a RR2 (Futurex) bath at 70°C for 5min to achieve metal lift-off. The lift-off technique is used to open windows in the n-contact to enable light extraction through the substrate. The sample is then annealed at 400°C for 30s with a rapid thermal annealer. During the alloyed contact formation, Au reacts with the Ga atoms to form a variety of alloys. Ge then diffuses into GaAs to occupy the Ga vacancies created by the alloys formation and produces a heavily n-type doped substrate. A typical device resistance of  $2.5 \times 10^{-4} \Omega \cdot \text{cm}^2$  was measured from the current versus voltage curve. The dielectric

layer protecting the area where the grating is integrated is removed by reactive ion etching with a standard process involving carbon tetrafluoride (CF<sub>4</sub>) and Oxygen following the process described in Table 6. The mechanisms of plasma etching will be explained in more details in the next section.

Table 6: Typical process used to remove Si<sub>3</sub>N<sub>4</sub> dielectric layer before grating integration.

<b>CF<sub>4</sub></b>	<b>O<sub>2</sub></b>	<b>RIE power</b>	<b>Pressure</b>	<b>Etch rate</b>
36 sccm	4 sccm	75W	40mT	~ 80nm/mn

### **3.2 Grating coupler fabrication**

The fabrication of the grating coupler typically requires precise control of the pattern features below 150nm for a 270nm period grating. The pattern transfer requires precise depth control as well as vertical sidewalls since the grating coupling coefficient and reflectivity was shown to depend strongly upon duty cycle and depth. We will first explain the pattern direct writing procedure using electron beam lithography before detailing the pattern transfer and plasma etching mechanisms involved in the grating fabrication process.

### 3.2.1 Electron beam lithography (EBL)

The electron beam lithography (EBL) system is a system of choice to write small features down to 10nm for a variety of applications. The first waveguide grating couplers fabricated by e-beam were patterned at Cornell university in 1973 [Turner 1973]. Since then, the flexibility of EBL has been successfully applied to the fabrication of various straight [Tiberio 1991] or circular [King 1992] second-order gratings for surface-emitting lasers. The basic principle of EBL is to control a beam of electrons across a thin film of resist sensitive to the electrons radiation. This function can be achieved by converting a scanning electron microscope (SEM) using a module such as the Naby Pattern Generator System (NPGS) or can be a system fully dedicated to patterning such as the Leica EBPG 5000+. Both systems were used at the College of Optics and Photonics and will be briefly compared. In this section, we will explain the basic principles of electron beam lithography before detailing the characterization of two e-beam resists. We will then explain how to exploit the e-beam flexibility to taper the grating strength by proper Computer Assisted Design (CAD) and good exposure dose control.

#### *3.2.1.1 Electron beam direct-write basic principles*

An electron source typically sits at the top of a typical EBL column (Fig.26). The electrons are produced either by applying heat (thermoionic source) or an electric field (field emission source) to a conducting filament. Two or more lenses, electrostatic or magnetic, are used to condense

the beam. As in an optics system, a stigmator is used for correcting any astigmatism in the beam. The beam is spatially cleaned and centered in the column by an aperture, and finally, an electron detector for assisting with focusing and locating marks on the sample

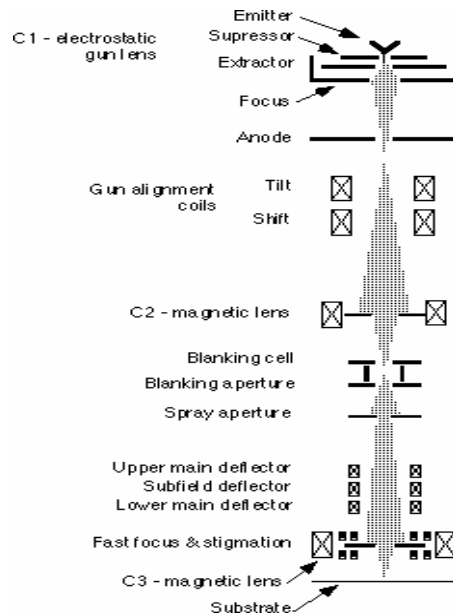


Fig.26: Elements of an EBL column (example of Leica Vectorbeam writer).

### 3.2.1.2 LEO 360 with NPGS versus Leica EBPB 5000+

The NPGS equipment offers a cost-effective way to obtain very small features. It is controlling the electron beam of a LEO 360 scanning electron microscope equipped with an electrostatic beam blanker from Scan Service corporation. The maximum allowed acceleration voltage is

30kV and can typically write features as small as 40nm in 200nm thick resist at a current of 30pA. The system is able to write very complex polygons with up to 200 vertices using a vector scan mode which, unlike the simpler raster mode, directs the beam to areas where patterns are written only. The system uses a 16 bit digital to analog converter (DAC) which means that patterns can be written with up to  $2^{32}$  pixels. However the DAC board speed is limited to 100kHz and without a laser interferometric stage, it is limited to single field of about  $400\mu\text{m} \times 400\mu\text{m}$  because the stitching accuracy is lower than  $10\mu\text{m}$ . The automatic alignment, although possible, also suffers from the stage inaccuracy and is practically unusable. On the other hand, for a much higher price of course, a dedicated electron beam system will write features down to 10nm on areas as large as a 5" plate. Also, the Leica e-beam system is capable to write small features with currents as high as a few nA, about two orders of magnitude higher than the NPGS which usually writes at a current of 30pA. The total writing time is defined as the dwelling time all pixels plus the scan coils settling time. The dwelling time for each pixel is defined by

$$t = \frac{\text{Area Dose} \times \left( \frac{\text{Field length}}{\# \text{ pixels}} \right)^2}{\text{Current}} \quad (3.1)$$

The NPGS writing speed is usually limited by the digital to analog throughput which is limited to 100 kHz (specifications for board DT2823, Data Translation Inc.). Therefore, if the dwelling time is too small, the number of pixels has to be decreased to allow the NPGS to correctly address the grid.

Table 7: Comparison between SEM based NPGS system and Leica EBPG 5000+

	<a href="#">JC Naby Lithography Systems</a>	<a href="#">Leica Lithography Systems Ltd.</a>
Model	NPGS / SEM LEO 360	EBPG 5000+
Electron source	Tungsten filament	Thermal field emitter
Alignment	Manequal or Automated (limited by stage)	Automated
Stitching	>10 $\mu\text{m}$	30nm (100 $\mu\text{m}$ field) 80nm (1000 $\mu\text{m}$ field)
Energy	0-40 kV (30kV in practice)	20 - 50 kV (100kV optional)
Beam current	0-500pA	100pA – 200nA
DAC speed	100 kHz	500Hz - 25MHz
Working distance	7mm	40mm
DAC	16 bits	16 bits
Pattern shape	Any	Any
Max. # of doses per pattern	30	232
Writing method	Vector scan	Vector scan
Max. field size	~ 400 $\mu\text{m}$ x400 $\mu\text{m}$	800 $\mu\text{m}$ x800 $\mu\text{m}$ (50kV)
Stage control/accuracy	Automated/10 $\mu\text{m}$	Automated/0.6nm (Laser interferometer HeNe)
Maximum sample size	4"	5"
Aberration corrections	Manequal (gold standard)	Automatic
Off-axis corrections/ Height sensor	No/No	Yes/Yes
Control computer	DOS/Windows	Alpha console / X Terminal

### 3.2.1.3 *The proximity effect*

As the beam of electrons hits the resist, the initial electron trajectories are affected by a broadening effect during propagation called forward scattering. Once they hit the substrate they can experience large deflection angles due to elastic scattering. This second effect is known as electron backscattering and is mainly responsible for the dose variation experienced by densely patterned features also known as proximity effect. When accelerated by higher voltages (20kV), electrons are buried deeper in the substrate, decreasing the magnitude of the proximity effect [Kyser 1975]. However, higher voltage also extends the backscattering range. The proximity effect is shown in fig.27 for the case of densely packed lines found in patterns such as a diffraction grating. The single-pass lines were patterned in a 400nm thick PMMA resist layer at 30kV with a dose of  $200\mu\text{C}/\text{cm}^2$  using the NPGS system. As shown on the SEM picture, although each line is exposed with the same dose, the middle line is affected by the electrons backscattered from the doses applied to the edge lines. Consequently, the effective dose received by the resist in the middle of the pattern is higher than on the edges, affecting the feature width and may prevent clearing the resist. The dose needed to clear an isolated line is therefore always higher than the dose of densely packed lines. In some cases this non-uniformity needs to be compensated for, especially when small features need to be patterned next to large areas. Another consequence of the proximity effect is the dependence of the clearing dose upon the feature width as shown in fig.27.

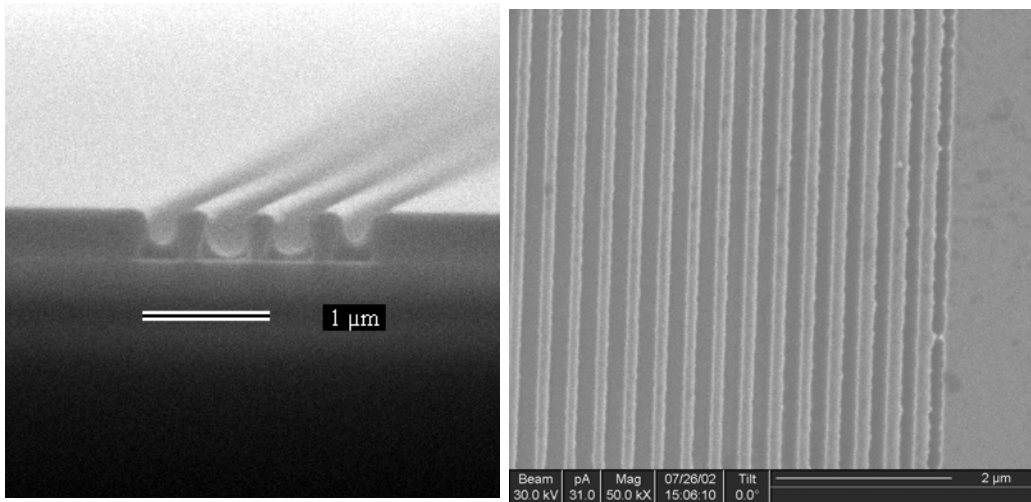


Fig.27: Proximity effect on densely packed lines. The left SEM show a cross section of patterns written in 400nm thick PMMA. The grating duty cycle on the edge of the pattern is affected by the proximity effect (right).

CAD linewidth	30nm	60nm	90nm	120nm
Clearing dose	140uC/cm <sup>2</sup> (+-10)	90uc/cm <sup>2</sup> (+-10)	60uC/cm <sup>2</sup> (+-10)	<50uC/cm <sup>2</sup>

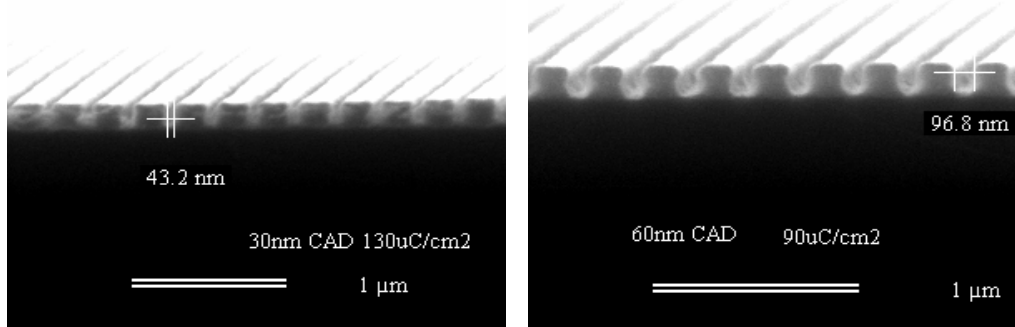


Fig.28: Clearing dose as a function of CAD linewidth for a 270nm period grating. The wider features typically require a lower dose to clear because of the proximity effect. The resist used is ZEP 2:1 spun at 3500RPM for 40s.



### 3.2.1.4 Defining and writing the grating coupler with the Leica EBPG

- Pattern grid and field size

For a given field size, the pattern is sampled on a grid of  $2^{32}$  pixels. Thus, for a pixel increment of 10nm, the corresponding field size  $L$  is given by

$$L = (2^{16} - 1) \cdot 10^{-3} = 655.35 \mu m \quad (3.2)$$

This field was used to write the grating couplers since its length allows the extraction of 99.99998% of the light, assuming a 250nm deep, 50% duty cycle grating. The field dimensions are especially important to sample patterns for grating couplers since the period must be a multiple of the pixel increment or phase errors will be introduced. The pattern file is typically written in GDS2 format and converted to the Leica file format using a program called CATS that fractures the pattern appropriately as a function of field size, format, and number of doses.

- Control over duty cycle variation

The proximity effect can be corrected by assigning different doses to the pattern. This feature is also very helpful to tailor the grating parameters. We showed in Chapter 2 that the grating coupler strength, represented by the inverse of the outcoupling length, depends strongly upon the grating duty cycle and depth. In order to obtain efficient substrate beam shaping or direct fiber coupling from the device, it is useful to reshape the beam into a more symmetric profile by tailoring the grating leakage rate through asymmetric grating couplers. Such graded strength

couplers also minimize the impedance mismatch between the waveguide and the grating region, decreasing scattering losses. Several techniques have been reported to control the leakage rate of grating couplers. Miyagana and al. first showed theoretically that grating couplers with fixed duty cycle and linearly varying depth can approximate Gaussian intensity output profile [Miyagana 1981]. Output beams approaching a gaussian profile were obtained from gratings fabricated using a specially modified ion etcher equipped with a moving slit to control the grating depth locally [Bates 1993]. Another technique used a dithering mask to create a tapered waveguide thickness where a uniform grating coupler could then be integrated to obtain symmetric output profiles [Kipfer 2000]. It was also shown theoretically that gratings with varying duty cycle and constant depth can produce output beams with symmetrical intensity profiles [Touam 1997] but no experimental verification has yet been made to the best of our knowledge.

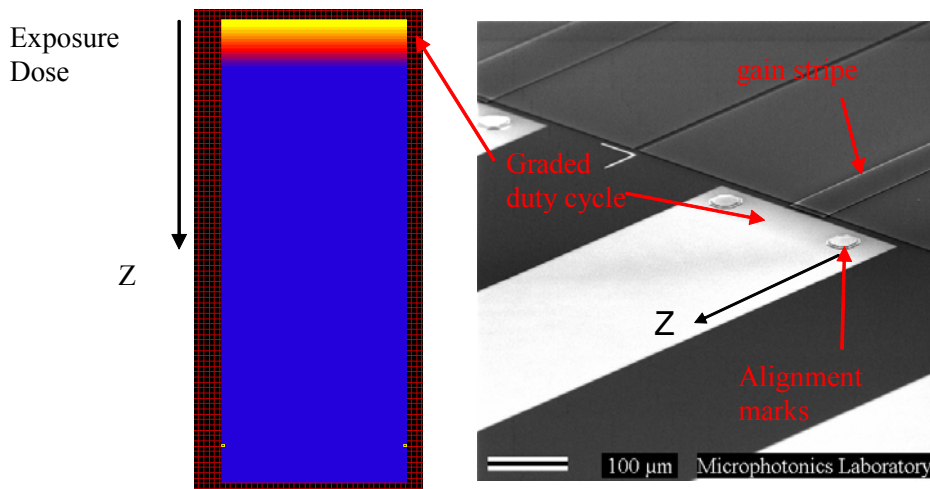


Fig.29: CAD design of a 16 level graded grating coupler and SEM of a device with a grating coupler patterned in ZEP. The exposure dose increases from  $z=0$  to  $z=80 \mu\text{m}$ .

Using e-beam lithography, the grating duty cycle variation can be achieved by varying the CAD feature size. However, since the clearing dose depends on the feature, the dose should be changed as well as shown in fig.29. Instead, it is possible to select a small CAD feature and change the dose assigned to the grating by placing each grating section in a different layer. Each layer is then assigned a different dose which is translated into a different writing frequency by the Leica EBPG. The dose increase widens the groove width proportionally to the applied dose. Another technique to control the grating duty cycle was proposed by Eriksson and uses a multiple line exposure to achieve more vertical sidewalls. However, we found that the single line exposure variation method used in this work also yields vertical sidewall profiles of the etched patterns as shown in the next section.

### **3.2.2 Pattern transfer**

After patterning, the features need to be transferred into the semiconductor material for monolithic integration. This step is achieved through plasma dry-etching to obtain anisotropic profiles of the grating coupler sidewalls for maximum coupling efficiency. We will first explain the basic principles of plasma etching by inductively-coupled plasma etcher. We will focus on the etching mechanisms of GaAs/AlGaAs by  $\text{BCl}_3$ -based chemistry to explain the process developed in collaboration with Unaxis. We will then present a comparison of hard versus soft mask pattern transfer to justify the process chosen for this work. Finally, effects specific to etching of submicron features such as microloading effect will be analyzed and applied to the

fabrication of graded grating couplers.

### *3.2.2.1 Inductively coupled plasma (ICP) etching mechanisms*

In a standard RF-generated plasma etching system, a voltage is applied between two electrodes by an RF power supply operating at 13.56 MHz to cause free electrons in the etching chamber to oscillate and collide with gas molecules. Those collisions produce ionization of the gas molecules which in turn create an avalanche of ions and electrons. This strong ionization also produces photons responsible for the well-known plasma glow. The typical parallel-plate reactor consists of a cathode capacitively coupled to the RF generator and a grounded anode. Since the reactor is equivalent to a capacitor, the cathode becomes charged by the electrons created during the ionization and retains a DC bias voltage which is used as one main characteristics of physical etching. The reactive species created in the plasma constitute the main etching mechanism since they diffuse to the sample surface and react with the solid molecules. The reaction products removal is assured by the vacuum and enhanced by various mechanisms. The advantage of the ICP source is to increase greatly the plasma density by changing the RF coupling to the plasma through a second RF generator operating at 2MHz. The ICP source consists of a helical resonator wrapped around the chamber that produces circumferential electric field lines shielded from the electrodes inside the chamber and an inductively-coupled axial RF magnetic field that creates high density plasma by changing the path of the electrons in the chamber. Indeed, instead of

going straight from the anode to the cathode, the electrons follow helical path forced by the axial magnetic field inductively created by the circumferential electric field lines. The longer path increases the ionization efficiency, creating high density plasmas. Such a source, shown in fig.29, has therefore the potential to create high-density ( $10^{12} \text{ cm}^{-3}$ ), low-energy plasmas sustainable at low pressure.

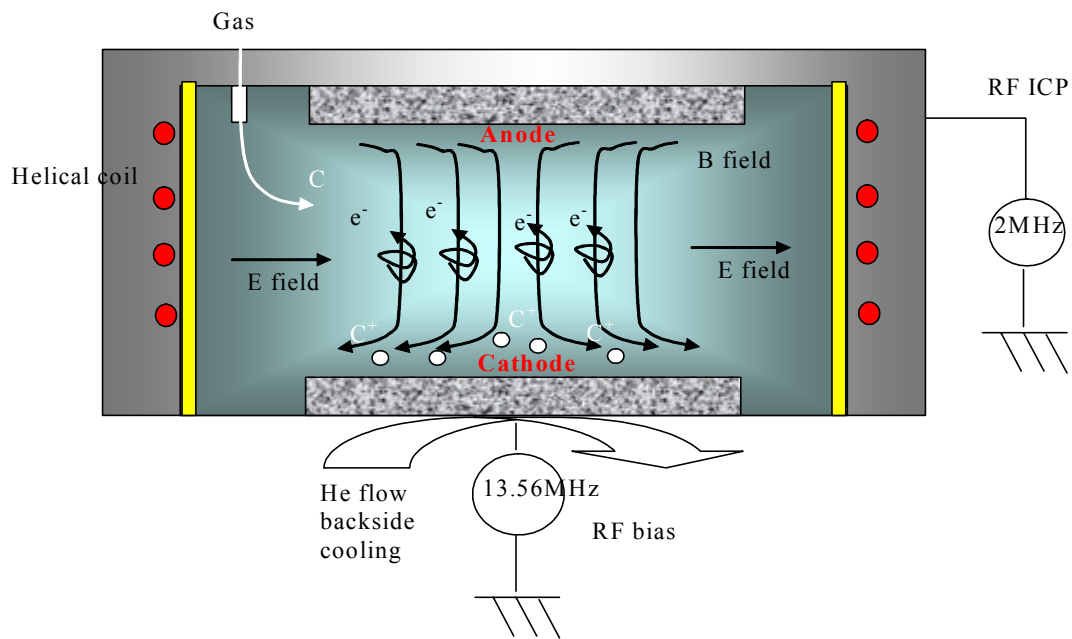


Fig.30: Diagram of an inductively-coupled plasma source (modified from Unaxis [Unaxis 2003]).

As a consequence of the decrease of electron density lost to the sample surface, a lower DC bias is typically measured with ICP sources, which also means low damage etching of the sample surface. A flow of Helium gas under the chuck with typical pressures of 50 torr allows active cooling of the sample during deep etching.

### 3.2.2.2 Etching process for GaAs/AlGaAs

The etching process to transfer the grating coupler into the AlGaAs p-cladding of the semiconductor structure was developed in collaboration with Unaxis, USA based in Saint-Petersburg, FL. The gas chemistry is based on Boron trichloride ( $\text{BCl}_3$ ) which dissociates in the plasma to produce chlorine molecules adsorbed chemically by the AlGaAs/GaAs surface. The ability of  $\text{BCl}_3$  to etch the native oxide makes it a good candidate to etch the AlGaAs layer which tends to oxidize more easily than GaAs [Cooperman 1988]. However it is more difficult to dissociate  $\text{BCl}_3$  than  $\text{Cl}_2$  and produces less reactive Cl molecules. Therefore slower etch rates are usually found with  $\text{BCl}_3$ -based chemistries but this is not an issue when etching fine features to a shallow depth like in this work.

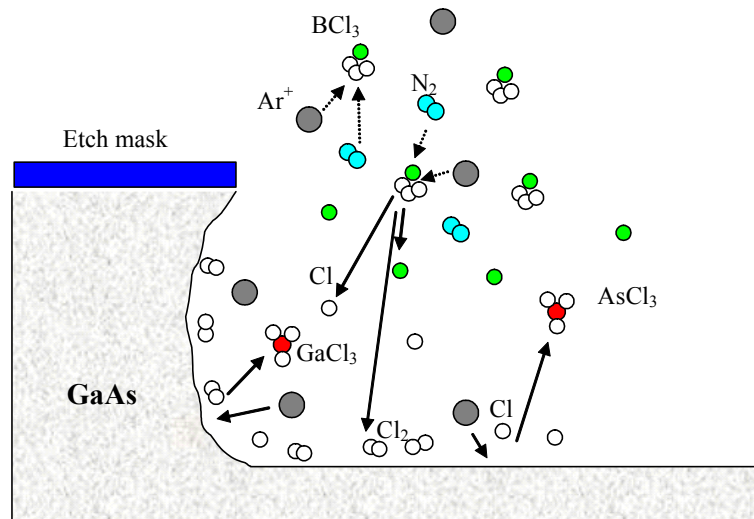


Fig.31: Etching mechanism of GaAs in  $\text{BCl}_3/\text{N}_2/\text{Ar}$  chemistry.

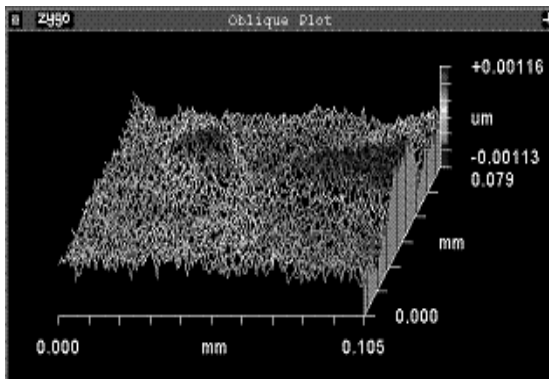
The ionization of  $\text{BCl}_3$  was found to be strongly enhanced by the presence of roughly 33% of  $\text{N}_2$  in the gas composition [Maeda 1998]. The reaction products of the Chlorine molecules with GaAs and AlGaAs are mainly Gallium and Arsenic Chloride  $\text{GaCl}_2$ ,  $\text{GaCl}_3$ , and  $\text{AsCl}_3$ . The removal process was found to be greatly improved by collisional cascade removal provided by a flux of heavy argon ions [Balooch 1986]. These processes have been investigated in details and applied successfully to chemically assisted ion beam etching (CAIBE) of GaAs [Hagberg 1994]. A diagram representing the chemical reaction occurring at the GaAs surface is shown in fig.31.

#### *3.2.2.3 Etching process characterization*

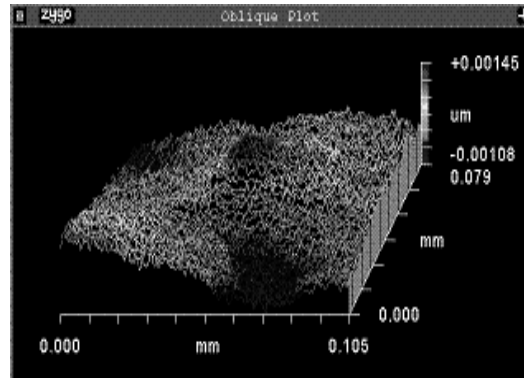
The grating coupler features require a very precise control of the etch depth and sidewall profile. In order to control the feature depth within  $\pm 20\text{nm}$ , the etch rate was decreased from the standard GaAs process by decreasing the RIE power to 60W and decreasing the pressure to 3mT. Decreasing the pressure reduces the mean path length of electrons in the chamber, decreases the ionization and therefore decreases the etch rate. It also enhances the etching anisotropy. A sample patterned by UNAXIS in photoresist on GaAs (100) is used to characterize the etching process for large features. The important etching parameters are defined in Fig.32. The sample is mounted on a 4" Silicon wafer with vacuum grease and loaded in the chamber through a load-lock system. The bottom of the etched groove was analyzed using a white light ZYGO interferometer to control the surface roughness. A root mean square (RMS) roughness of less

than 1nm was measured. Such a smooth surface is provided by the high density, low energy plasma which causes very little damage to the features.

<b>Etched Material</b>	GaAs	GaAs	AlGaAs
<b>Sample size</b>	~10mmX20mm	~10mmX20mm	~10mmX20mm
<b>Mounting</b>	4" Si	4" Si	4" Si
<b>Mask</b>	Photoresist 1.22 $\mu$ m	ZEP	ZEP
<b>Feature size</b>	>10 $\mu$ m	70nm	70nm
<b>Gas</b>	BCL3/N2/Ar	BCL3/N2/Ar	BCL3/N2/Ar
<b>Flow (sccm)</b>	20/5/10	20/5/10	20/5/10
<b>Pressure</b>	3mT	3mT	3mT
<b>ICP</b>	400W	400W	400W
<b>RIE</b>	60W	60W	60W
<b>Temperature</b>	25 C	25 C	25 C
<b>DC Bias</b>	~-172V	~-172V	~-172V
<b>Etch rate</b>	400nm/mn $\pm$ 20nm	~260nm/mn $\pm$ 20nm	~170nm/mn $\pm$ 20nm
<b>Selectivity</b>	~2.35:1	1:2 (sloped mask)	1:2.5 (sloped mask)
<b>RMS Roughness</b>	<1nm	<1nm	<1nm



RIE power =60W



RIE power =100W

Fig.32: AlGaAs/GaAs etching process parameters for anisotropic etching of submicron features. The Zygo profile of the etched GaAs surface shows a very smooth surface (RMS roughness<1nm) resulting from the high density, low-energy plasma generated by the ICP source for RIE powers of 60W to 100W.



We found the etch rate of GaAs to be 33% higher than AlGaAs for short etching time because of the higher reactivity of Al to produce oxidation, although the use of  $\text{BCl}_3$  tends to limit the difference between the two materials [Cooperman 1988]. Note that the selectivity for small features is hard to define since erodible resist masks such as e-beam resist are removed much faster on densely packed features due to the pyramidal shape produced by the mask erosion. Thus the etching selectivity not only depends on the feature width but also on the feature groove period which makes it difficult to characterize. We experimentally found that for AlGaAs, a ZEP resist mask thickness of 450nm was enough to obtain vertical sidewalls up to 270nm deep for features of 140nm. Deeper etching transfers the sloped sidewall to the semiconductor material. We will see later that we can take advantage of this feature to control the sidewall profile.

#### *3.2.2.4 Soft mask versus hard mask*

The transfer of the grating pattern into the semiconductor material requires vertical sidewalls, accurate depth control, and needs to be repeatable. The patterns were first transferred into Poly(methyl methacrylate) (PMMA) from Microchem corp. because of the resist availability and robustness. However, PMMA is well-known for its poor dry-etch resistance and showed selectivity as small as 1:1 for features as large as  $2\mu\text{m}$  during pattern transfer into GaAs. We then focused on a hard dielectric mask which requires first to etch the pattern into a thin layer of  $\text{Si}_3\text{N}_4$  using a reactive ion etcher before transferring the pattern into the semiconductor material.

Following Lenhman [Lehman 1975] and the recommendations from the team at UNAXIS, a gas mixture of CHF<sub>3</sub> and O<sub>2</sub> was used to etch the pattern into the silicon nitride film.

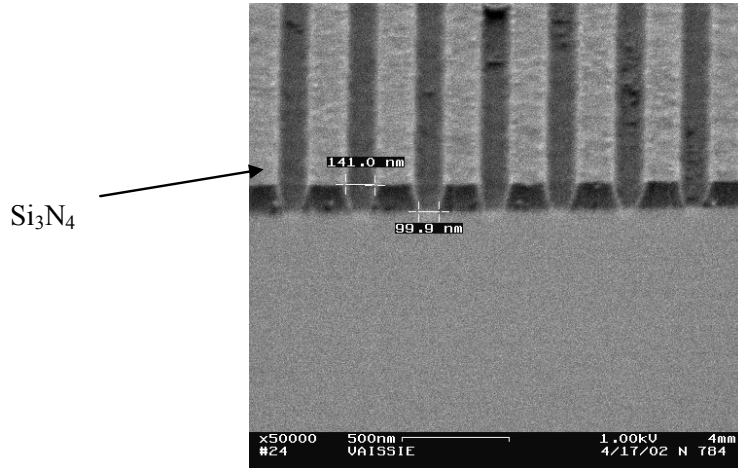
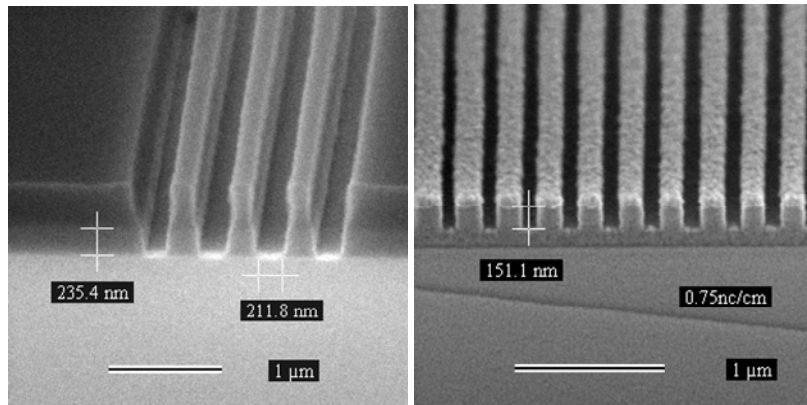


Fig.33: Typical slanted profile in Si<sub>3</sub>N<sub>4</sub> obtained from standard CF<sub>4</sub> RIE etching using PMMA mask. The mask was removed before SEM inspection.



Gas	Flow (Sccm)	Pressure	RIE power	Etch rate
CHF <sub>3</sub> /O <sub>2</sub>	11/0.8	10mT	150W	~50nm/mn

Fig.34: Etched dielectric sidewalls profile comparison between PMMA (left) and ZEP 520 (right) mask after anisotropic RIE using CHF<sub>3</sub> for passivation of the sidewalls.

Heinecke [Heinecke 1975] first noticed that the addition of hydrogen to  $\text{CF}_4$  increased selectivity of  $\text{SiO}_2$  to Si. He explained that the hydrogen scavenges fluorine to form HF, decreasing significantly the silicon etch rate compared to pure  $\text{CF}_4$  by decreasing the fluorine concentration available. Later, Oehrlein et al. [Oehrlein 1987] showed by surface analysis that the process also creates a  $\text{CF}_x$  fluorocarbon polymer film that passivates the etched sidewalls and enables very good anisotropic profiles as well as good  $\text{SiO}_2/\text{Si}$  selectivity as opposed to standard  $\text{CF}_4/\text{O}_2$  which creates slanted sidewalls by etching the material more isotropically as shown in fig.34. Also, PMMA was replaced by ZEP520 resist (ZEON corp.) which clears at a much smaller dose than PMMA and provides a threefold better etch resistance to provide vertical sidewalls as shown in Fig.34. The SiNH dielectric layer was PECVD grown at  $200^\circ\text{C}$ . It is important to note that the  $\text{CF}_x$  film created by this process prevents long and deep etching without cleaning the chamber periodically. Although the features in the dielectric layer exhibit many desirable features including vertical sidewalls and low etch rate, we faced two main problems during the pattern transfer into the semiconductor material. First, the polymer created by  $\text{CHF}_3$  greatly decreased the repeatability of the process by creating nonuniformities during the pattern transfer into AlGaAs. Secondly, the hard dielectric mask offers a very good etch resistance and selectivity to AlGaAs ( $>7:1$  for  $\text{Si}_3\text{N}_4$  grown at  $250^\circ\text{C}$ ) which in turn created an effect known as bowing effect in the semiconductor material as shown in Fig.35. On the other hand, transferring the pattern using single step lithography eliminates both problems. For this purpose, ZEP 520 resist can be spun at a thickness of 450nm to obtain vertical sidewalls as shown in Fig.35. This erosion mechanism is well-known and is described for example in [Hagberg 1994].

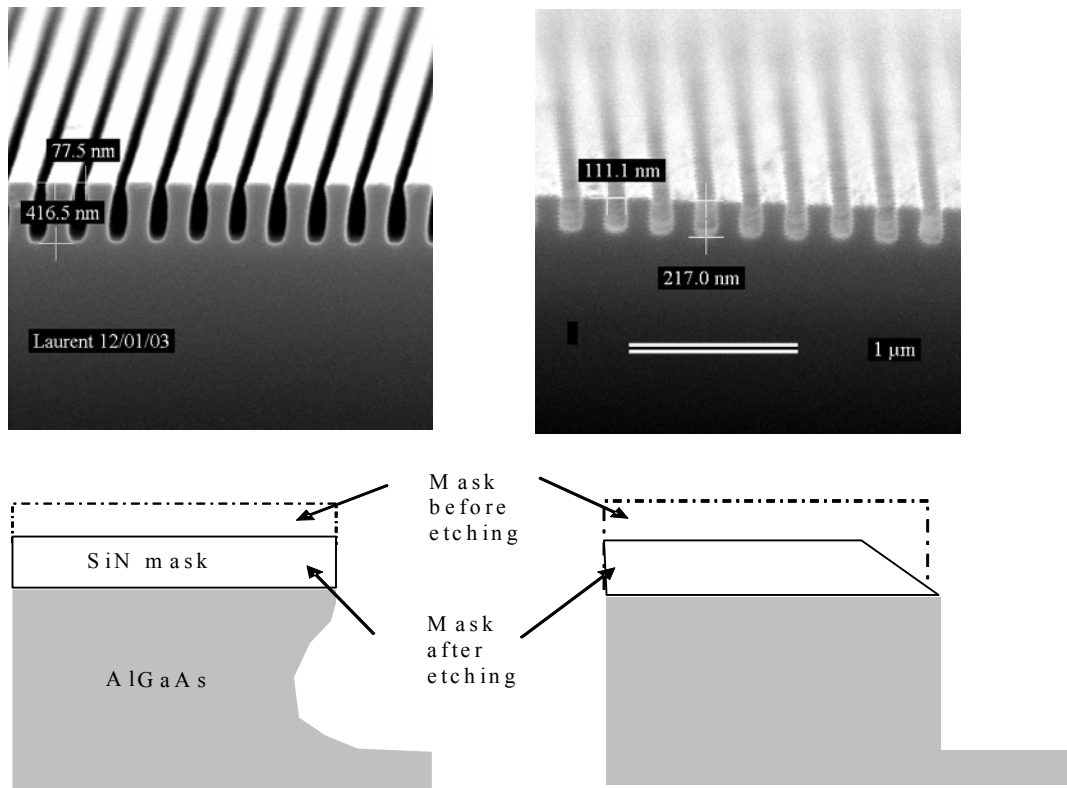


Fig.35: SEM of sidewalls profiles obtained using hard (left) and soft mask (right). The erosion of the soft resist mask compensates for the bowing effect. The drawing is modified from [Hagberg 1994].

### 3.2.2.5 Aspect ratio dependent etching (ARDE)

The grating features are typically ranging from 25nm to 140nm wide, corresponding to a duty cycle of roughly 10% to 50% for a 270nm period. This duty cycle variation controls the near-

field intensity profile of the outcoupled beam, compensating for the standard exponential decay due to coupling of the guided wave to a leaky wave by the grating coupler. However, the transfer of these features into the III-V material shows a strong dependence of the feature depth versus width during the same etching process. This effect, known as RIE lag or aspect ratio dependent etch (ARDE), has been consistently observed for sub-micron features etched in plasma chemistries. Gottscho et al. explained this phenomenon by the transport limitation of etching species due to diffusion processes on the wafer and ion shadowing due to high aspect ratio features. These explanations are consistent with the observation that this effect is time dependent since the aspect ratio increases with time [Gottscho 1992]. We characterized the microloading effect for features ranging from 27nm to 160nm patterned in ZEP resist and etched for 60s in AlGaAs using the process described in paragraph 3.2.2.3. We observed a linear dependence of the feature width versus depth, which confirms that the features' aspect ratio is typically conserved during the first couple of minutes of etching as shown in Fig.36. This linear equation will be used to model accurately the near-field profile obtained from a graded strength grating coupler as demonstrated later in chapter IV. Another phenomenon occurring during transfer of densely packed lines is called the microloading effect attributed to the depletion of the reactant concentration due to excessive substrate load [Hedlund 1994]. This effect, unlike ARDE, depends only on the features density and translates into a decrease of the etching rate of a grating compared to an isolated line for example. It should therefore be noted that all the data considered in this work were characterized using at least a few lines to minimize the proximity effect for patterning as well as the microloading effect for pattern transfer.

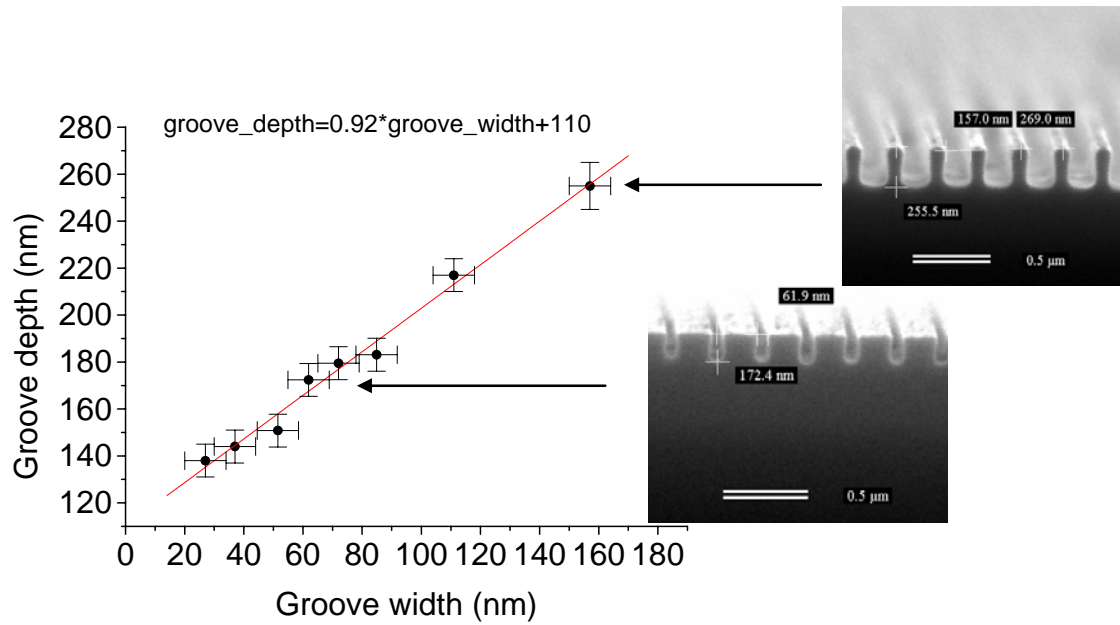


Fig.36: Characterization of aspect ratio dependent etching in AlGaAs using ZEP resist as a mask (removed before SEM).

### 3.2.2.6 Grating metallization and substrate antireflection coating

For high power operation, it is important to keep the active region close to the heat sink to provide better cooling and avoid thermal rollover. It is therefore required to mount the device p-side down on the heatsink. In this configuration, light must be extracted through the substrate and windows must be opened on the n-side contact by lift-off as described earlier. However, since light is diffracted on both sides of the grating, it is necessary to redirect the light emitted in

the air towards the substrate. To do so, based on the analysis shown in chapter 2, we followed Evans et al. who first proposed to cover the grating with quarter wave dielectric layer followed by a 200nm gold layer as shown in Fig.37. A 63% increase of the device external differential quantum efficiency was reported using this technique [Evans 1989].

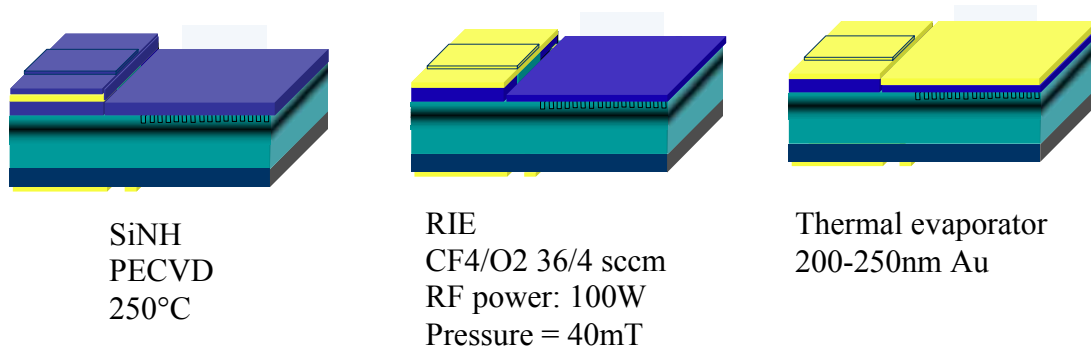


Fig.37: Grating coupler metallization scheme.

The dependence of the layer's index of refraction upon the gas composition was analyzed using a reflectometer. An uncoated GaAs sample was placed as a reference before samples obtained from 4, 6, and 8sccm of ammonium ( $\text{NH}_3$ ) flow, the other parameters remaining the same. The results are shown in Fig.38. At a wavelength of 980nm, the higher  $\text{NH}_3$  gas flow gives an index of refraction close to 1.79. The reflection coefficient for the multilayer semiconductor structure with a dielectric film coated on the substrate was derived using equations (2.40) and (2.41). Considering that light is diffracted by a 270nm period grating, a minimum reflectivity of  $6 \cdot 10^{-3}$  is obtained for TE polarization for a dielectric film of index 1.78 and a thickness of 142nm.

Consequently all the antireflection dielectric layers we used in this work were deposited using the highest  $\text{NH}_3$  flow of 8sccm and the following parameters shown in table 8.

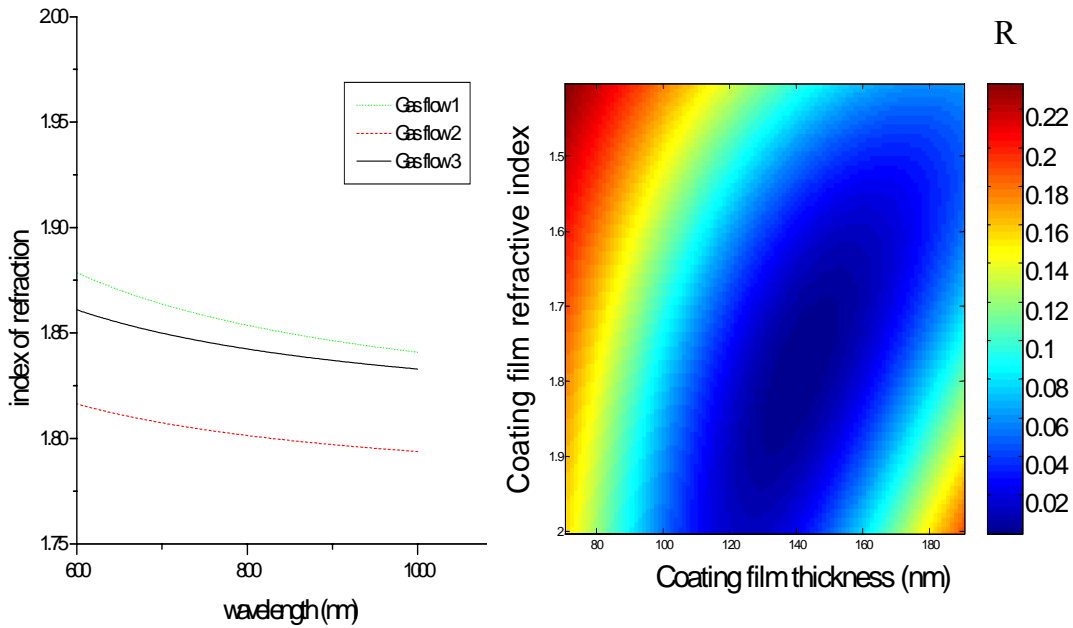


Fig.38: Index of refraction of PECVD grown films versus  $\text{NH}_3$  gas flow. Gas flow 1=4sccm, gas flow 2= 6sccm, gas flow 3=8sccm. The lowest reflectivity is obtained for a film of index close to 1.78 which corresponds to 8sccm  $\text{NH}_3$  gas flow.

Table 8: Process parameters used to deposit  $\text{SiNH}$  in PECVD chamber provided by Unaxis Inc..

$\text{NH}_3$	$\text{SH}_4$	$\text{N}_2$	Pressure	RIE	Temperature
8sccm	250sccm	650sccm	40mT	25W	250°C

Using a Quintel contact aligner, the dielectric layer was removed from the p-contact by RIE in



CF<sub>4</sub>/O<sub>2</sub> chemistry at a rate of 100nm/min. A 1μm thick layer of NR7-1000PY was used as a mask. After cleaning the sample, the devices were then placed inside the chamber of an Edwards thermal evaporator where a 5nm of Chromium was deposited for adhesion purposes, followed by a 250nm thick layer of Gold to act as a reflector. An SEM picture shows the cleaved profile of the grating coupler after metallization. The nonconformal coating of the grooves by the dielectric layer can be seen on the SEM picture and is known as “breadloaf effect”.

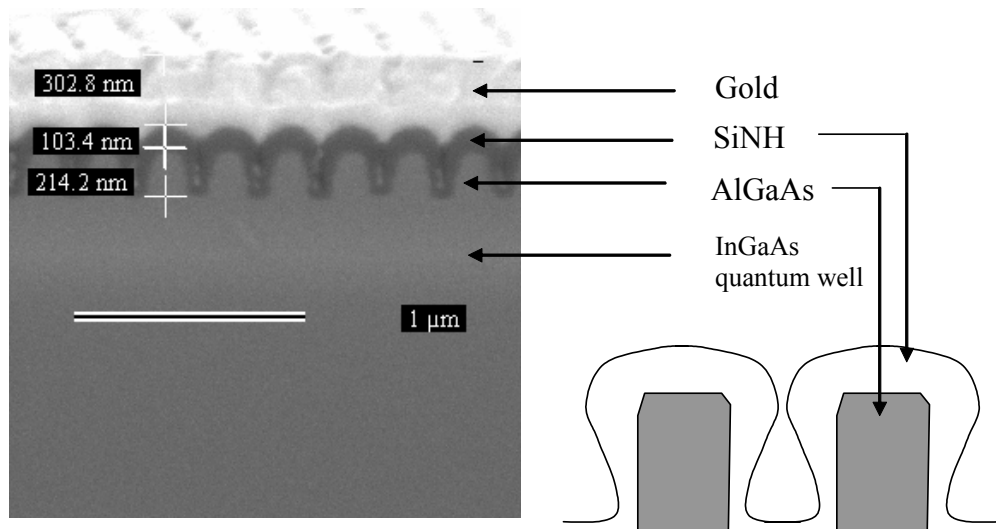


Fig.39: SEM of typical grating profile with high reflection coating. The nonconformal coating of the dielectric layer produces a “keyhole” feature in the profile which may cause some additional scattering losses.

This effect represents the nonuniform coating of the SiNH layer which is thinner on the side due to a shadowing effect during plasma deposition caused by the feature aspect ratio. This keyhole feature inside the dielectric layer may be overcome by a multiple steps of deposition followed by Argon ion sputtering to obtain a conformal coating [Kotani 1985]. However, for our application,

it seems the ideal case would be to fill the semiconductor gap with dielectric material and then planarize the coating layer before metallization. In this case, the metal layer acts only as a reflector and does not interfere with the diffraction by the grating coupler. A review of the limitations of chemical vapor deposition of dielectric films applied to gap-filling of small features can be found in [Cote 1995]. A low reflection coating can then be integrated on the substrate by repeating steps 1 and 2 shown in Fig.39. Other optical elements can also be integrated at this point on the device substrate as we will see in chapter 5.

### **3.3 Conclusion**

We detailed the fabrication steps used to create an efficient grating-coupled semiconductor laser. The wide variety of features needed on the device requires the understanding of a broad range of complex equipment processes, ranging from patterning and deposition to etching and metallization. The process characterization helped to understand the etching mechanisms in GaAs-based materials. We developed a repeatable process that meets the stringent requirements on the grating coupler features such as duty cycle, depth and sidewalls profiles. We will now present the performance results of the devices fabricated using this process. We will show how the characterization of the fabrication process for small features can improve the device performance by correcting the near field intensity profile. We will also detail the losses mechanisms involved in the device performance to evaluate the grating efficiency and identify the areas of potential further improvement.

## **CHAPTER 4: PERFORMANCE ANALYSIS**

We described in chapter 4 the different steps involved in the fabrication of the GCSEL devices before integration of the backside optical elements. The fabrication process was optimized to obtain high efficiency and high power surface-emitting devices with improved near-field spatial beam profiles. The output from such device can then be properly shaped or the efficiency improved by integrating monolithic optical elements on the substrate as described in chapter 5. In this chapter, we present the performance characteristics of the GCSEL device before integration of the second optical element. The quality of the fabrication process is evaluated by estimating the grating efficiency using an analysis of the various losses mechanisms involved in limiting the device performance. Also, the impact of replacing a standard cleaved facet mirror by a low reflectivity detuned grating coupler on the cavity resonator will be highlighted in the case of the GCSEL device. Then, the effect of replacing both cleaved facets by detuned second order gratings will be investigated. All the raw data presented to support the performance analysis in this section was collected by Dr Oleg Smolski, research scientist of the Microphotonics laboratory.

### **4.1 Testing set-up**

After fabrication, the samples are cleaved with a Dynatec automated cleaver. Some chips are

tested directly without bonding on a gold-covered plate using a needle probe for measurement of the light versus current characteristic in pulse regime using a PCX-7410 driver from Directed Energy. The chip testing is also used to measure the power extracted from the grating side and substrate side, before AR/HR coatings are integrated, to calculate the grating efficiency as will be shown in section 4.4.2. For the other testing procedures of the completed device, including far-field measurements, voltage characteristic and spectrum measurements, the devices are bonded p-side down on a Beryllium Oxide (BeO) substrate applying Indium (In) solder performs. Wire bonding is performed on the n-contact to provide uniform current distribution along the broad area laser stripe. The device temperature is controlled through a thermoelectric cooler mounted on a copper heatsink. The copper block is cooled by a water flow maintained at 20°C. Optical powers in CW and high power QCW regime are measured with a thermal head from Ophir. Spectrum measurements are generally performed by coupling light into a multimode fiber close to the device to capture the entire spectrum despite the spatial dispersion produced by the grating coupler.

## **4.2 Low reflectivity GCSEL performance**

### **4.2.1 L-I-V characteristics**

The power versus current characteristic curve is obtained by measuring the power from the low

divergence output coming out of the device substrate impinging directly on an Ophir photodiode or thermal head. The laser is bonded p-side down. The voltage versus current characteristic is also controlled using continuous wave pumping of the diode. The grating duty cycle is tapered on a distance of  $80\mu\text{m}$  from about 15% to 40%. A grating depth of 210nm for the largest duty cycle was measured by SEM. The substrate is coated with a low reflection dielectric coating. The low grating reflectivity results in a large ratio between powers measured at the grating side and the facet which reduces the risk of COD. The device is pumped in quasi-CW conditions with a pulse width of 500ns at a repetition rate of 1kHz. The measured slope efficiencies for 7 devices with 2mm long stripes vary from  $0.62\text{W/A}$  to  $0.71\text{W/A}$ . Devices with 1mm long active region showed slope efficiencies around  $0.58\text{W/A}$ .

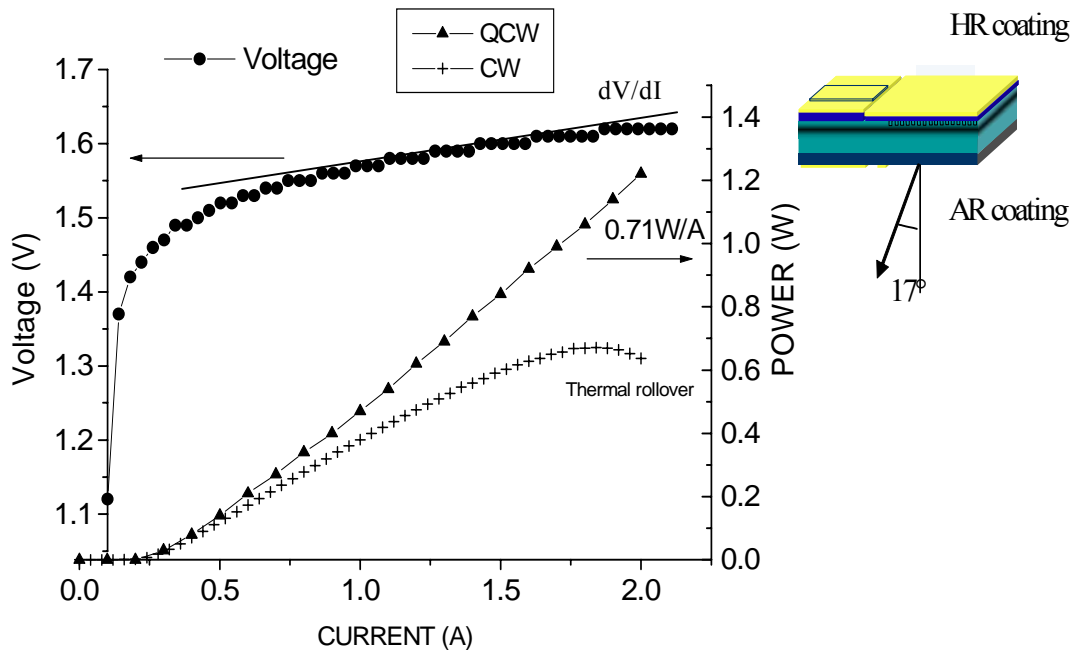


Fig.40: Typical L-I-V curve for a 2mm long,  $60\mu\text{m}$  wide stripe GCSEL with AR dielectric coating on the substrate.

Although the differential quantum efficiency is typically inversely proportional to the stripe length for Fabry-Perot lasers, the GCSEL's behavior resembles more a single pass gain element such as a superluminescent diode where the power increases as a function of the device length due to increased gain. Optimum device length was found to be around 2mm. For longer lengths, the intra-cavity losses become significant and the device efficiency decreases. The performance was similar for 100 $\mu$ m and 60 $\mu$ m wide stripe devices although 100 $\mu$ m stripe devices show a better thermal behavior due to a wider area and lower resistance. When the device is pumped in continuous wave operation, thermal effects decrease the efficiency of the device significantly above 1A pumping current. However, the ability to bond the device p-side down still improves the performance significantly. The device resistance can be derived from the slope of the voltage versus current curve and shows a typical resistance of  $2.5 \times 10^{-4} \Omega \cdot \text{cm}^2$ .

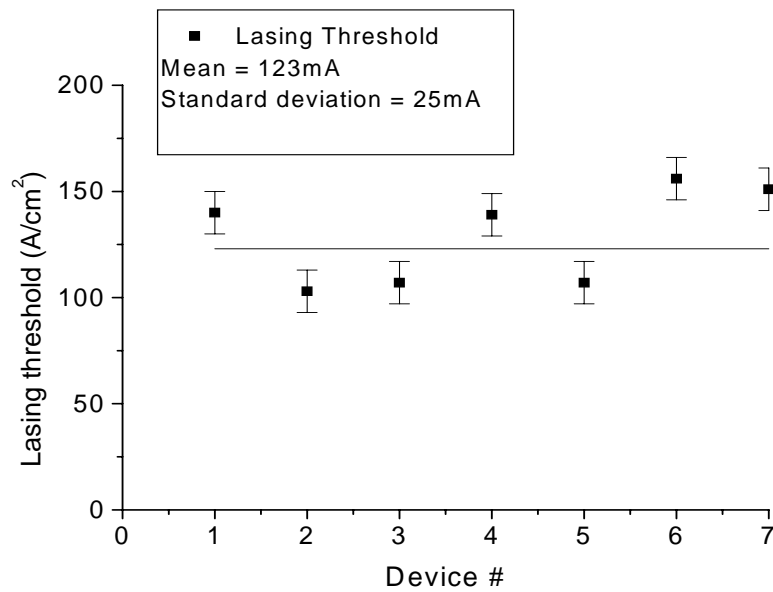


Fig.41: Lasing threshold current densities for 2mm long GCSEls with HR/AR coatings on grating and substrate respectively. The cleaved facet is left uncoated.

Due to the high mirror losses  $\alpha_m$ , defined by equation (1.9), introduced by the low reflectivity mirror and, higher current is required to overcome the cavity losses which results in a higher lasing threshold than Fabry-Perot lasers. The typical lasing threshold for GCSELS is 123A/cm<sup>2</sup> as shown in fig.41. For comparison, 2mm long uncoated facets Fabry-Perot lasers show a lasing threshold around 70A/cm<sup>2</sup>. Although the lasing threshold is defined here classically as the intersection of the L-I curve with the current axis X, the very low mirror reflectivity actually affects the device lasing behavior and the actual current at which lasing can be properly defined. The L-I curve around threshold shows a gentle knee, typical of superluminescent diode behavior, the emission being dominated by amplified spontaneous emission due to the lack of feedback from one of the resonator's mirrors.

#### **4.2.2 Analysis of grating performance**

A discussion of the performance of the fabricated device involves a detailed analysis of the losses mechanisms involved in the light extraction. We will show that losses are mainly due to the substrate absorption, the substrate reflectivity, the grating scattering losses, and the absorption in the unpumped waveguide. We will then use these parameters to evaluate the grating efficiency and reflectivity.

#### 4.2.2.1 Substrate losses

In the proposed device configuration, light is extracted through the GaAs substrate. Although the emission wavelength is far away from the absorption peak of the material (located at 808nm), the heavy n-doping of the substrate creates a doping-dependent free carrier absorption that limits the overall efficiency of the device [Spitzer 1959]. We estimated these losses experimentally by measuring light transmitted from a GCSEL around 974nm through samples of four different thicknesses.

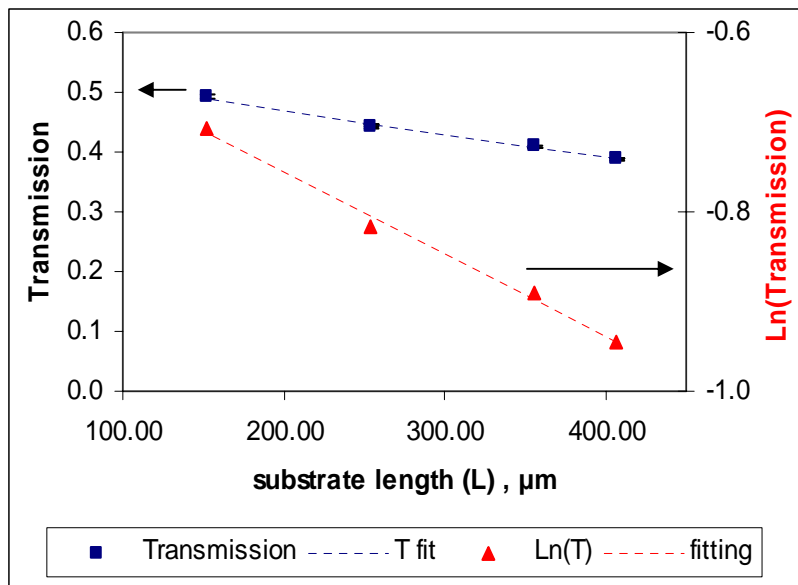


Fig.42: Linear fitting of transmission through n-doped GaAs substrate.

The sample was lapped and polished after each experiment to achieve the desired thickness.



Assuming a sample of thickness  $L$  at normal incidence, the power transmitted through the substrate is given, assuming multiple reflections can be neglected, by

$$T = \frac{P_{out}}{P_{in}} = (1 - R)^2 \cdot \exp(-\alpha_{sub} L) \quad (4.1)$$

where  $R$  is the power reflectivity and  $\alpha_{sub}$  is the absorption coefficient. The need for accurate reflectivity measurements is alleviated by measuring samples with different thicknesses. The absorption coefficient is obtained directly from a linear fitting of the logarithmic curve of the transmission as shown in Fig.42. The absorption coefficient is estimated at  $9\text{cm}^{-1}$ , corresponding to losses as high as 12% for single pass propagation in a  $140\mu\text{m}$  thick substrate, typical of the substrates used for this work. The substrate losses must be taken into account to evaluate the overall grating efficiency.

#### *4.2.2.2 Passive region losses*

Another source of concern regarding the ultimate performance of the GCSEL device has been the absorption caused by the unpumped quantum well. Since light has to propagate into the passive region to interact with the grating, one has to wonder whether the device efficiency will be severely affected. From the rather high experimental slope efficiencies measured in Fig.40, it is clear that the absorption is not quite as high as the predicted  $2.10^3\text{cm}^{-1}$  absorption coefficient for InGaAs quantum well [Coldren 1995 p.167]. To investigate this further, we first measured

slope efficiencies of devices cleaved with 0.5mm and 1mm passive region without grating integrated. In this case, we are in the familiar case treated by Coldren of a device with an active region of length  $L_a$ , and a passive region of length  $L_p$  as shown in Fig.41. The intracavity absorption coefficient was derived in Chapter 2 from Fabry-Perot measurements and equals  $2.5\text{cm}^{-1}$ . All the other parameters being known, we can derive the passive region absorption loss. The facets are left uncoated and their reflectivity therefore equals 0.32. From the results of the FDTD modeling presented in chapter 2, the reflectivity between the active and passive region can be neglected. By setting the energy generation rate equal to energy loss rate for the above cavity configuration, it can be shown [Coldren 1995, Appendix no 5, p.456] that the mirror losses associated with the cavity configuration are given by

$$\alpha_m = \frac{P_1 + P_3}{P_1 + P_2} \frac{\Gamma_z}{L_a} \ln \left( \sqrt{\frac{1}{R_1 R_2}} \right) \quad (4.2)$$

$\Gamma_z$  is the axial confinement factor defined by the fraction of the energy confined to the active region. It is important to note that this expression is significantly different from the equation representing mirror losses in the case of a simple active region configuration as derived in chapter 1. Using the definition of the external differential quantum efficiency (1.7), one gets

$$\eta_d = \eta_i \frac{\alpha_m}{g_{th}} \quad (4.3)$$

where  $g_{th}$  describes the total modal gain at threshold. It can also be expressed as a function of the transverse modal gain  $g_{xy}$  to reduce (4.3) to

$$\eta_a = \eta_i \frac{\ln\left(\sqrt{\frac{1}{R_1 R_2}}\right) \frac{P_1 + P_3}{P_1 + P_2}}{g_{xy} L_a} \quad (4.4)$$

Using the threshold condition applied to the active region only, one gets

$$g_{xy} L_a = \alpha_a L_a + \ln\left(\frac{1}{\sqrt{R_1 R_2}}\right) \quad (4.5)$$

The power  $P_i$  can be calculated accurately by expressing the expressions of the power circulating inside the cavity.

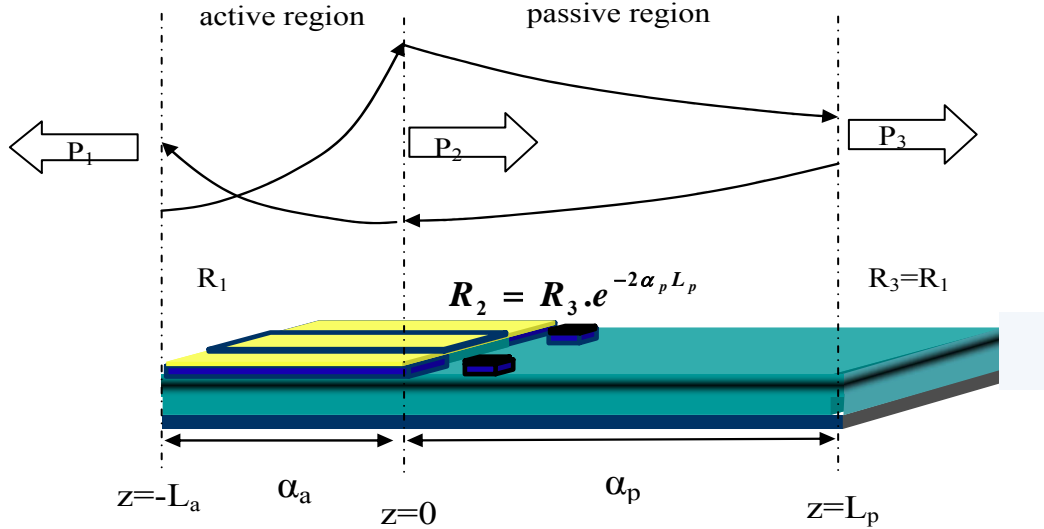


Fig.43: Device configuration for characterization of passive losses. The exponential gain and losses are taken into account for the derivation of the external differential efficiency. The effective reflectivity between active and passive region is neglected.

In the active region, the power curve for the forward and backward propagating waves are given by

$$\begin{cases} P_a^+(z) = \frac{1}{\sqrt{R_2}} \exp((g_{xy} - \alpha_a)z) \\ P_a^-(z) = \sqrt{R_2} \exp(-(g_{xy} - \alpha_a)z) \end{cases} \quad (4.6)$$

Inside the passive region we get

$$\begin{cases} P_p^+(z) = \frac{1}{\sqrt{R_2}} \exp(-\alpha_p z) \\ P_p^-(z) = \sqrt{R_2} \exp(\alpha_p z) \end{cases} \quad (4.7)$$

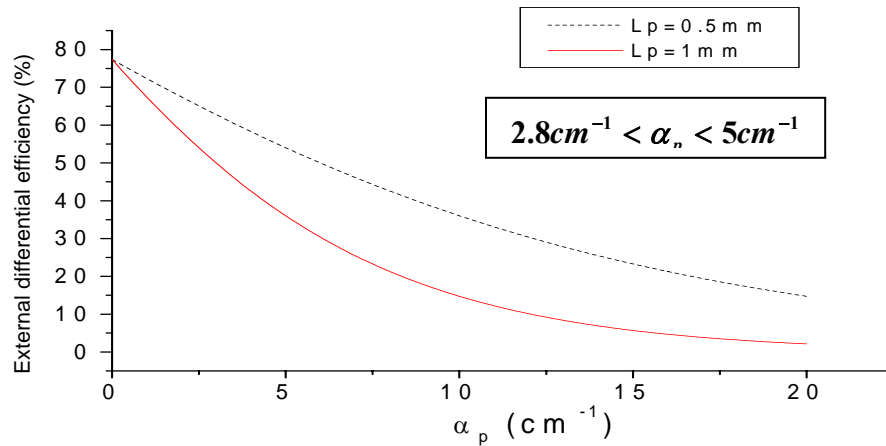
where the decay coefficient  $\alpha_p$  can be expressed as a function of  $R_2$  and  $R_3$  using the expression of  $R_2$  shown in Fig.43. The power ratio in (4.4) can then be rewritten

$$\frac{P_1 + P_3}{P_1 + P_2} = \frac{[P_a^-(z = -L_a) - P_a^+(z = -L_a)] + [P_p^+(z = -L_p) - P_p^-(z = L_p)]}{[P_a^-(z = -L_a) - P_a^+(z = -L_a)] + [P_p^+(z = 0) - P_p^-(z = 0)]} \quad (4.8)$$

The external differential efficiency can then be readily compared to data measured from cleaved devices and the passive loss coefficient can then be derived. In our case,  $R_1 = R_3 = R = 0.32$ , then (4.3) reduces to

$$\eta_d = \eta_i \cdot \frac{1}{1 - \frac{\alpha_a L_a}{\ln(\text{Re}^{-\alpha_p L_p})}} \cdot \frac{2}{1 + \frac{(1 - \text{Re}^{-2\alpha_p L_p})}{(1 - R) \cdot e^{-\alpha_p L_p}}} \quad (4.9)$$

Four samples were used experimentally to determine the passive region losses by comparing the experimental results to the theoretical curves shown below in Fig.44. The loss coefficient is estimated to be between 2.8 and 5 cm<sup>-1</sup>. These numbers are fairly close to the losses parameters measured in the active region. A possible explanation of the relatively small impact of the large quantum well absorption coefficient on the external differential efficiency can be the red-shift of the lasing wavelength observed experimentally (~4nm for 1mm passive region length).



Device#	FP (av. data)	FP#1-1-1	FP#1-1-2	FP#1-1-3	FP#1-0.5-1
La, mm	1.0	1.0	1.0	1.0	1.0
Lp, mm	0.0	1.0	1.0	1.0	0.5
total slope eff, W/A	0.96	0.70	0.67	0.65	0.70
wavelength, nm	977.0	981.4	981.0	981.2	978.0
threshold current, mA	88	168	162	172	130
total dif eff	77.3%	55.6%	52.9%	51.3%	54.8%
Average Eff.:				53.3%	54.8%

Fig.44: Theoretical (plot) and experimental (table) external differential efficiency as a function of passive region loss coefficient  $\alpha_p$ . The loss coefficient is estimated to be between 2.8 and 5 cm<sup>-1</sup>.

By shifting the lasing wavelength outside the band-gap region, the absorption is greatly reduced. The smaller shift observed for shorter passive region ( $\sim 1\text{nm}$  for  $0.5\text{mm}$  passive length) can also explain why a larger loss coefficient is observed in that case. In the case of a GCSEL, light is usually coupled out of the cavity before reaching the facet and therefore the spectrum of a GCSEL does not typically show the red-shift observed for  $L_p=1\text{mm}$ . As a consequence, it is reasonable to model the passive region losses coefficient for the GCSEL by a value close to the one obtained for the shorter passive region length. A more careful look at the near-field profile as a function of pumping current reveals that the absorption in the passive region is power-dependent due to the “bleaching” of the carriers involved in the absorption process at high power levels. In order to quantify experimentally this phenomenon, a GCSEL with a grating depth of  $200\text{nm}$  and uniform duty cycle around  $40\%$  was fabricated. The slanted sidewalls of the grating were profiled by SEM and the corresponding outcoupling length was calculated by finite-difference time domain to be around  $500\text{microns}$ . In order to take the passive region losses into account, equation (2.44) that describes the intensity profile decay becomes

$$I(z) = I_0 e^{-\frac{z}{L_{out}}} = I_0 e^{-(2\alpha_{grating} + \alpha_p + \alpha_s)z} \quad (4.10)$$

where  $\alpha_{grating}$  is defined by (2.47) and  $\alpha_s$  is the saturable absorber parameter. The near-field intensity profile measured at two different current levels is shown in Fig.45. The exponential decay measured from near-field data is used to obtain the parameter describing the saturable absorption of the quantum well by the following empirical formula:

$$\alpha_s = \alpha_s^0 \exp\left(-\frac{P}{P_s}\right) \quad (4.11)$$

where  $P_s$  describes the saturation power and  $\alpha_s^0$  the quantum well absorption coefficient when no light is propagating in the passive waveguide. This effect may be important for long outcoupling lengths and low power levels but its impact is reduced for strong grating coupling and moderate to high power levels due to high peak intensity and fast saturation of the quantum well when the passive region loss coefficient is negligible with respect to the grating's decay coefficient.

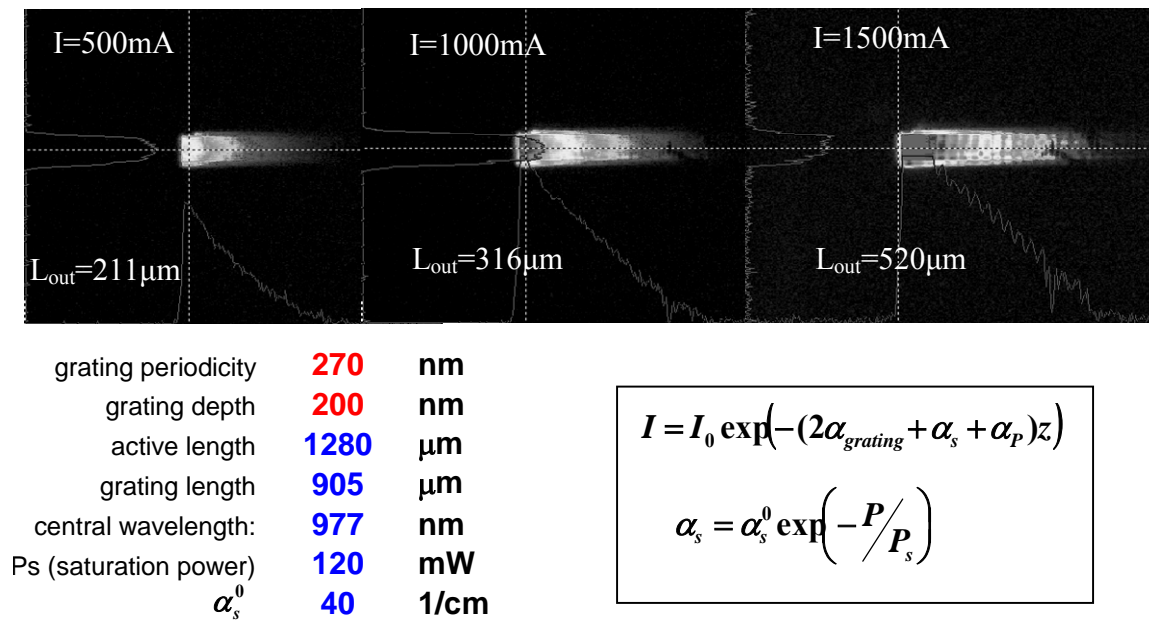


Fig.45: Near-field intensity profiles at different current levels highlighting the saturable absorption of the quantum well. Weak coupling was obtained with a 200nm deep grating with low duty cycle to investigate the passive region losses at low power levels more accurately.

Consequently, we will from now on approximate the passive region losses by the parameter  $\alpha_p$  to evaluate the grating efficiency since we consider gratings producing decay coefficients of 100  $\text{cm}^{-1}$ .

#### 4.2.2.3 Grating efficiency

In order to evaluate the impact of the several fabrication steps detailed in chapter 3, the device's optical performance was also measured after the grating integration, before the high and low reflection coatings be deposited on the grating and substrate. At this point of the process, light is diffracted into the air (1) and the substrate (2) as shown in and the grating efficiency can be derived with fewer unknown variables. Residual light is transmitted through the cleaved facets of the device (3) and (4). The total output power from the grating can then be written as

$$P_d = P^{(1)} + P^{(2)} \quad (4.12)$$

We call  $x$  the directionality of the grating in the air. We take into account multiple reflections from the superstrate but neglect the grating coupler effect on the superstrate reflectivity. The total output power from the device is then given by

$$\frac{P_d}{P_{FP}} = \eta_g \cdot \eta_l^p \cdot \left( x + (1-x) \cdot \eta_l^s \cdot (1-R_s) \cdot \left( 1 + \eta_l^s \cdot R_s + \eta_l^{s^2} \cdot R_s^2 + \dots \right) \right) \quad (4.13)$$

where  $\eta_g$  is the grating efficiency and  $\eta_l^{p,s}$  represents the losses of the passive region and



substrate,  $R_s$  is the substrate reflectivity.  $P_{FP}$  represents the maximum output power extracted from both facets of an equivalent Fabry-Perot laser and is taken equal to 1.1W/A, or 87% external differential efficiency. This value was calculated from the measured internal efficiency of Fabry-Perot lasers, intracavity losses and mirror effective reflectivities. Given the material losses and the measured power diffracted in the air and in the substrate, one can derive  $x$  by

$$x = \frac{\eta_l^s \cdot (1 - R_s) \cdot \left( \frac{P^{(1)}}{P^{(2)}} \cdot \sum_{k=0}^{\infty} (\eta_l^s \cdot R_s)^{2k} - \sum_{k=0}^{\infty} (\eta_l^s \cdot R_s)^{2k+1} \right)}{1 + \eta_l^s \cdot (1 - R_s) \cdot \left( \frac{P^{(1)}}{P^{(2)}} \cdot \sum_{k=0}^{\infty} (\eta_l^s \cdot R_s)^{2k} - \sum_{k=0}^{\infty} (\eta_l^s \cdot R_s)^{2k+1} \right)} \quad (4.14)$$

The grating efficiency can then be estimated as a function of the losses in the passive region and the substrate. The losses due to the passive region absorption can be approximated by

$$\eta_l^p = e^{-\alpha_p L_{out}} \quad (4.1)$$

while the losses in the substrate for single-pass propagation are given by

$$\eta_l^s = e^{-\alpha_s d} \quad (4.2)$$

where  $d$  is the substrate thickness equal to 140 $\mu$ m and  $\alpha_s$  is 9 cm<sup>-1</sup> so  $\eta_l^s = \mathbf{0.88}$ . An energy balance calculation shows that the light diffracted by the grating can be summed to a total of 0.93W/A or an external differential efficiency of 75%. The grating has a 55% duty cycle, 275nm depth corresponding to a decay coefficient around 100 cm<sup>-1</sup>.

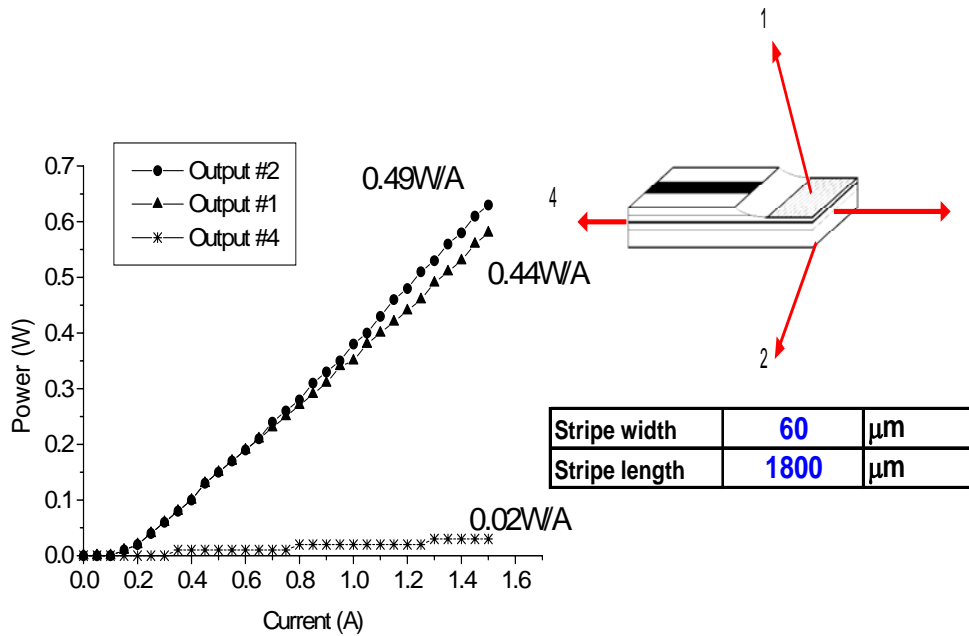


Fig.46: Typical optical power measured from the various device outputs before integration of the grating and substrate coatings. The power measured at output #3 is negligible. The grating duty cycle varies from 20% to 55% on 80μm for a maximum depth of 275nm.

This value is valid for gratings with uniform duty cycle. However, for gratings where duty cycle is varied on a distance of 80μm, the effective interaction length used to evaluate the passive region losses is increased roughly by a factor of 2 to include both rising and decaying fields. The passive region loss  $\alpha_p$  is taken to be 4 cm<sup>-1</sup> and the outcoupling length is measured around 50μm for a grating with uniform duty cycle. One can then derive the grating efficiency from (4.13). The results are shown in table 9 for three different gratings.

Table 9: Grating efficiency versus fabrication methods and grating parameters. The grating efficiency is estimated using an analysis of the losses mechanisms.

<i>Patterning tool/resist</i>	<b>NPGS/ZEP</b>	<b>EBPG/ZEP</b>	<b>EBPG/ZEP</b>
<i>Etching mask</i>	SiNH	ZEP	ZEP
<i>Grating duty cycle</i>	30%	55%	20-55%
<i>Grating depth</i>	220nm	275nm	210-275nm
<i>Grating decay <math>\alpha_{grating}</math></i>	60cm <sup>-1</sup>	100cm <sup>-1</sup>	~0-100cm <sup>-1</sup>
<i>Grating Output Power (<math>P^{(1)}+P^{(2)}</math>) (W/A)</i>	0.27+0.29	0.5+0.39	0.44+0.49
<b>Grating Efficiency</b>	<b>60%</b>	<b>92%</b>	<b>99.7%</b>

Only the best measurements out of several devices are represented. A 50% efficiency improvement was therefore obtained by optimizing the patterning and etching methods to produce more uniform gratings and decrease the scattering losses. This may explain the drop in efficiency observed by some research groups when the grating coupler is multiplexed with beam shaping elements. Such a combination harms the grating uniformity and increases feedback inside the cavity, which in turn affects the device efficiency [Modh 2002]. An additional improvement is obtained by varying the duty cycle linearly to decrease the impedance mismatch between the active and passive region.

#### 4.2.2.4 Estimation of grating effective reflectivity

The grating effective reflectivity can be experimentally estimated from measurements of the output power. The power  $P_g$  at the entrance of the passive region can be derived from (4.13) if we assume that the end facet of the laser resonator is located at the beginning of the grating and is therefore taken to be 1.06W for 1A of pumping current. The grating reflectivity is so small that the effect of its variations on the theoretical power  $P_g$  is small and is neglected in our analysis.

The grating effective reflectivity can then be calculated using [Coldren 1995, p. 78]

$$\frac{P_g}{P^{(4)}} = \left( \frac{R^{(4)}}{R_g} \right)^{1/2} \cdot \left( \frac{1 - R_g}{1 - R^{(4)}} \right) \quad (4.17)$$

which can be rewritten

$$R_g = \left[ \sqrt{1 + \left( \frac{P_g}{P^{(4)}} \cdot \frac{1 - R^{(4)}}{2\sqrt{R^{(4)}}} \right)^2} - \left( \frac{P_g}{P^{(4)}} \cdot \frac{1 - R^{(4)}}{2\sqrt{R^{(4)}}} \right) \right]^2 \quad (4.18)$$

Using this technique the effective grating reflectivity for several devices was estimated and the results shown in table 10. The effective reflectivity obtained from experimental data is on the order of magnitude of the theoretical reflectivity presented in chapter 2 and references presented therein. The detuned grating coupler is therefore capable of providing very low effective reflectivity that may not be readily achievable by standard anti-reflection coating without using complex multiple coatings schemes. Gratings with graded duty cycle consistently show lower

reflectivity than gratings fabricated with uniform duty cycle given that the scattering losses at the interface between the passive and active region are minimized by the tapering of the grating coupling coefficient.

Table 10: Effective grating reflectivity estimated from the facet output power measurements. All the other device parameters are identical. The power at the beginning of the grating  $P_g$  is assumed to be 1.1W for all devices at 1A of pumping current.

<i>Substrate coating</i>	NO	NO	YES	NO
<i>HR grating coating</i>	NO	NO	YES	YES
<i>Grating duty cycle</i>	55%	20-55%	20-55%	20-55%
Facet output $P^{(4)}$ (W/A)	0.04	0.02	0.018	0.17
<b>Effective reflectivity <math>R_g</math></b>	<b><math>9.1 \times 10^{-4}</math></b>	<b><math>2.3 \times 10^{-4}</math></b>	<b><math>1.9 \times 10^{-4}</math></b>	<b><math>1.6 \times 10^{-2}</math></b>

Another important conclusion is that the high reflection coating does not seem to influence the effective reflectivity significantly, a fact confirmed by the similar lasing threshold values obtained from devices with and without high reflection coating. However, devices with high reflection coating and no substrate coating exhibit much higher reflectivities, as high as  $2 \times 10^{-2}$ . This phenomenon can be explained by the fact that a significant part of the light reflected by the substrate is coupled back inside the cavity by the grating coupler and cannot be transmitted

through the grating coupler into the air because of the gold layer used for the high reflection coating.

### 4.2.3 Spectral characteristics

In order to measure the spectrum emission of the device, a multimode fiber is placed close to the facet output to collect light from the device and connected to a grating-based optical spectrum analyzer. The low reflectivity mirror created by the grating coupler prevents feedback inside the cavity. For low currents, the emission is therefore broad with a full-width half-maximum bandwidth approaching 8nm at 400mA produced by amplified spontaneous emission (ASE) mechanism, similar to the behavior observed for a superluminescent diode as shown in Fig.47. Such behavior was observed in 1973 by Lee and al. when feedback was suppressed by leaving part of the device unpumped [Lee 1973]. At higher current levels, enough feedback is provided by the cleaved facet so that stimulated emission becomes the main emission mechanism. Multiple longitudinal modes can be observed due to the several spatial modes supported by the broad area stripe and the lack of wavelength selective element inside the cavity. For some devices with shallow grating depth of 200nm and below, a red-shift is observed at lasing due to the absorption in the passive region of the grating. In that case, lasing occurs due to the feedback coming from the residual light not outcoupled by the grating coupler and reflected by the cleaved facet.

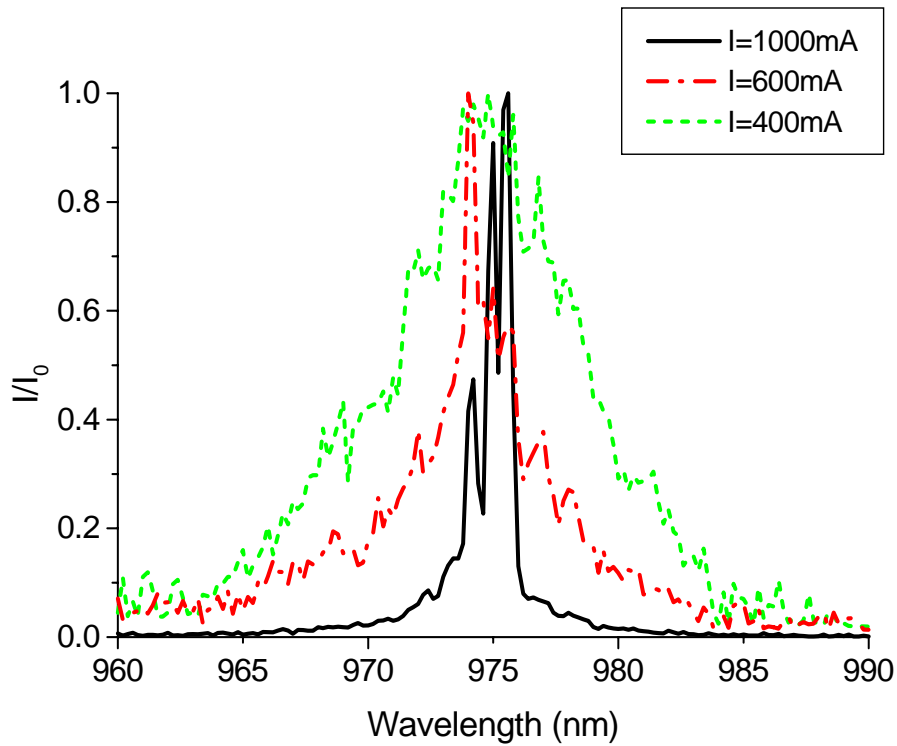


Fig.47: Typical normalized spectrum for a 2mm long GCSEL as a function of pumping current. The resolution of the spectrum analyzer for this measurement is 0.2nm. The pulse width is 500ns and the repetition rate is 1kHz.

The ripples seen on the spectrum are due to reflections between the grating and the substrate coated with the low reflection dielectric coating and correspond to a modulation of period around 0.8nm for a 150 $\mu$ m thick substrate. We will show later in this chapter that a broad spectrum can be obtained at high currents by using a second grating coupler instead of a cleaved facet.

## 4.2.4 GCSEL Near field and far-field intensity profiles

### 4.2.4.1 Near field intensity profile

A clear advantage of the grating coupler is the ability to reshape the mode guided in the semiconductor structure in the direction of the stripe to enhance the coupling to optical waveguides for instance. By controlling the groove features along the grating as described in chapter 3, it is possible to modify the coupling coefficient locally and overcome the traditional exponential decay produced by a uniform grating described by (2.49). We showed that grating duty cycle and depth are strongly coupled through the ARDE effect for submicron features. This coupling strongly affects the grating attenuation coefficient and eventually the near-field intensity profile. In our case, this effect plays in our favor and needs to be exploited. Indeed, if the grating depth was constant, a simple variation of the grating duty cycle would require duty cycle close to 1% ( $\sim 3\text{nm}$  feature) to obtain proper decrease of the coupling coefficient to obtain a slowly rising intensity profile [Touam 1997]. Such features cannot be readily achieved today, even by the newest e-beam tools. Instead, the automatic decrease of the coupling coefficient through coupling between grating duty cycle and depth produces quasi-symmetric near-field profiles while relaxing the requirements on the feature size. A comparison between the variations of the grating decay coefficient  $\alpha$  with and without ARDE is shown in Fig.48.



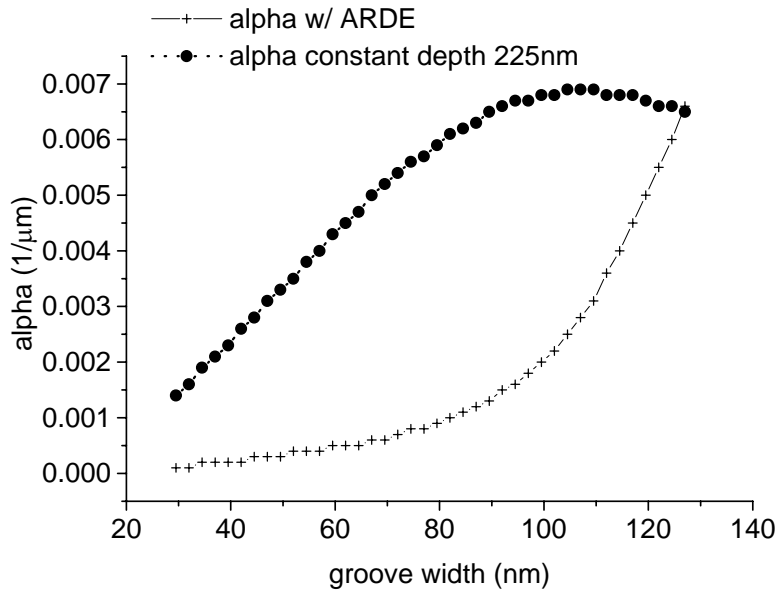


Fig.48: Effect of ARDE on grating decay coefficient  $\alpha$ . The coupling between grating depth and linearly increasing duty cycle produces a slow rising coupling coefficient which produces nearly symmetric near-field intensity profile.

The attenuation coefficient was obtained by the perturbation technique. The coupling between duty cycle and grating depth was modeled using the formula obtained from experimental data presented in chapter 3. The derivation of the ideal attenuation coefficient  $\alpha$  needed to obtain a Gaussian output intensity profile can be found in chapter 6. Based on these observations, we fabricated devices for which grating duty cycle, measured with a scanning electron microscope, was tailored from 20% to 55% by controlling a three pass line exposure dose on the first 80 micron of the grating coupler. The rest of the grating was exposed with a constant exposure dose of  $390\mu\text{C}/\text{cm}^2$ . After completion of the remaining fabrication steps, the device was mounted p-side down for testing. The near field intensity profile was measured by focusing a CCD camera

on the device substrate using a 10X zoom. Devices from the same batch were fabricated with uniform gratings exposed at  $390\mu\text{cm}^2$  for reference. The two profiles are shown in Fig.49 to highlight the impact of the duty cycle variation on the near-field intensity profile.

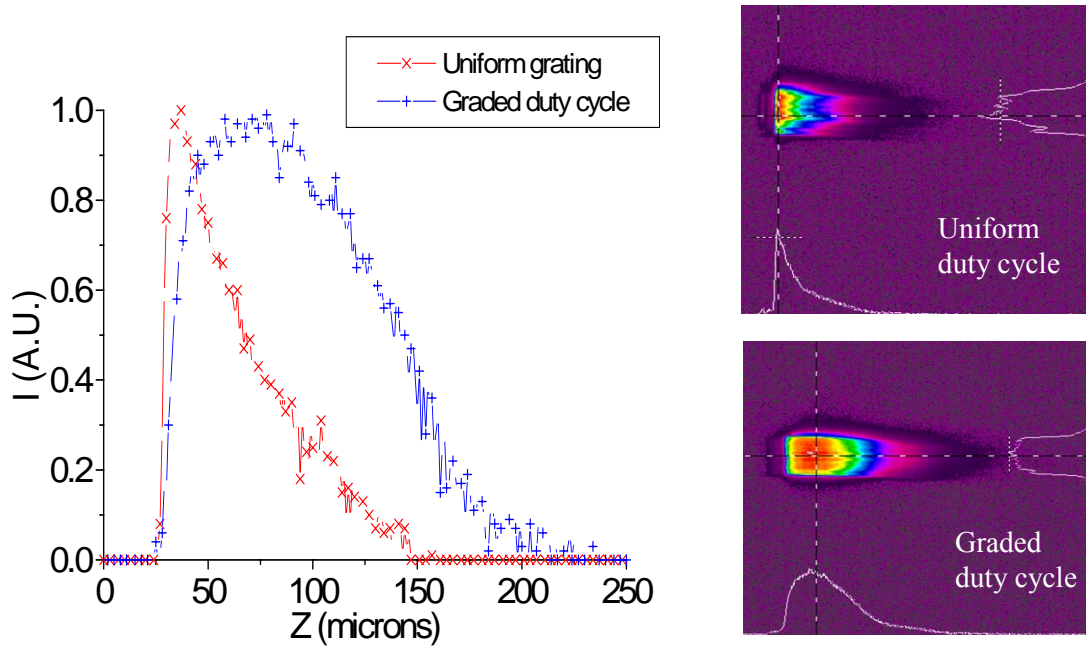


Fig.49: Experimental near-field intensity profiles from gratings with uniform versus graded duty cycle. The duty cycle is varied from 20% to 55%, the grating depth varies accordingly from 210nm to 275nm.

The grating duty cycle versus depth profile was used to model the expected near-field intensity profile by the finite-difference time domain technique outlined in Chapter 2. The grating length was set to  $200\mu\text{m}$ . The vertical component of the pointing vector, derived at the grating plane, was used to compare the predicted versus measured profile as shown in Fig.50. The graded duty cycle region is properly modeled by the FDTD technique as well as the exponential decay in the

uniform duty cycle region. The spikes observed in the FDTD profile correspond to the discontinuities introduced by the sampling of the duty cycle variation profile.

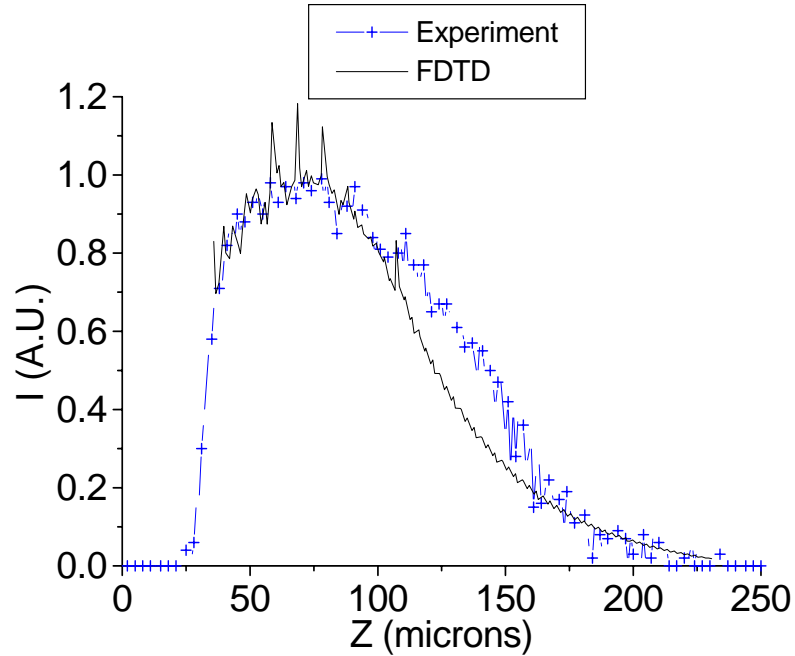


Fig.50: Near-field intensity profile obtained by finite-difference time domain compared to experimental data.

The intermediate region discrepancy may be due to grating nonuniformities or filamentation observed in the 2D profile. A complete 2D near-field intensity profile can then be obtained by convoluting the longitudinal profile obtained by finite-difference time domain by the transverse profile obtained by the self-consistent model of the cavity described in chapter 2. The result is shown in Fig.51. The self-consistent model was run for 19 round-trip loops with a grating reflectivity of  $10^{-4}$  and a cleaved facet reflectivity of 0.32 at a current of 1A. The intensity was averaged over the 5 last loops. The model predicts the propagation of filaments observed

experimentally in the 2D near-field profiles shown in Fig.49. and can be used to model other contact geometries that will maintain a single spatial transverse mode for elevated currents.

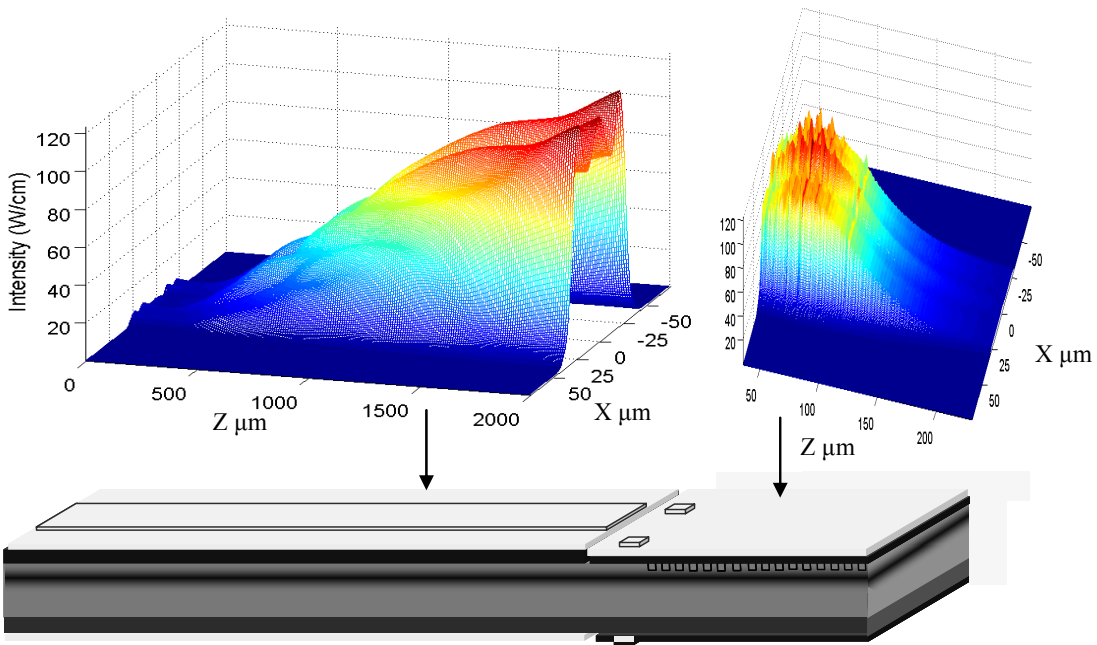


Fig.51: Intensity profile modeling of a 2mm long, 60  $\mu\text{m}$  wide GCSEL inside the active region (left) and along the grating (right) for 1A pumping current.

#### 4.2.4.2 Far-field profile

The far-field profile of the device is measured by placing a diffuser with a ruler grid at a distance of 20cm above the device substrate. The image of the output beam on the diffuser is imaged on a CCD camera. The full-width half maximum of the intensity profile is used to

determine the beam far-field divergence as shown in Fig.52.

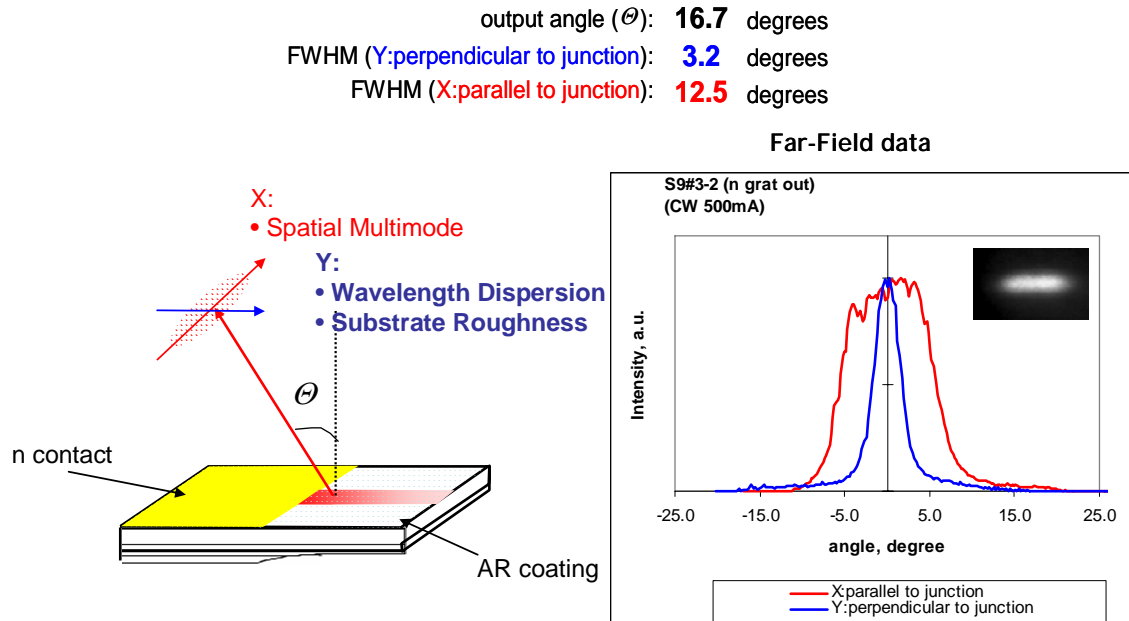


Fig.52: Far-field profile of 2mm GCSEL at 600mA CW pumping current. The divergence angle in the X direction is affected by the multimode behavior of the broad area device while the amplified spontaneous emission bandwidth controls the divergence angle in the Y direction.

The relatively broad divergence in the X direction perpendicular to the stripe is caused by the multimode behavior of the broad stripe device. The divergence in the longitudinal direction is mainly due to spatial dispersion introduced by the grating coupler. Several longitudinal modes as well as the ASE background, seen in Fig.52 for I=600mA, contribute to the wider far-field angle. However, the device still produces a threefold improvement over standard Fabry-Perot devices divergence which is typically  $\sim 7^\circ \times 35^\circ$ . The far-field profile could be made more symmetric by

choosing an alternative geometry such as tapered electrodes or master oscillator power amplifier configuration that can maintain the single transverse mode profile stability [Parke 1993].

#### 4.2.5 High peak power performance

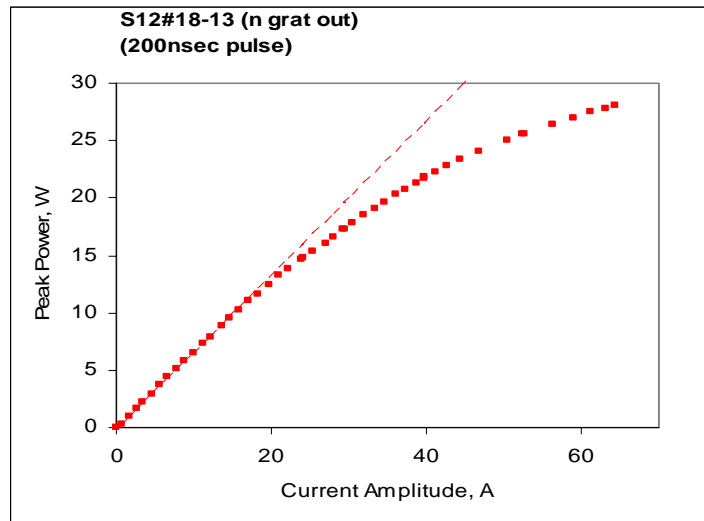


Fig.53: High peak power operation of a 2mm GCSEL. Maximum power is limited by catastrophic optical damage occurring on the uncoated cleaved facet.

The large difference between the residual power measured through the cleaved facet and power measured from the grating side increases greatly the level at which these devices can be operated before reaching catastrophic optical damage. A 2mm long device was tested in high pumping current conditions using a pulse current driver from Directed Energy LDX-100 capable of delivering currents as high as 100A with pulses as low as 50ns. The testing was carried out with

pulses of 200ns at a repetition rate of 2kHz. An output power of 25W was obtained for a current of 50A, as shown in Fig.53, using a thermal detector from Ophir. The device tested produces a slope efficiency of 0.67W/A. Higher power may be obtained by coating the cleaved facet with a standard high-reflection dielectric coating. It is then expected that other degradation mechanisms than COD, such as electrical breakdown or thermal rollover, may limit the performance of the device around 50W peak power.

### **4.3 Crossed-beam superluminescent diode (X-SLD).**

We showed in section 2 of this chapter that the integration of a detuned grating forces the diode to operate in a superluminescent mode at low pumping current levels. This feature is caused by the low reflectivity produced by the grating coupler which suppresses feedback inside the cavity. At moderate current levels, the feedback from the cleaved facet produces enough feedback to create some lasing oscillations and the stimulated emission process overcomes the amplified spontaneous mechanism. By suppressing the cleaved facet and replacing it with a detuned grating coupler, it is expected that the amplified spontaneous emission mechanism can be maintained for higher pumping current and broad spectrum emission can be obtained for high power operation. This feature is also desirable for optical amplifiers applications. Besides, since negative detuning is used for the grating period, the two output beams can be combined a few mm above the device in a single spatial beam as shown in Fig.54. This feature is a net advantage for the X-SLD from standard superluminescent diodes typically based on flared geometries with

high divergence [Du 2003].

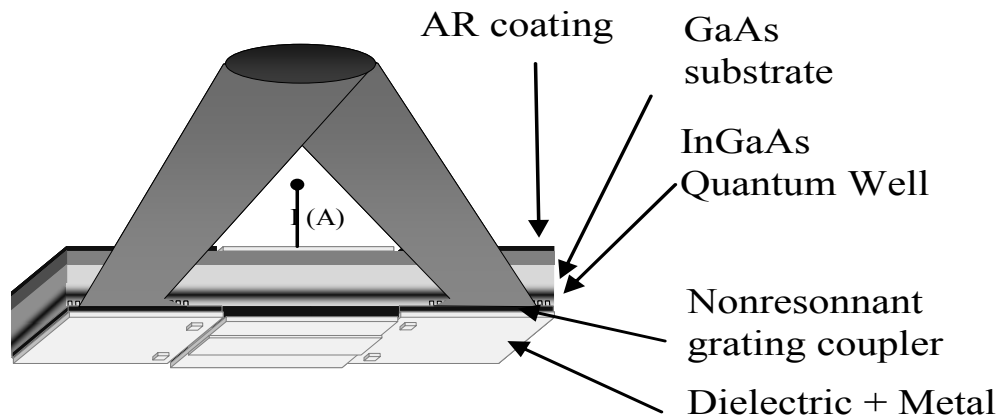


Fig.54: Schematic of the crossed-beam superluminescent diode (X-SLD). The low reflectivity nonresonant gratings prevent lasing oscillation in the cavity. The grating is metallized to increase efficiency through the substrate.

#### 4.3.1 Device performance

Devices with 2mm active length, 100 micron wide stripe, were cleaved and bonded p-side down on Beryllium Oxide heat sink. After wire-bonding, the device was tested in quasi-continuous conditions with a 500 $\mu$ s pulse at 100Hz repetition rate. The thermoelectric cooler temperature was maintained at 20°C. A thermal detector was placed at 4.7mm above the device where the beams from the two grating couplers overlap. The measured slope efficiency was 0.49W/A and



showed a gentle slope around threshold characteristic of amplified spontaneous emission behavior as shown in Fig.55.

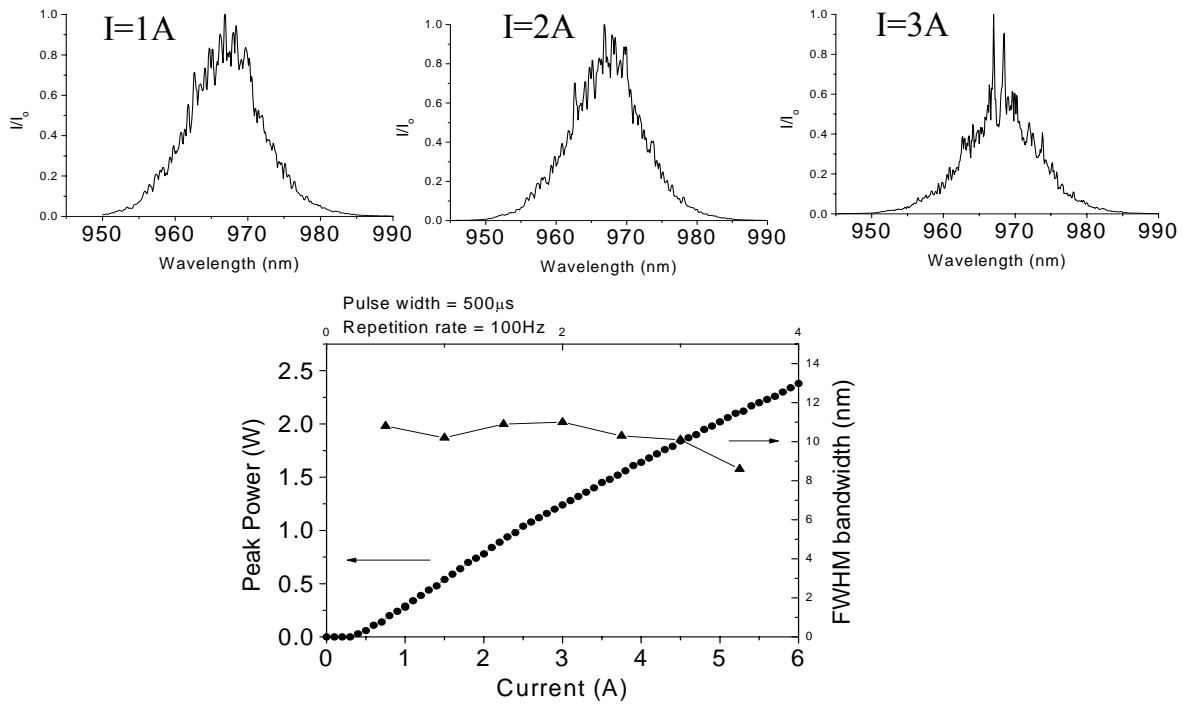


Fig.55: L-I curve of a 2mm X-SLD. The bandwidth of the device remains approximately constant up to the apparition of the lasing oscillations above 4A.

The spectrum was measured by collecting the light diffracted into a multimode fiber connected to a HP86142B optical spectrum analyzer. The resolution was set to 0.1nm. The full width half maximum (FWHM) bandwidth of the device was measured to be above 10nm for currents up to 4A. Lasing oscillations were not visible before pumping currents up to 4A. Even for higher

currents where lasing lines were observed, a wide spectrum was still present due to the poor quality of the resonator and the spatial multimode behavior of the device. Thermal effects started to affect the device efficiency around a current of 4A. In continuous wave operation the slope efficiency was measured around 0.41W/A. In the direction parallel to the junction between active and passive region, the full width half maximum (FWHM) far field divergence angle of the beam is mainly controlled by the aspect ratio of the diode stripe and is given by [Lee 1973]

$$\theta''_{FWHM} = 2 \cdot \sin^{-1} \left( n_{eff} \cdot \sin \left[ \tan^{-1} \left( \frac{W}{L} \right) \right] \right) \quad (4.19)$$

where W is the stripe width, L is the stripe length, and  $n_{eff}$  is the effective index of the guided mode. The calculated theoretical value of 19 degrees is in good agreement with the measured data shown in Fig.56. In the direction perpendicular to the junction, the beam divergence depends upon the emission spectrum bandwidth by the classic equation

$$\theta^{\perp}_{FWHM} = \frac{\Delta\lambda_{FWHM}}{\Lambda \cos(\theta_{-1})} \quad (4.20)$$

where  $\Delta\lambda_{FWHM}$  is the FWHM bandwidth,  $\Lambda$  is the grating period, and  $\theta_{-1}$  is the output angle for the -1 diffracted order in the air. The material and modal dispersion has been neglected. This angle is 2.2 degrees for a 10nm bandwidth at 1A pumping current while it reaches 7 degrees at low amplification level for 300mA pumping current as shown in Fig.56. The beam profile was captured by a charge-coupled camera. The divergence for the beam coming from a single grating was measured to be around 20° by 7° in the direction parallel (X) and perpendicular (Y) to the

grating lines respectively. The overlapping spot shows FWHM diameters of 0.8mm and 2.3mm respectively in the X and Y direction with bell-shaped intensity profiles.

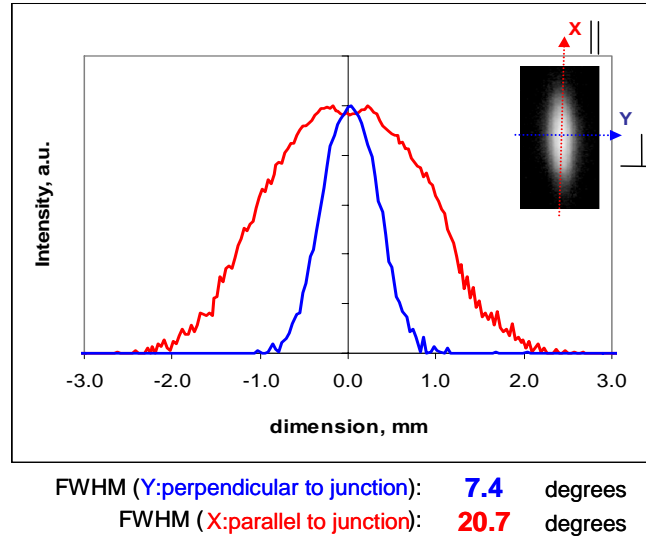


Fig.56: Spatial profile of the overlapped beams captured at 4.7mm above the 2mm long device for 300mA pumping current.

### 4.3.2 Influence of stripe geometry on device performance

The performance of the X-SLD can be explained by a first order model of superluminescent diode as first described in [Lee 1973]. Unlike standard laser diodes where strong feedback from the facet creates a fast gain saturation and abrupt transition from spontaneous emission to stimulated emission mechanism, superluminescent diodes present a region of linear small signal gain where the power  $P$  for the forward and backward propagating waves inside the cavity

follows an exponential dependence upon current described by the first order differential equation

$$\frac{dP^\pm}{dz} = \pm(\Gamma g - \alpha_i)P + P_0 \quad (4.21)$$

where  $\Gamma$  is the quantum well confinement factor,  $g$  is the small signal gain proportional to the current density,  $\alpha_i$  the internal losses coefficient.  $P_0$  is the spontaneous emission power coupled into the waveguide for an infinitesimal length  $dz$  defined as

$$P_0 = \eta_{sp} \left( \frac{h\nu}{q} \right) \cdot \frac{I}{L} \cdot \beta \quad (4.22)$$

where  $I/q$  defines the number of injected electrons,  $\eta_{sp}$  is the spontaneous emission efficiency,  $L$  the device length, and  $\beta$  the ratio of spontaneous power coupled into the waveguide versus the total emitted spontaneous emitted power. Thus, after integration over the length of the device  $L$ , one gets

$$P^\pm(z = L) = \frac{P_0}{(\Gamma g - \alpha_i)} \left( e^{(\Gamma g - \alpha_i) \cdot L} - 1 \right) \quad (4.23)$$

For a given current density, the power at the grating input therefore increases as a function of the device length for a given current density. This trend was verified experimentally by measuring the L-I curves of devices featuring the exact same grating parameters but with various active region lengths 1mm, 2mm, and 4mm shown in Fig.57. This trend is also seen in the external differential efficiency which is typical of amplified spontaneous emission mechanism, unlike

laser diodes for which the external differential efficiency decreases as a function of the active length due to gain saturation and intracavity losses. The only drawback associated with extending the device length is the spectral narrowing of the emission bandwidth that is typically observed.

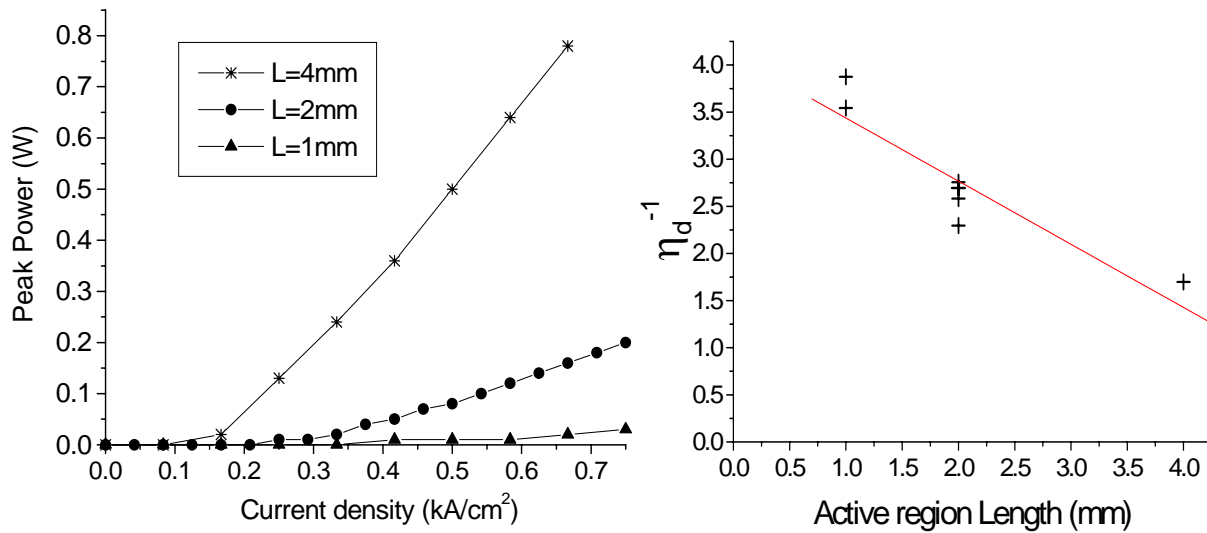


Fig.57: Peak power as a function of current density (left) and differential quantum efficiency for various cavity lengths of 1mm, 2mm, and 4mm (right).

The 4mm device typically shows a FWHM bandwidth of 5nm versus 10nm for a 2mm device and up to 30nm for a 1mm long device with similar current density around 1.6kA/cm<sup>2</sup> as shown in Fig.58. Streifer and al. analyzed the coupling of spontaneous emission into the longitudinal modes of a diode laser and proposed a simple definition of the spectral envelope above threshold by [Streifer 1982]

$$\Delta\lambda \approx \Delta\lambda_h \frac{P_s}{P} \quad (4.24)$$

where  $\Delta\lambda_h$  is the homogeneous spontaneous linewidth,  $P$  is the output power, and  $P_s$  is the saturation power.  $P_s$  is proportional to the resonator reflectivity and the stripe geometry through  $\beta$  [Lee 1982]:

$$P_s \propto W \cdot \left( \frac{1-R}{\sqrt{R}} \right) \cdot \beta \quad (4.25)$$

where  $\beta$  is defined as the ratio of spontaneous power coupled into the waveguide versus the total emitted spontaneous emitted power. In an X-SLD or any similar superluminescent device, all the power emitted isotropically by spontaneous emission and captured by the waveguide will be amplified and will contribute to the emission output.

$$\beta \approx \frac{1}{\pi} \sin(\theta_c) \tan^{-1} \left( \frac{W}{L} \right) \quad (4.26)$$

where  $\theta_c$  is the critical angle defined by the gain-guided index difference,  $W$  is the stripe width and  $L$  is the device length. Since the saturation power therefore increases while the stripe aspect ratio decreases, devices with short length and wide stripe will produce broader emission bandwidth as seen in Fig.58. Note that, following (4.24), the FWHM bandwidth is inversely proportional to the output power and for similar current density, the output power is greater for longer device length. From (4.25), it is also clear that low reflectivity from the grating coupler

increases the FWHM bandwidth of the device which mathematically translates the fact that the lack of feedback prevents an efficient stimulated emission process to occur.

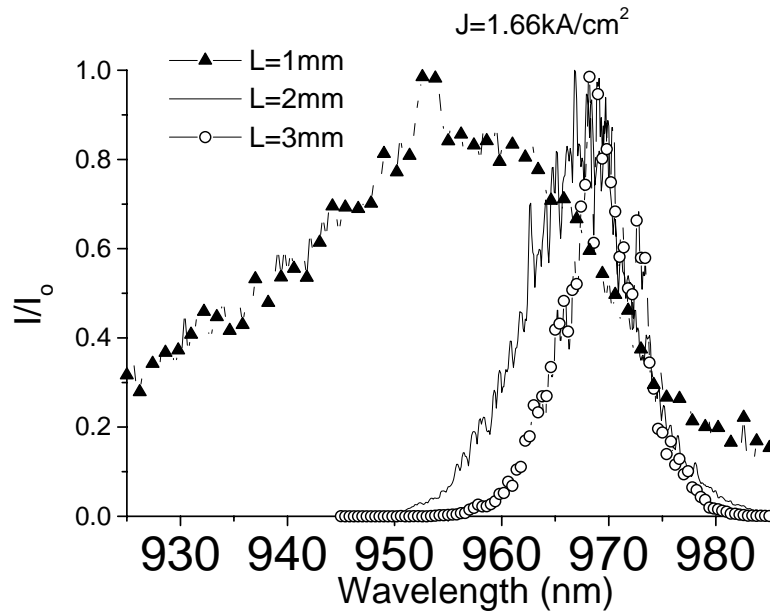


Fig.58: Spectrum of a 1mm, 2mm and 4mm long X-SLD for a current density of  $1.66\text{kA/cm}^2$ . The current pulse width is 500nS, repetition rate of 1kHz. The coefficient  $\beta$  can then be derived geometrically and is given by [Zhao 1999].

For standard laser diodes where light is produced by lasing oscillations, only the spontaneous power emitted along the path of the oscillation modes will contribute to the emission and the ratio of spontaneous power coupled to lasing modes decreases when the device width increases. However, for superluminescent devices such as the X-SLD, as long as there are no oscillations, more spontaneous power is amplified and contributes to the output power as the device width

increases. Consequently, the device efficiency will increase as a function of the device width. Experimentally 10 $\mu$ m wide stripe devices showed efficiency on average around 8 times lower than 100 micron wide stripes devices for 1mm device length. However, we observed little differences between devices of 60 $\mu$ m and 100 $\mu$ m. A possible explanation is that for device widths larger than 60 $\mu$ m, the amount of spontaneous emission contributing to the emission output tends to saturate as the geometrical angle of rays emitted from inside the cavity becomes larger than the critical angle and therefore is not coupled outside the waveguide. Similar reasoning can be applied to predict the far-field beamwidth as a function of the stripe geometry [lee 1973].

### **4.3.3 High peak power performance**

The greater efficiency obtained from a 4mm device makes the X-SLD a very good candidate for high power applications. The corresponding device resistance decreases as the p-contact area increases. Consequently, the corresponding current-induced heating produced at high power levels and potentially reducing thermal effects. We therefore decided to test a 4mm long device, 60 $\mu$ m long device with a pulse width of 100ns and repetition rate of 5kHz. The electrical pulse was monitored using an oscilloscope to watch for pulse distortions during the peak power measurements. A maximum peak power of 32 W was obtained for a pumping current of 61 A. However, at this current level, many lasing oscillations can be observed. Unlike the GCSEL device with uncoated cleaved facet, no optical damage was observed on the device with two



grating couplers due to the large emitting area of the grating couplers used to replace the facet.

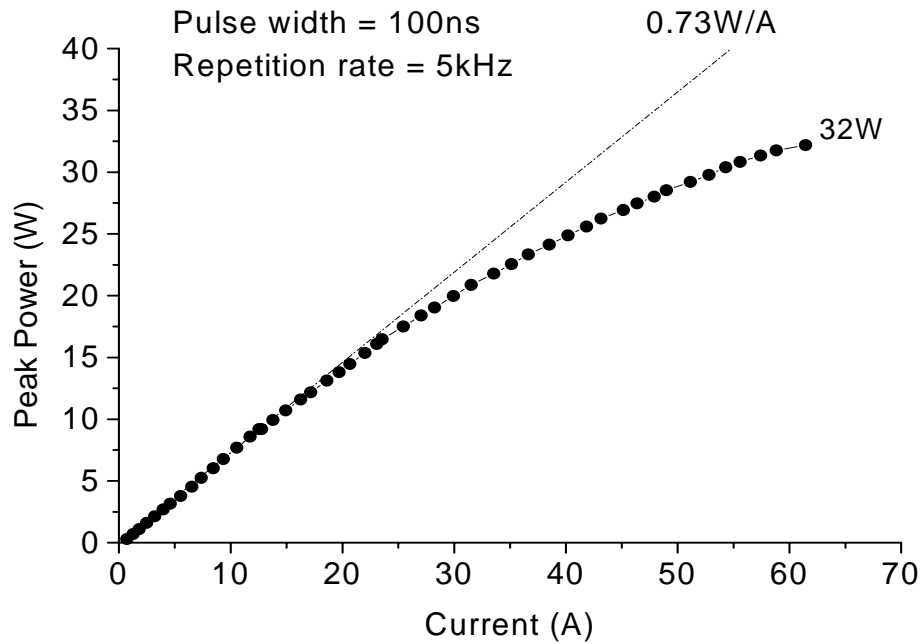


Fig.59: High current performance of a 4mm long device with two grating couplers. Thermal effects limit the power to 32W for 60A current. The large grating coupler emitting area eliminates catastrophic optical mirror damage. Above 3.5A, many lasing oscillations can be observed.

#### **4.4 Conclusion**

We analyzed the GCSEL device performance using a detailed analysis of the losses related to the substrate free-carrier absorption and losses in the passive region. We used this analysis to quantify the grating efficiency to demonstrate that the fabrication process developed for this dissertation produces grating efficiency as high as 98.5%. We showed that when the grating decay coefficient is close to the passive region loss coefficient, one must take into account a

power-dependent loss effect that may be used for saturable absorber purposes. When the grating decay coefficient is large compared to the passive region loss coefficient, good agreement is found with finite-difference time domain modeling used to predict the improved near-field intensity profile produced by gratings with graded duty cycle. A complete 2D profile of the device showing the impact of the broad area stripe on the transverse mode quality was obtained using a self-consistent model that also provided insight about the device behavior by showing a single pass gain intensity pattern inside the GCSEL cavity. A comparison between output power from the facet and the grating side was used to evaluate the low grating effective reflectivity and confirms the predicted theoretical value of  $1-5 \times 10^{-4}$ . The ultra-low reflectivity of the grating coupler was used to suppress feedback inside the cavity by replacing both facets by grating couplers. The feedback suppression produces broad spectrum emission characteristic of superluminescent diode. An analysis of the device performance versus stripe geometry confirmed that the device works as a single pass gain element. The X-shaped output beam coming out of the device can be used in the overlapping area without collimating optics. This novel superluminescent device can produce up to 1.5W QCW with 11nm bandwidth [Vaissie 2004(a)] with a 2mm long active length. No lasing oscillations are observed until around 3.5A. Also, the large emitting area enabled high peak power of 32 W without COMD from a 4mm device with a current of 60A. In summary, we have fabricated high efficiency surface emitting devices by integrating high quality and very low reflectivity grating couplers with semiconductor diodes. The surface-emitting devices produce a good quality, high efficiency and high power beam through the device substrate. We will now investigate how the integration of a second

optical element on the device backside can further improve the device beam profile, efficiency, or functionality.

## **CHAPTER 5: INTEGRATION OF BACKSIDE OPTICAL ELEMENT**

The device configuration presented in the previous chapter enables the integration of a second passive optical element on the diode substrate to further improve the performance of the device. In this chapter, we demonstrate the monolithic integration of three different elements as examples of the versatility of the proposed device configuration. The first element is a refractive lens used to reshape the beam at 1mm above the device suitable for efficient coupling to multimode fibers. The second element demonstrates how the device efficiency can be greatly improved by fabricating a tapered subwavelength antireflection coating on the GaAs substrate. Finally we present the integration of a fan-out element to demonstrate that beam-shaping functions can be monolithically integrated on the device substrate without creating additional feedback inside the cavity and affecting the device performance.

### **5.1 Monolithic lens integration by focused ion beam (FIB)**

Recently several research efforts focused on integrating beam-shaping elements with laser diodes to avoid the cost and alignment process of external optics. For example, the integration of a lens on the end facet of an edge-emitting laser diode was recently demonstrated using focused-ion beam etching [Rashed 2002] and deposition [Fu 2002]. However the end facet integration is not suitable for low cost wafer-based fabrication. Other devices based on a single beam-shaping

element in VCSEL's have been introduced for low power applications [Martinsson 1999]. For moderate to high power, in-plane laser configuration must be used. Multiplexed grating schemes have been demonstrated through the use of grating-coupled semiconductor lasers for beam shaping and splitting applications [Eriksson 1997]. However, one major disadvantage of the multiplexed grating coupler is that the dislocated grating creates a high level of feedback into the laser cavity which leads to increased filamentation resulting in severe wavefront distortion of the output beam [Modh 2002]. In order to minimize the feedback into the cavity, the beam shaping function must be decoupled from the grating. The solution to this is to couple the diffracted light through the substrate and out of the opposite side. In this approach the device substrate is used to integrate the beam shaping optical element separately from the outcoupling element. The integration of a bifocal refractive lens on a laser diode substrate was first proposed by Liao and al. [Liao 1990]. In this work, light was directed towards the substrate by a 45 degree mirror etched on the p-side of the device. The problem with such a configuration is twofold. First, the mirror angle needs to be controlled very accurately since the high substrate index of refraction amplifies greatly any deviation from the 45 degree mirror into deviations of the output angle [Stegmüller 1991]. Secondly, the mirror does not compensate for the beam divergence and the integrated lens function must be bifocal to collimate the beam in the longitudinal and transverse directions without possibility of focusing the output beam. These drawbacks are eliminated if a grating coupler is used to decrease the divergence and circularize the output beam as shown in chapter 4. We present in this section the integration of a 40 level refractive lens on the GaAs substrate of a grating-coupled surface emitting device [Vaissie 2003].

### 5.1.1 Lens fabrication

In this section, we describe the fabrication of a multilevel refractive lens using direct milling focused ion beam (FIB) on the GaAs substrate of a GCSEL device. The FIB tool is based on a liquid metal ion source from which Gallium (Ga) ions are extracted. The ions are accelerated by a high voltage of 30kV. The details of the column of a FEI 200 tool similar to the one used for our work is shown in Fig.60. The sample can be placed at eucentric height so that the center of the image is not shifted when the sample is tilted.

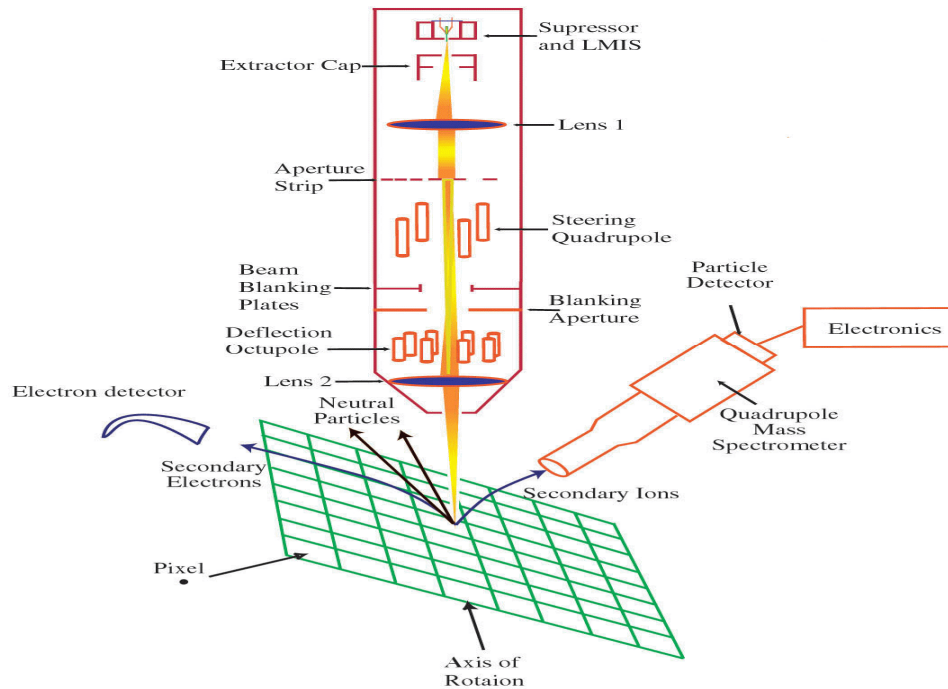


Fig.60: Focused ion beam FEI 200TEM column showing milling and imaging mechanisms (source Alan Kubis, University of Virginia).

The collision of the Gallium ions with the sample produces secondary electrons and ions as well as neutral species. The ions are implanted inside the material while atoms are removed from the sample by sputtering. The addition of gas through a needle placed close to the sample can improve the etching rate and roughness by producing chemical assisted ion beam milling. However this option was not available for our work and therefore the etching mechanism is pure sputtering. The advantage of the FIB tool is it can use direct-writing technique by scanning the beam across the sample without the need for masking techniques as in standard photolithography. The pattern is designed using custom-made software written by Waleed Mohammed from the Microphotonics group at the College of Optics and Photonics. The multilevel refractive lens is fabricated using an additive milling technique. This technique depends on the quantization of the optical element surface into several discrete levels of specific heights. Each level can be represented by basic geometrical shapes or a more complicated stream file. The basic geometrical shapes are rings and circles. For a spherical lens of desired focal length  $f$ , the depth of the structure is given by

$$\delta = R - \sqrt{R^2 - (W/2)^2} \quad (5.1)$$

where  $W$  is the diameter of the lens and  $R$  is the radius of curvature that equals  $(n-1)f$ ,  $n$  being the refractive index of the material. Fig.61 shows the quantization of the lens surface into  $N$  levels of equal heights  $\delta_i = \delta/N$ . The radius of each level is calculated from

$$r_i = \sqrt{R^2 - (R - (N - i)\delta_i)^2}, i \in \mathbf{N}, \quad (5.2)$$

The fabrication procedure starts by milling a ring of inner radius equal to  $r_{N-1}$  and depth of  $\delta l$ . The outer radius should be greater than or equal to  $W/2$ . Next, a concentric ring of inner diameter of  $r_{N-2}$  and the same outer radius is milled to the same depth. The process repeats till the N rings are milled to the desired depth. In this configuration, each ring is conveniently milled at the same depth which translates into the same milling time per surface unit being attributed to each level. However, the inner ring diameter varies for each level. This may result in non-uniform curvature of the lens since the center of the lens is not milled. This flat center may be to blame for the  $4\lambda$  defocus aberration shown in Fig.61.

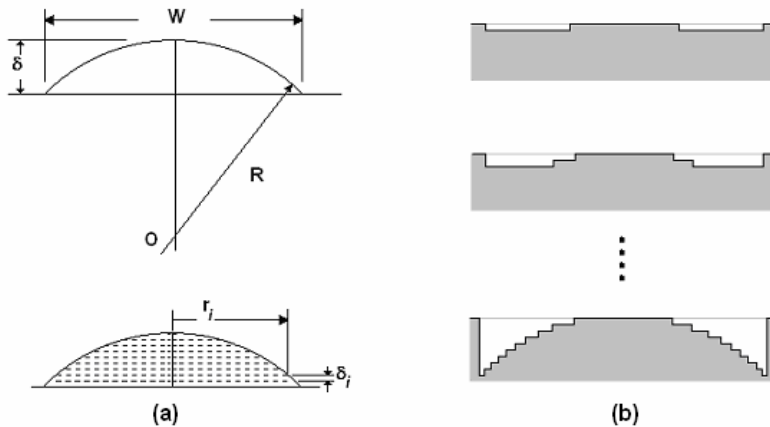


Fig.61: Quantization of the lens for fixed depth increment.

The lens fabricated for this work was milled in GaAs with a 7nA  $\text{Ga}^+$  ion beam at a rate of  $0.41\mu\text{m}^3/\text{nA}/\text{s}$ , in agreement with previously published work [Young 1990]. The multi-level lens was fabricated by milling forty rings with different inner diameters as explained in Fig.61. A



white light ZYGO profilometer was used to determine the curvature and estimate the aberrations of the lens as shown in Fig.62. The curvature corresponds to a 1mm focal length with a  $3.5\mu\text{m}$  sag.

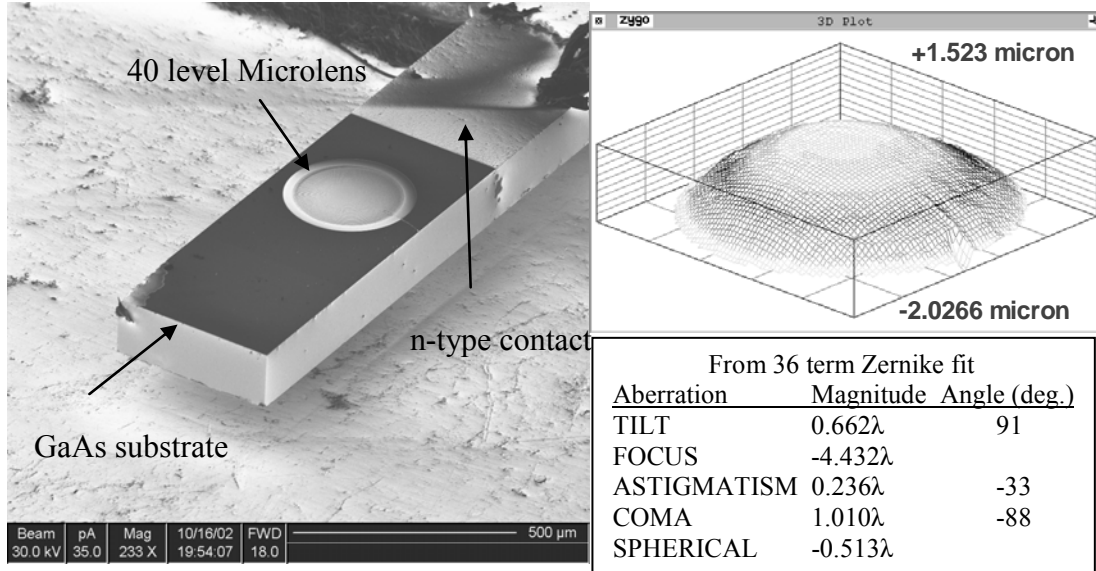


Fig.62: SEM picture of the device substrate with the integrated microlens and 3D white light interferometer profile of the fabricated lens.

### 5.1.2 Device performance

The lens was integrated on a first generation device for which overall efficiency and performance was lower than the devices presented in chapter 4. The laser diode material was MOCVD grown AlGaAs-GaAs graded index structure with a single 6nm thick InGaAs quantum well for an emission wavelength around 970 nm. The broad area gain stripe is 100 microns wide by 2mm long. A 100nm thick Si<sub>3</sub>N<sub>4</sub> layer was deposited on the p-doped surface to be used as a mask to

transfer the pattern. The 275nm period grating was then patterned in Poly(methyl methacrylate) (PMMA) using EBMF Leica/Cambridge 10.5/CS electron-beam lithography system at the Cornell Nanofabrication Facility at 40kV and 1nA current. The pattern was successively transferred into the Si<sub>3</sub>N<sub>4</sub> layer with a Reactive Ion Etcher and into the laser diode with an Electron Cyclotron Resonance (ECR) plasma etcher using Chlorine-based chemistry. After the grating was fabricated, the wafer was thinned and an n-electrode was patterned on the backside. Lift-off technique was used to open a non-metallized window on the substrate side allowing the transfer of the second optical element. The wafer was then cleaved and the devices were tested p-side down under quasi-continuous conditions (pulse width of 500 ns at 1 kHz). A CCD camera and a 10X zoom were used to characterize the near field intensity profile on the substrate side for accurate placement of the lens. A FIB inspection showed the uniform grating duty cycle was around 20% and the depth 240nm. No high reflection coating was deposited on this device. The near-field intensity profile showed a typical exponential decay with a measured outcoupling length around 160µm. The device was tested at 1A with a pulse width of 500ns at 1kHz repetition rate. First, an image of the lens was taken and used for calibration purposes. Then the device and probe were translated vertically and images were recorded by focusing on a fixed 0.5 micron grain size diffuser, located at the initial position of the lens. Density filters were used to avoid saturation of the CCD camera. Recorded images were normalized and full width half maximum contours were calculated. The effect of the lens on the full width half maximum of the longitudinal intensity profile (X) and two corresponding dimensional plots are shown in Fig.63.

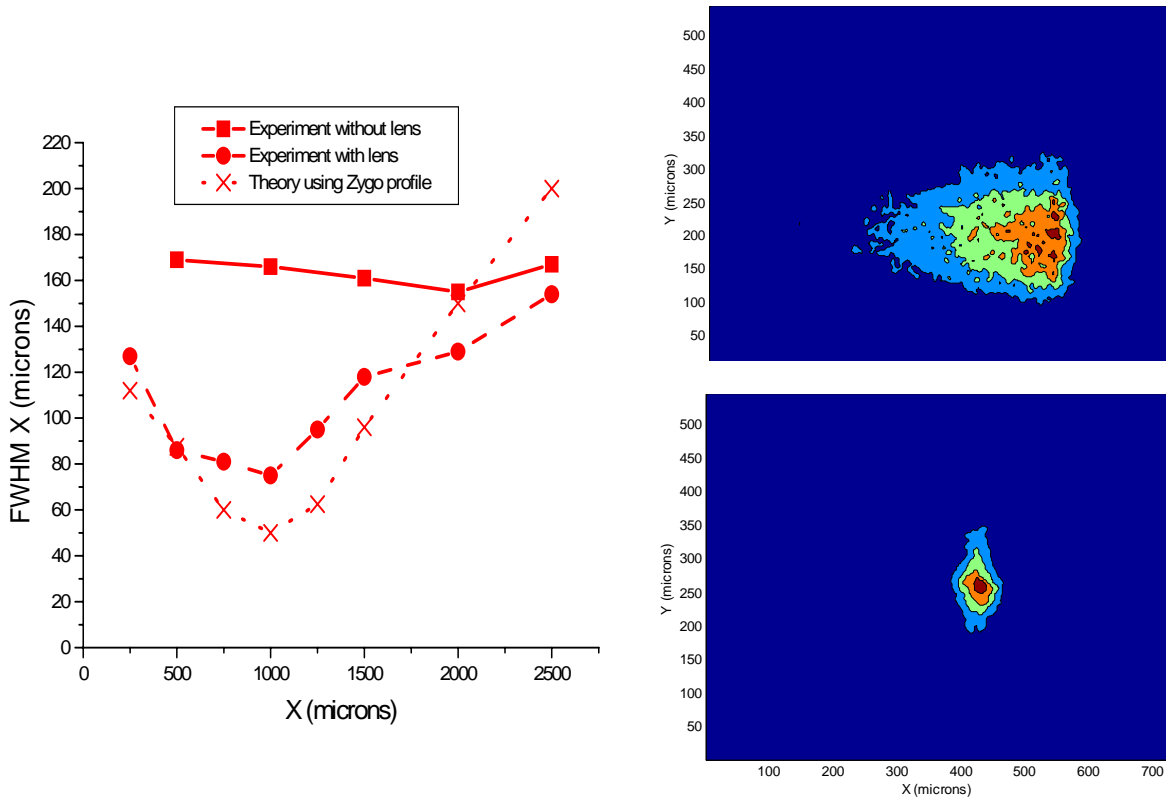


Fig.63: Full-width half-maximum variation of the intensity profile with respect to distance from the lens (left). The four level contour images captured with (bottom right) and without the lens (top right) after 1mm propagation illustrate the focusing effect of the fabricated microlens.

The experiment confirms that the lens has a 1mm focal length, similar to what was calculated from the profile measurements. The output beam profile shows a twofold reduction of the longitudinal full width half maximum 1mm away from the lens. A 2D Fresnel propagation kernel was used to propagate the exponential amplitude profile coupled out of the grating through a lens using the profile obtained from the Zygo measurements. The results confirm the location of the focal length 1mm above the device substrate. A fair comparison between experimental and

theoretical results is made more difficult by the asymmetry of the beam profile which affects the calculation of the FWHM intensity diameter as well as the multiple longitudinal lasing modes that broaden the beam FWHM in the X direction and are not included in the modeling. Also the transverse mode profile of the output from the grating coupler is multimode, which deteriorates the quality of the focused spot in the Y direction. However both theoretical and experimental results confirm that the lens aberrations limit the ultimate performance of the device in the longitudinal direction to more than 45 microns. Despite the limitations inherent to the lens fabrication and the transverse multimode behavior produced by the broad area stripe, the measured 75 micron full-width half-maximum near circular output may be suitable for direct pumping of multimode fiber or solid-state laser rods. The performance of the lens may be improved in several ways. First, the quality of the transverse mode profile may be improved by using a flared electrode instead a broad stripe to maintain a single mode spatial beam profile. Secondly, the longitudinal intensity profile may be made more symmetrical by grading the duty cycle as shown in chapter 3. Finally the lens may be fabricated by a different additive milling technique or techniques relying on additive lithography [Pitchumani 2002]. Increasing the number of levels will improve the surface profile and roughness. On the other hand, increasing the number of levels will also increase the probability of the rings to be shifted due to the machine error in allocating the center coordinates for each new ring. For the focused ion beam FEI 200TEM we used, the error may be as large as 0.25  $\mu\text{m}$ .

## 5.2 Tapered subwavelength antireflection coating

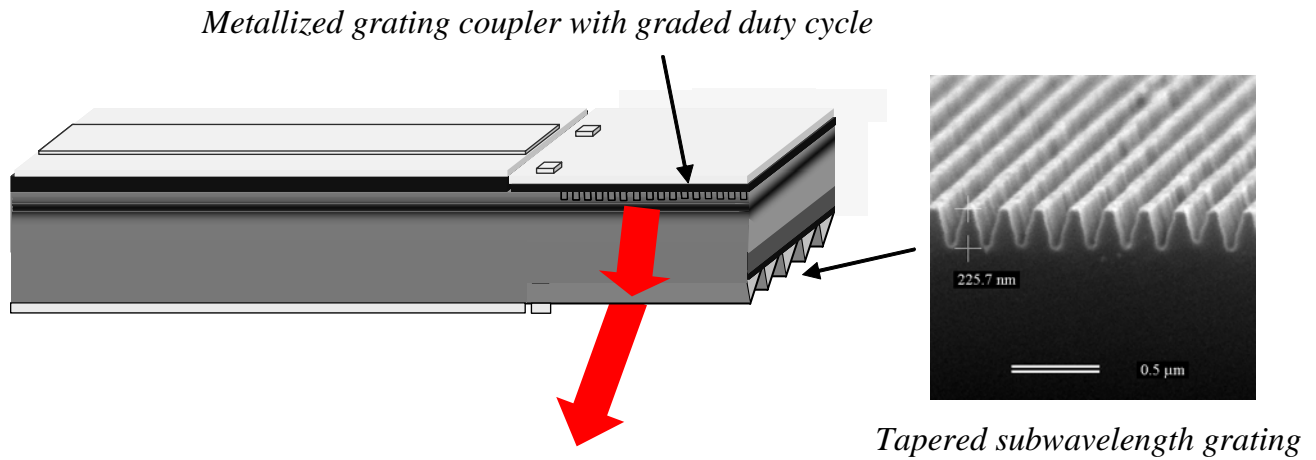


Fig.64: Diagram of subwavelength grating integrated on the device substrate.

The GCSEL or X-SLD configuration presented in this work relies on extracting the light from the GaAs substrate of the device. Due to the high index of refraction of GaAs and the high free-carrier absorption losses of  $9\text{cm}^{-1}$  in the substrate, the device efficiency strongly depends on the quality of the anti-reflection coating deposited on the substrate. In this section, we discuss the fabrication of a tapered subwavelength grating in GaAs as a monolithic alternative to the dielectric antireflection coating as shown in Fig.65 [Vaissie 2004(b)].

### 5.2.1 Tapered 1D subwavelength grating (SWG)

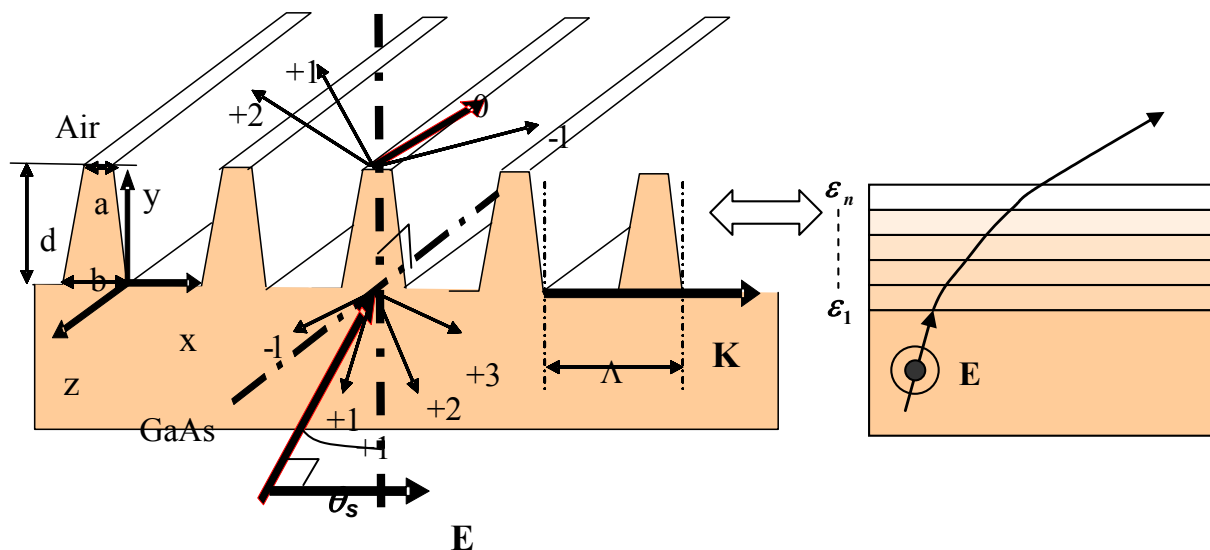


Fig.65: Diagram of trapezoidal 1D grating and equivalent film-stack of gradient refractive index. The polarization direction and the incident angle are set by the grating coupler.

The concept of using subwavelength periodical structures to create an antireflection surface has been implemented in the fabrication of achenic chambers for decades. The concept was extended to the smaller scale of optical wavelengths after Bernard's discovery in 1967 of the structured cornea of night-flying moth [Bernard 1967]. The first experimental verification using “man-made” material came in 1973 with work of Clapham and Hutley with a periodic array made using photolithography [Clapham 1973].

If we consider a 1D grating of period  $\Lambda$ , there is a domain where only the  $0^{\text{th}}$  order will be transmitted while the other diffracted orders will be cut-off. The projection of the incident

wavevector along the direction of the grating wavevector  $\mathbf{K}$  can be expressed as a function of the polar and azimuthal angles  $\theta_s$  and  $\phi_s$  respectively to obtain the upper limit the upper limit for  $\Lambda$  is given by [Grann and al. 1994]:

$$\Lambda_{\max} = \left\{ \frac{\lambda}{\sqrt{\max(n_a^2, n_s^2) - (n_s \sin \theta_s \sin \phi_s)^2 + |n_s \sin \theta_s \cos \phi_s|}} \right\} \quad (5.3)$$

In our case,  $\theta_s$  is the incident angle given by

$$n_s \sin \theta_s = n_f - \frac{\lambda}{\Lambda_g} \quad (5.4)$$

where  $n_f = 3.31$  is the mode effective index and  $\Lambda_g = 270nm$  is the period of the grating coupler. We also consider that the subwavelength grating grooves are perpendicular to the grating coupler grooves, therefore  $\phi_s = 0$ . One then gets, given  $n_{GaAs} = 3.54$  at  $\lambda = 970nm$

$$\Lambda_{\max} = \frac{\lambda}{n_{GaAs} + n_f - \frac{\lambda}{\Lambda_g}} = 304nm \quad (5.5)$$

However, this limit is valid for a plane wave only and may not be restrictive enough for a finite beam that can be decomposed into plane waves of different angles of incidence. We therefore decided to use a smaller period of 200nm for the fabricated element. In that case the SWG can be represented by a stack of layers of uniform effective permittivity with relatively good confidence. Rytov investigated the electric field propagation in a stratified medium for the case

where the electric field is parallel or perpendicular to the grating vector [Rytov 1956]. The effective medium properties derived from this work can be used to model the properties of subwavelength gratings under a technique called Effective Medium Theory (EMT). Although the EMT technique is an approximation compared to rigorous coupled wave analysis (RCWA), it can evaluate the reflectivity accurately as long as the ratio of the SWG period versus the wavelength is less than 0.3 and only the zeroth order is allowed to propagate [Richter 1995]. We consider in this work a second order approximation in the period to wavelength ratio so that the effective permittivity is given by [Raguin and Morris 1993]

$$\begin{cases} \varepsilon_{E\perp K}^{(2)}(\mathbf{y}) = \varepsilon_{E\perp K}^{(0)}(\mathbf{y}) \left[ 1 + \frac{\pi^2}{3} \left( \frac{\Lambda}{\lambda} \right)^2 f(\mathbf{y})^2 (1-f(\mathbf{y}))^2 \frac{(\varepsilon_a - \varepsilon_s)^2}{\varepsilon_0 \varepsilon_{E\perp K}^{(0)}} \right] \\ \varepsilon_{E\parallel K}^{(2)}(\mathbf{y}) = \varepsilon_{E\parallel K}^{(0)}(\mathbf{y}) \left[ 1 + \frac{\pi^2}{3} \left( \frac{\Lambda}{\lambda} \right)^2 f(\mathbf{y})^2 (1-f(\mathbf{y}))^2 \frac{(\varepsilon_a - \varepsilon_s)^2 \varepsilon_{E\perp K}^{(0)}}{\varepsilon_0} \left( \frac{\varepsilon_{E\parallel K}^{(0)}}{\varepsilon_s \varepsilon_a} \right)^2 \right] \end{cases} \quad (5.6)$$

where  $\varepsilon_a$  denotes the permittivity in the air and  $\varepsilon_s$  the permittivity of the GaAs substrate and the zeroth order approximation of the medium permittivity is given by

$$\begin{cases} \frac{1}{\varepsilon_{E\parallel K}^0(\mathbf{y})} = \frac{f(\mathbf{y})}{\varepsilon_a} + \frac{1-f(\mathbf{y})}{\varepsilon_s} \\ \varepsilon_{E\perp K}^0(\mathbf{y}) = f(\mathbf{y}) \cdot \varepsilon_a + (1-f(\mathbf{y})) \cdot \varepsilon_s \end{cases} \quad (5.7)$$



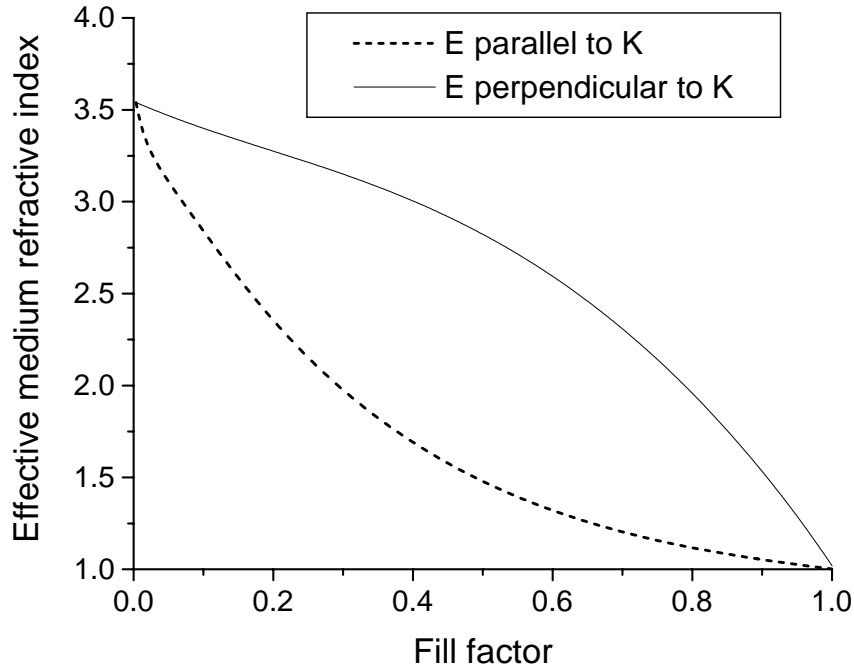


Fig.66: Index of refraction of the effective medium as a function of the fill factor.

The filling factor of the trapezoidal profile shown in Fig.65 is given by

$$f(y) = \frac{a}{\Lambda} + \frac{b-a}{\Lambda} \cdot \frac{y}{d} \quad (5.8)$$

The effective index as a function of the fill factor is shown in Fig.66. For a triangular profile, the curves also represent the variation of refractive index  $n_j = \sqrt{\epsilon_j}$  for the film stack represented in Fig.65. The case where the electric field is parallel to the grating vector produces a slower variation of the refractive index at the top of the grating which is believed to be responsible for

lower reflectivity factors. The reflectivity is analyzed using classic multilayer stack analysis [Ono and al. 1987]. The amplitude reflection coefficient is given by

$$\rho_j = \frac{r_j + \rho_{j+1} \exp(2i\delta_{j+1})}{1 + r_j \rho_{j+1} \exp(2i\delta_{j+1})}, \quad j = 1..N - 1 \quad (5.10)$$

with the phase delay inside the  $i$ th layer given by

$$\begin{cases} \delta_j = \frac{2\pi n_j d_j}{\lambda} \cos \theta_j \\ \sin \theta_j = \frac{n_{eff} - \frac{\lambda}{\Lambda_g}}{n_j} \end{cases} \quad (5.11)$$

The solution for the multilayer stack is obtained iteratively and the reflectivity for the subwavelength grating is obtained by

$$R_{swg} = |\rho_0|^2 \quad (5.12)$$

The coefficient  $r_j$  is the Fresnel reflection coefficient and is polarization dependent. However, in the case investigated here, the polarization of the electric field is fixed by the GCSEL such that the electric field is perpendicular to the multilayer film stack, no matter what is the orientation of the SWG grooves. The reflectivity coefficient is shown in Fig.67 as a function of the grating depth. The profile is assumed to be triangular. The angle of incidence is governed by the grating coupler period of 270nm and the effective index of the mode in the waveguide measured at 3.31. The wavelength is set to 970nm.

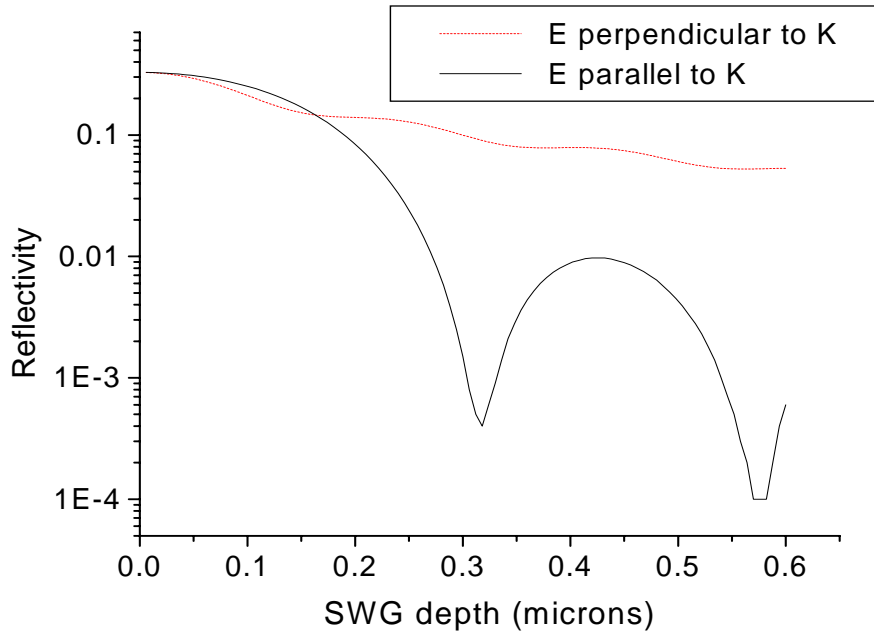


Fig.67: Reflectivity versus SWG depth for two orientations of the grating grooves. The profile is triangular approximated by 200 layers. A minimum reflectivity of  $3.5 \times 10^{-4}$  is estimated for a depth of 325nm.

The reflectivity is lower for the case where the grating grooves are oriented perpendicular to the electric field polarization due to a slower index gradient. All the further results will therefore be presented for this configuration. The variation of the reflectivity as a function of the grating shape is shown in Fig.67. The two extreme cases correspond to triangular and 50% duty cycle rectangular profiles. A sloped sidewall profile clearly provides lower reflectivity due to the index gradient equivalent to a multilayer stack. A square grating ( $a = \frac{\Lambda}{2}$ ) is equivalent to a single layer so the reflectivity oscillates periodically as expected from the phase requirements needed to

obtain low reflectivity peaks.

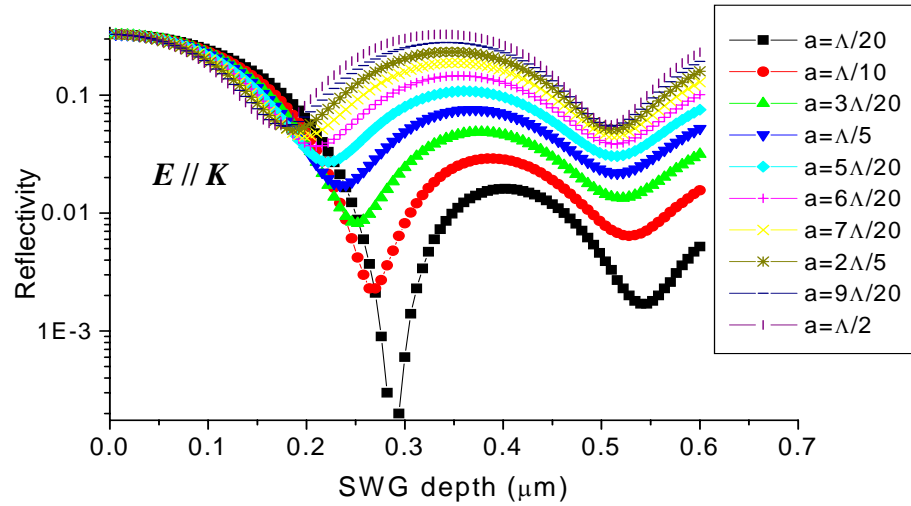


Fig.68: Reflectivity versus SWG depth for various trapezoidal profiles for  $E // K$  configuration. The geometry of the SWG is defined in Fig.65.

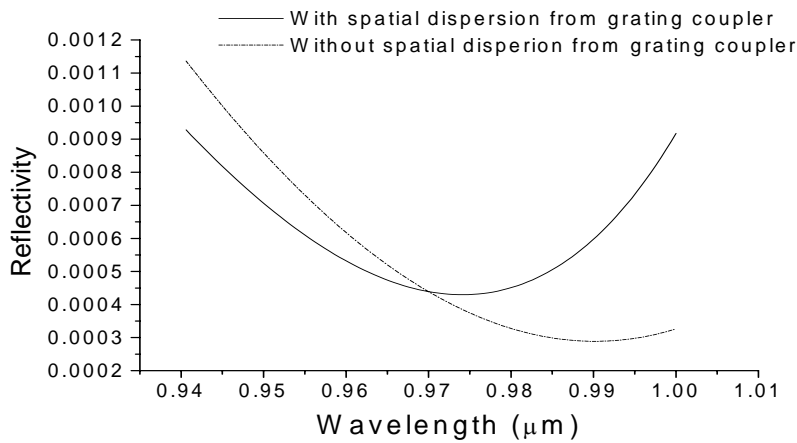


Fig.69: Reflectivity versus wavelength for a triangular profile. The SWG depth is set to  $d=320\text{nm}$  and  $E // K$ . The effect of the spatial dispersion introduced by the grating coupler is also shown for  $\Lambda_g = 270\text{nm}$ .

A tapered SWG profile also produces low reflectivity over a broad spectrum. The reflectivity versus emission wavelength is shown in Fig.69. At a predicted depth of 320nm, the reflectivity remains below  $10^{-3}$  for an emission wavelength varying from 940nm to 1 $\mu$ m. The spatial dispersion from the grating coupler is also taken into account but the GaAs material dispersion was neglected. From the analysis reported in this section, one can conclude that an optimum subwavelength antireflection coating may be obtained by fabricating a 200nm period grating with close to triangular profile in GaAs at a depth around 320nm for a peak transmission at a wavelength of 970nm. We will now describe a process based on mask erosion that allows the fabrication of such profiles.

### 5.2.2 Fabrication

The control of the slope of the grating sidewall profile can be achieved by dry etching techniques. Unlike wet-etching where the slope is mainly controlled by the crystallographic properties of the substrate, dry-etching techniques provide a more precise and flexible way of controlling the grating structure. One technique proposed by Kanamori and al. [Kanamori 2002] uses alternate etching technique using the SF<sub>6</sub> and Cl<sub>2</sub> gases in a fast atom beam etching chamber. The tapered pattern integrated on the backside of a light emitting diode produced a 21% improvement of the device efficiency. Although this technique seems interesting, the profiles still show a conical rather than triangular profile. The process also requires alternating two processes which in turn increases the complexity of the process and can lead to some

scalloping of the sidewalls which in turn increase scattering losses. Toyota and al. [Toyota 2001] reported excellent tapered features profiles in fused silica by using Chromium thin disks in a Reactive Ion Etcher (RIE). However their process is based on high fluorocarbon plasma and may not be suitable for III-V semiconductor materials.

In this work, we are using a soft mask erosion technique to control the grating profile in GaAs. This technique is based on the lateral erosion of the mask as the etching progresses and has been used to fabricate sharp tips in silicon with sidewalls slopes from  $52^\circ$  to  $78^\circ$  [Rakhshandehroo 1996] as well as sloped vias in GaAs [Westermann 2001]. We decided to use the process described in chapter 3 to transfer the SWG structure into the GaAs substrate. We found experimentally that a tapered structure could be obtained by simply varying the e-beam resist thickness and etching time without having to modify the process that proved to be successful in the transfer of the grating couplers. The goal of the process is to etch a narrow trench with a high aspect ratio while the resist mask is being eroded as shown in Fig.70. First, the pattern is written as a 30nm three pass line into a layer of ZEP520 using the Leica EBPG 5000+ with a current of 1nA and a voltage of 50kV. The dose used to clear a 450nm thick layer of resist is  $195\mu\text{C}/\text{cm}^2$ . The mask erosion produces the vertical sidewall profile observed during the transfer of the grating coupler by compensating for the bowing effect as explained in chapter 3. Then, as the mask is further eroded, an etch bias is developed and the sidewall profile in the semiconductor material follows the shape of the resist mask, producing the trapezoidal shape desired. As the etching process is continued further in time, a triangular shape can be obtained by removing the resist mask completely as shown in Fig.70. We found that a ZEP resist thickness of 250nm could

produce triangular profiles around 150nm deep while a 450nm thick resist produces 250nm deep gratings with shapes close to triangular for 71s etch time at an etching rate around 200nm/mn.

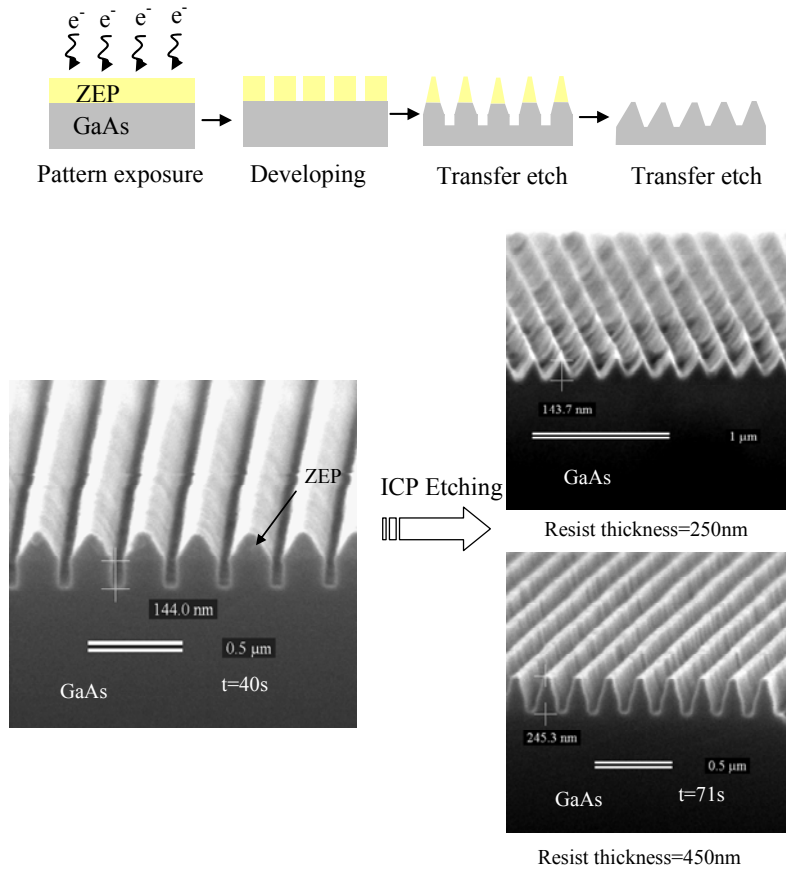


Fig.70: SEM pictures of tapered grating transfer in GaAs. The slope created by the mask erosion, shown after 40s of etching, is transferred into the substrate as the etching progresses to create the desired trapezoidal profile.

A SWG was fabricated using this process on the backside of a GCSEL such that the grating grooves are perpendicular to the grating coupler grooves and the electric field preferred polarization to obtain the lowest reflectivity. The grating coupler has a graded duty cycle for

which efficiency was shown to be close to 100% in chapter 4. The grating decay coefficient varies between 0 and  $100\text{cm}^{-1}$  for the first  $80\mu\text{m}$ . The antireflection grating was patterned in 450nm thick ZEP resist to obtain the profile shown in Fig.70. After developing the pattern in ZEP-RD for 90s and rinsed in isopropanol for 30s, the wafer was etched in a UNAXIS ICP etcher for 71s using the process described in chapter 3. The actual grating depth was measured to be around 225nm. The SWG reflectivity is estimated between 1% and 5% from the plots shown in Fig.68. The grating depth and profile may be finely adjusted in the future to improve this parameter.

### 5.3 Device performance

To evaluate the SWG performance, devices from the same wafer were fabricated with and without antireflection structure on the substrate. The  $60\mu\text{m}$  wide stripes devices were cleaved with a 2mm active and 0.8mm passive length, and then bonded p-side down on Aluminium Nitride submounts with a pre-deposited Au/Sn eutectic solder. They were tested under pulse condition with a  $1\mu\text{sec}$  current pulsewidth and repetition rate of 100kHz. Grating output light-current characteristics are presented in Fig.71. Slope efficiencies from GCSELs with n-side SWG were measured in the range of  $(0.81-0.83)W/A$ , corresponding to an external differential quantum efficiency of 65% that compares favorably to the best data previously reported for a grating-coupled semiconductor laser [Eriksson 1995]. Besides, the device presented in [Eriksson 1995] is based on a Bragg reflector grown in the substrate which increases the device resistance



and requires p-side up bonding, and is therefore not suitable for high power operation. Devices without SWG exhibited lower slope efficiencies around of 0.5W/A, the SWG being credited for a 64% improvement of the device efficiency.

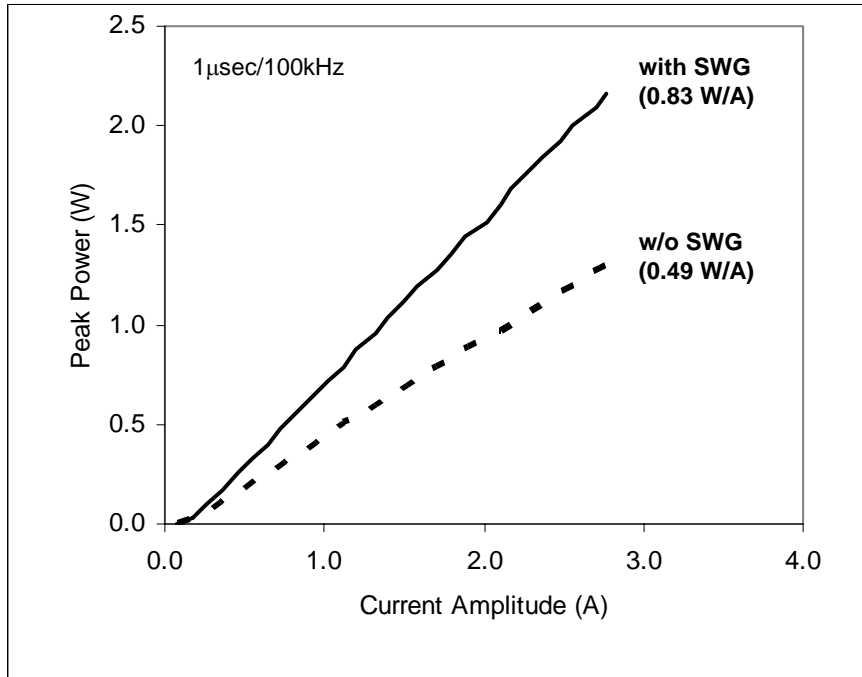


Fig.71: Light-current characteristics for GCSEL devices with and without antireflection subwavelength grating. The devices were tested with 1μs pulse current pulses at 100kHz repetition rate.

The effect of the reflectivity of the substrate can be estimated from an analysis similar to the one described in chapter 4. The power coming out of the device substrate can be estimated by

$$P_{out} = P_{FP} \cdot \eta_g \cdot \eta_i^p \cdot \eta_i^s \cdot \eta_i^m (1 - R_s) \cdot \left( \sum_{k=0}^{\infty} (\eta_i^{s^2} R_s R_m)^k \right) \quad (5.13)$$

where  $\eta_g$  is the grating efficiency estimated at 99% from the calculations in chapter IV,  $\eta_l^p$  and  $\eta_l^s$  account for losses in the passive region and substrate respectively,  $R_s$  and  $R_m$  are the substrate and superstrate reflectivities, and  $\eta_l^m$  accounts for the additional scattering losses generated by the non perfect high reflection coating. Given an internal quantum efficiency of 95% and internal losses of  $2.5\text{cm}^{-1}$  calculated from Fabry-Perot lasers as explained in chapter 4, one can estimate the maximum achievable grating output differential efficiency for our device to be 87% or  $P_{FP} = 1.1\text{W/A}$  in the case of low substrate reflectivity from (2.78). The absorption in the highly doped GaAs substrate was experimentally measured around 13% using wafers of different thicknesses, which proves that the obtained efficiency of 65% can be further enhanced by reducing the substrate loss, i.e. by lowering the substrate doping level. The SWG reflectivity is estimated at 5% using an SEM profile and Fig.68. Due to the low substrate reflectivity, the impact of multiple reflections is neglected. An output power of  $0.79\text{W/A}$ , in good agreement with experimental data, is found if we consider the HR coating on the grating generates 10% additional losses due to the non-planarized metal coating on submicron features as shown in Fig.39. This number is also consistent with experimental reflectivity data obtained by Evans for a grating coated with quarter wave dielectric and gold layer [Evans 1991]. In the case where the bare substrate has a high reflectivity of 0.32, the experimental data suggest that the substrate transmission coefficient alone cannot account for the difference in device efficiency. A possible explanation is that the device efficiency is affected by slightly higher feedback inside the cavity and additional heating which decreases  $P_{FP}$ . This argument is supported by an observed decrease

in lasing threshold of about 30% and the fact that reflected light from the substrate can be coupled back into the waveguide along the direction of propagation so that the impact of multiple reflections on the total output power is decreased. Following these arguments, a theoretical output power of 0.51W/A, in agreement with the experiment, is obtained when  $P_{FP}$  is decreased to 1W/A due to increased feedback and multiple reflections are neglected. More experimental data may be needed to confirm these assumptions and determine precisely the impact of the various variables on the device efficiency.

### **5.3 Fan-out element**

We described so far two optical elements that can be used to either shape the output beam for coupling purposes by focusing the beam above the substrate, or improve the device efficiency by decreasing the substrate reflectivity. We now describe the integration of a fan-out element on the device substrate to create multiple output beams from the device without affecting the overall efficiency. The integration of a fan-out element with a light source or amplifier is of interest for various applications including optical interconnects or multiple detector schemes [Wong 1993] as well as high power machining [Karlsson 2003]. The integration of a 4 by 4 fan-out on the substrate of a VCSEL was achieved by Martinsson et al. [Martinsson 1999]. For the in-plane semiconductor laser configuration, the integration of a fan-out has been achieved by the dislocation technique first proposed by Li [Feng 1998]. The technique was used by Eriksson [Eriksson 1997] in an unstable resonator configuration but feedback created by the DOE inside

the cavity distorted the output beam profile. Also the uniform duty cycle of the grating coupler created skewed spot intensity profiles due to exponential decay of the intensity during interaction with the grating. A new fan-out phase function design calculating the contribution of each grating to the reflected and diffracted waves was recently proposed by Modh [Modh 2003] to prevent feedback inside the laser cavity. Modh obtained diffraction-limited spots, however the new design is responsible for a 40% drop in external differential quantum efficiency at 975nm when compared to devices with a grating outcoupler only. In Feng and Li's work [Feng 1999], the fan-out was integrated with a grating coupler at the end of a master-oscillator power amplifier. This approach showed significant improvement of the spot profile by placing the beam-shaping function outside of the resonator but the efficiency remained low with “considerably lower output power than predicted” reported by the authors. The cause of the efficiency drop in both cases is not fully understood at this point but is likely related to the combination of the grating coupler and beam-shaping functions into a same DOE.

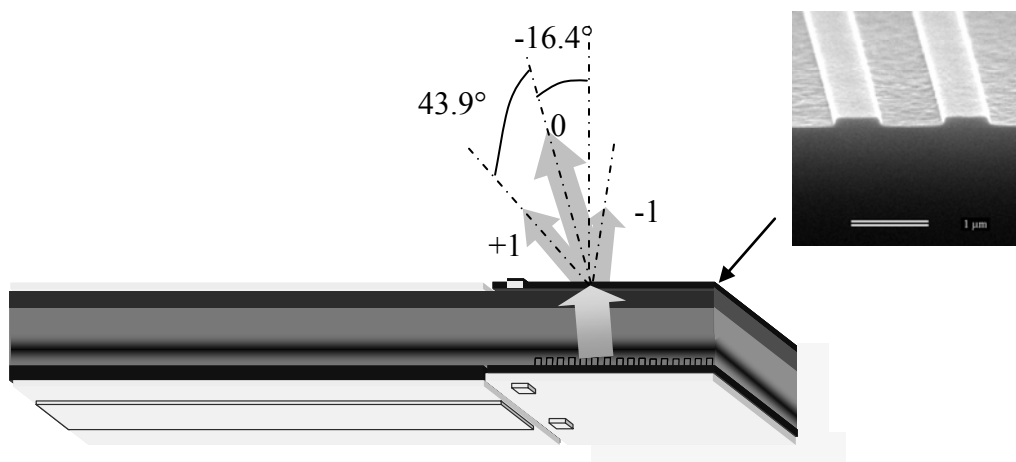


Fig.72: Diagram of the fan-out integration on the backside of a GCSEL. The fan-out element is a  $1.4 \mu\text{m}$  period grating etched in GaAs at a depth of 105nm. An SEM profile of the fabricated

grating is shown in the inset.

In this work, we integrate a fan-out grating on the backside of a GCSEL to decouple outcoupling and splitting functions as shown in Fig.72. The grooves of the grating are parallel to the contact stripe. Although complex fan-out functions may be integrated on the device substrate, the multiple spatial transverse modes created by the broad stripe device as well as the several longitudinal modes would severely distort the spot profiles unless a different contact stripe configuration such as master-oscillator power amplifier (MOPA) geometry is implemented [Feng 1999]. We therefore decided to demonstrate a splitting function using a simple  $1.4 \mu\text{m}$  grating designed to split the output beam into three distinct orders, the +1 and -1 orders being diffracted at  $43.9$  degrees off-normal for a wavelength of  $970\text{nm}$ .

### 5.3.1 Design and fabrication

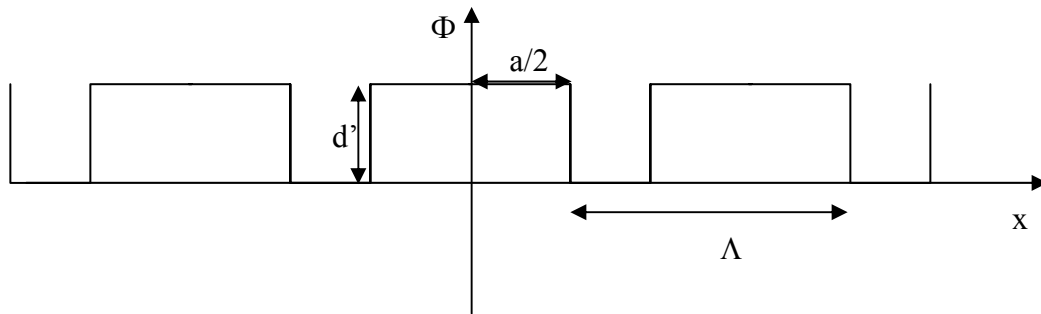


Fig.73: Phase profile introduced by the fan-out element.

The grating period of  $1.4 \mu\text{m}$  is chosen so that only three orders are diffracted in the air. The

phase of the relief grating shown in Fig.73 can be expressed as

$$T(x) = \left[ \text{rect}\left(\frac{x}{a}\right) e^{j\phi} + \text{rect}\left(\frac{x - \frac{\Lambda}{2}}{\Lambda - a}\right) \right] * \sum_{k=-\infty}^{\infty} \delta(x - k\Lambda) \quad (5.14)$$

The phase difference  $\Phi$  is given by

$$\phi = \frac{2\pi}{\lambda} d (n_s - 1) = \frac{2\pi}{\lambda} \frac{d}{\cos\theta_i} (n_s - 1) \quad (5.15)$$

where  $n_s$  is the GaAs substrate index of 3.54 at 970nm wavelength,  $d$  is the grating thickness, and  $\theta_i$  is the incident angle inside GaAs. In the far-field, assuming a plane wave impinging on the grating, the intensity profile of the diffracted wave is given by

$$I(\nu) = \left| \int_{-\infty}^{\infty} T(x) e^{-j \frac{2\pi x \nu}{\lambda}} dx \right|^2 \quad (5.16)$$

where  $\nu = \frac{\theta}{\lambda}$  is the spatial frequency and  $\theta$  is the far field angle. The far-field intensity profile

is then given by

$$\left\{ \begin{array}{l} I(\nu) = \left| \frac{e^{j\phi} \sin(a\pi\nu) + e^{-j\nu\frac{\Lambda}{2}} \sin((\Lambda - a)\pi\nu)}{\Lambda\pi\nu} \right|^2 \\ \nu = \frac{n}{\Lambda}, n \in Z \end{array} \right. \quad (5.17)$$

We assume that light is diffracted in the plane perpendicular to the grating. However the depth of the grating is corrected for the incident angle inside the GaAs material of  $4.5^\circ$ . The calculated ratio of power diffracted into the +1 or -1 order and power diffracted into the  $0^{\text{th}}$  order is shown in. Due to the high index of GaAs around 970nm wavelength, the phase profile strongly depends on the grating depth. A 10nm difference in grating depth around 100nm produces a 40% difference of the power ratio between 0 and +1 order for a 50% grating duty cycle. The tolerance on the grating parameters is therefore low and rigorous coupled wave analysis may be required to predict the element performance accurately [Moharam 1995].

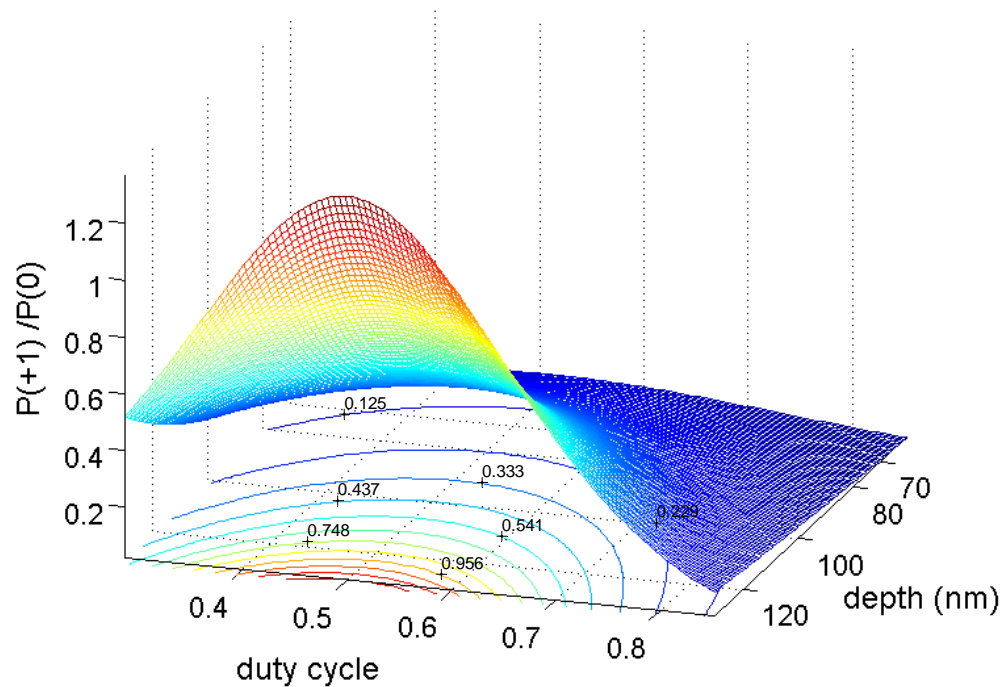


Fig.74: Diffracted power ratio between +1 and zero<sup>th</sup> order. The depth is corrected by the angle of incidence in the substrate of  $4.5^\circ$ . The calculation is based on scalar theory for a  $1.4\mu\text{m}$  rectangular grating and 970nm emission wavelength.

The grating was fabricated by patterning the fan-out element in 450nm of ZEP using a dose of  $100\mu\text{C}/\text{cm}^2$ . The grating on the n-side was aligned to the p-contact stripe using gold alignment marks produced by lift-off using front to back alignment. The pattern was developed for 90 s in ZEP-RD and rinsed in IPA for 30s. Then the pattern was transferred into GaAs in an ICP etcher using the process described in chapter 3 for 19s. A depth around 105nm and a duty cycle of 0.58 were measured. No anti-reflection coating was applied on the fan-out element. The grating coupler on the p-side had a graded duty cycle and was covered with a high reflection coating. The slope efficiency of similar devices from the same wafer without fan-out element antireflection coating on the substrate was around 0.51W/A in QCW operation.

### 5.3.2 Performance

The power in the 0th order was measured around three times higher than the power measured in the +1 and -1 order. The scalar theory predicts a ratio around 2.5 for the grating profile measured. The discrepancy may be explained by the limitations of the scalar theory for large diffraction angles and small feature to wavelength ratio [Pommet 1994]. The total output power from the three orders is 0.54W/A, a value similar to the power obtained in the same pumping conditions from a reference device without fan-out element. The integration of the beam-splitting element therefore does not affect the efficiency of the device, unlike the other methods involving grating coupler dislocation. The angle of divergence between the 0<sup>th</sup> and +1 order was measured by measuring the distance between the two intensity peaks of the two spots at a distance of



1.36cm and 2.36cm above the device. The angle obtained is  $43.3^{\circ} \pm 0.8^{\circ}$ , in good agreement with the predicted angle. The tolerance on the angle measurement comes from the difficulty in locating the intensity peak of the +1 or -1 order due to the large angle projection on the plane of the image.

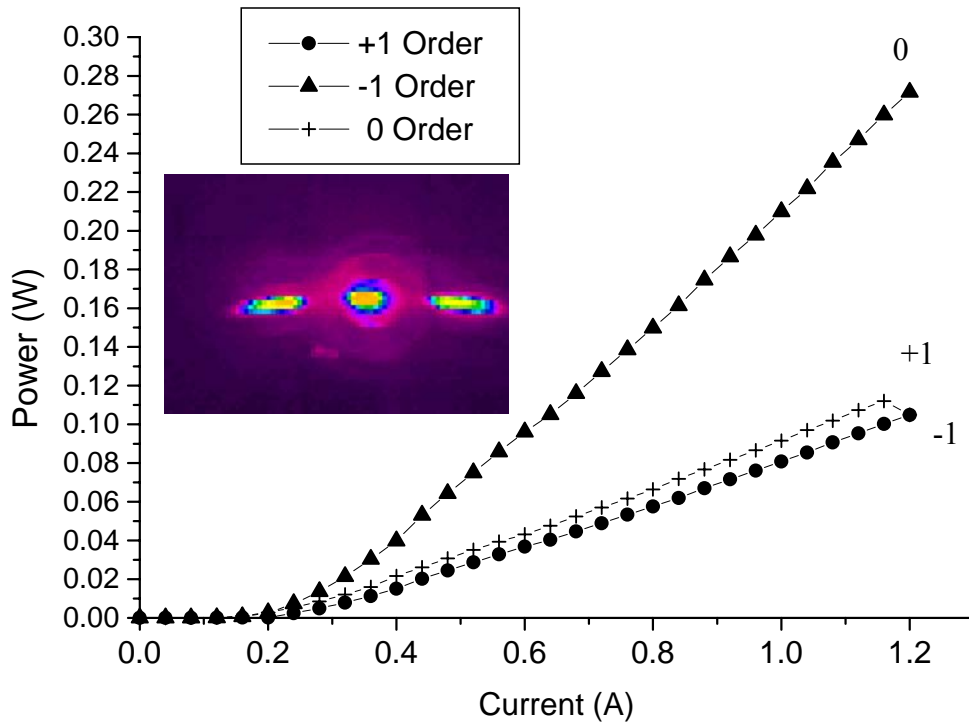


Fig.75: L-I curve for the three diffracted spots. The device was tested with a 500ns pulse at a 1kHz repetition rate. The intensity profile shown in inset was captured 1.36cm above the substrate by imaging a diffuser. The +1 and -1 order spots appear distorted due to the large divergence angle projection.

## CHAPTER 6: CONCLUSIONS

### **6.1 Summary of the contributions presented in this dissertation**

We presented the monolithic integration of dual optical elements on a broad area semiconductor laser diode for high power applications around 980nm wavelength. The device's novelty is based on the combination of a low reflectivity second order detuned grating coupler integrated close to the quantum well while the second optical elements is integrated on the GaAs substrate. The main contributions presented in this dissertation are summarized in this section.

#### **6.1.1 High efficiency grating coupler with low effective reflectivity**

The AlGaAs/GaAs waveguide structure of the device was successfully designed in collaboration with Coherent Inc. to maximize coupling by the grating while minimizing the reflectivity between active and passive regions. The patterning of 270nm period gratings by electron beam lithography was characterized to control the grating coupler duty cycle using dose exposure variation. The etching process, developed in collaboration with Unaxis Inc., was characterized for sub-micron features. A significant improvement of the device near-field intensity profile along the contact stripe was obtained by varying the grating duty cycle from 20 % to 55%. The

best grating couplers showed efficiency evaluated as close to 100% and reflectivity lower than  $5 \cdot 10^{-4}$ . They were obtained by grading the duty cycle to minimize impedance mismatch between active and grating region and by using a ZEP soft mask resist to obtain rectangular profiles in AlGaAs.

We also demonstrated the low reflectivity grating coupler can be used to suppress feedback inside the cavity and obtain superluminescent emission when both cleaved facets are replaced by grating couplers. Output power in excess of 1.5W CW with 11nm bandwidth FWHM spectrum was obtained by measuring the device's crossed outputs where they overlap, a few mm above the substrate. Peak power in excess of 30W without visible COMD was obtained in this case. The device optical and spectral characteristics were found consistent with those of a standard superluminescent diode. In both cases, the grating coupler was coated by a high reflection coating combining dielectric and gold layers.

### **6.1.2 Device performance improvement using backside optical element**

The integration of an optical element on the device GaAs substrate was performed to achieve three different optical functions, taking full advantage of the collimating and circularizing functions of the grating coupler. A front-to-back photolithography process was developed to enable the second optical element integration on the substrate in open windows above the grating coupler, including lift-off of the n-type ohmic contact and alignment marks.

First a 40 level refractive lens was successfully integrated using focused ion beam direct milling.

The lens has a 1mm focal length and showed a twofold reduction of the FWHM output intensity profile at the focal point. However, the quality of lens focusing is limited by several factors, particularly the poor transverse spatial beam profile as well as large aberrations created by the additive milling process.

Then we showed that the device output power can be increased by integrating a subwavelength grating (SWG) on the substrate to act as an antireflection structure. The low reflectivity tapered structure was obtained by a mask erosion technique which enables the fabrication of trapezoidal gratings in a single etching step. The SWG integration was responsible for a 64% improvement of the device external differential quantum efficiency (DQE) when compared to devices with bare GaAs substrates. DQEs of 65% were measured with 1 $\mu$ s pulse width at 100kHz repetition rate. To the author's knowledge, this is the highest efficiency reported for a grating-coupled device.

Finally, a beam splitter was integrated on the device substrate by etching a 1.5 $\mu$ m grating at a depth of 105nm onto the GaAs substrate. The +1 and -1 diffracted orders are emitted at around 44 degrees off normal. Unlike other techniques based on dislocation of the grating coupler, the integration of the beam splitting element did not cause any observable drop of the device efficiency. This result is a direct benefit of decoupling the outcoupling and beam-shaping functions into two different, but monolithically integrated, optical elements. This feature demonstrates the high potential of this configuration to fabricate highly integrated and versatile semiconductor devices for high power applications.

### 6.1.3 Numerical modeling and analysis

A detailed analysis of the losses involved in extracting light by the grating coupler through the substrate was presented. We showed that the power-dependent losses in the passive region are on the order of 3 to 5  $\text{cm}^{-1}$ , while the absorption in the heavily-doped substrate is on the order of 9  $\text{cm}^{-1}$ . The grating efficiency improvement obtained during the development of the fabrication process was demonstrated using the losses analysis. The aspect ratio dependence of the etching for sub-micron features was characterized and taken into account to model accurately the effect of varying the grating parameters on the near-field profile using finite-difference time-domain technique. The FDTD model also predicted losses would be 28% higher if gold was deposited directly into the grating's grooves without a dielectric buffer layer.

A self-consistent model of the semiconductor active region was implemented to explain the effect of the broad area contact stripe and low reflectivity grating on the output spatial mode profile and optical intensity distribution. The nonuniform optical intensity distribution along the stripe predicted by the model explains the increase in COMD level of the grating-coupled device versus standard Fabry-Perot observed experimentally. A peak power of 22W was obtained from a 60 $\mu\text{m}$  wide, 2mm long device with a cleaved back-facet mirror left uncoated. The model also predicts the apparition of ripples on the top of the transverse beam profile, resulting from nonlinearities triggered by the antiguiding factor and multiple spatial modes excited inside the wide stripe cavity.

#### **6.1.4 Device applications**

The devices presented in this dissertation can be used in various applications where semiconductor lasers or amplifiers are of interest. The large surface emitting area increasing the COMD level and low divergence beam with beam-forming capability are a powerful combination that should be appreciated in high power applications for pump diodes or free-space optical communication sources. Besides, p-side down configuration is suitable for efficient cooling during CW operation. The low reflectivity feature of the device also makes it an attractive candidate for external cavity configuration where feedback is provided by an external mirror. The high performance of the devices shown in this work is expected to have a very positive impact on such applications as compact modelocked semiconductor laser [Kim 2004] or broadly tunable laser source [Jiang 1999]. Finally the broad spectrum generated by the X-SLD device should be of interest as a superluminescent diode. This configuration also constitutes a potentially very good and compact semiconductor gain block [Kim 2004] by providing ultra-low facet reflectivity not easily achieved by standard dielectric coating and high signal to noise ratio provided by the spatial dispersion of the grating coupler that separates the amplified signal from the spontaneous emission spectrum [Carlson 1992, Zhang 2004].

#### **6.2 Future perspectives**

The performance of the semiconductor presented in this work could be further improved and understood by following these suggested research paths.

### **6.2.1 Efficiency**

We showed in chapter 4 and 5 that the main factor limiting the device's efficiency is the absorption in the GaAs substrate. We believe it is possible to improve the performance further by lowering the doping level and decrease the free-carrier absorption coefficient. An improvement on the order of 10% can be expected. The reduction of the losses in the passive region by quantum well intermixing does not seem necessary if the device is pumped at high current.

The integration of the subwavelength grating on the substrate demonstrated the importance of decreasing the substrate reflectivity to obtain high efficiency. We believe the fabricated structure reflectivity can be lowered further by fabricating slightly deeper triangular structures. This task is particularly important for superluminescent diodes and optical amplifiers applications to avoid the ripples observed on the emission spectrum caused by multiple reflections in the substrate.

### **6.2.2 Brightness**

The device brightness is severely limited by the filaments formed inside the broad stripe active region. To solve this problem, one should leverage off the great deal of research that has aimed at maintaining single spatial transverse mode in high power semiconductor lasers over the past several years [Luo 2000, Eriksson 2001]. Flared configurations already showed they are capable of producing a diffraction-limited beam with more than 5W optical power in pulsed conditions [Mehuys 1994]. In such geometry, the forward wave can propagate according to

diffraction law inside the material, while the backward wave is not guided inside the active region. Such a structure was modeled using the self-consistent model presented in chapter 2. A significant improvement is found at 1A pumping current in pulse conditions (thermal effects neglected). However, the grating coupler will have to be curved to collimate the diverging wavefront of the propagating wave. Note that the far-field intensity profile has not been corrected for possible collimation of the beam. Convergence is obtained after 7 loops, unlike broad stripe case.

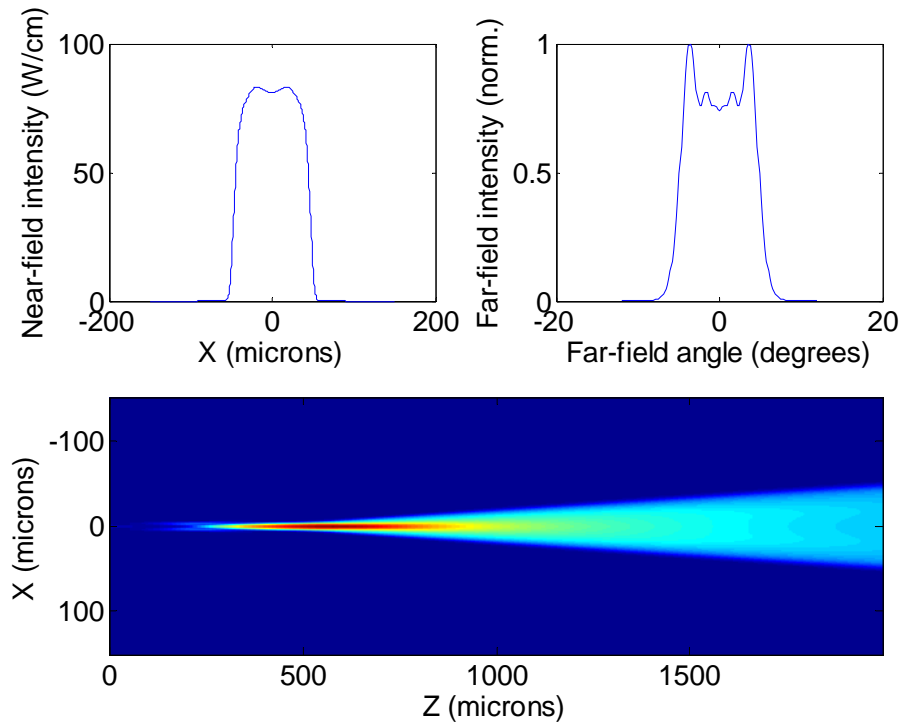


Fig.76: Optical intensity distribution under flared contact stripe for 1A pumping current. The structure consists of a 10 $\mu$ m wide, 500  $\mu$ m long rectangular stripe followed by a 1.5mm long flared stripe corresponding to a 3.43 degrees taper angle.



In the direction parallel to the stripe, a more symmetric near-field intensity profile than the one showed in chapter 4 could be obtained by varying the grating parameters on a longer distance than  $80\mu\text{m}$ . Assuming no aspect ratio dependent etching, Kipfer derived an analytic formula of the duty cycle variation needed to obtain a Gaussian intensity profile output of width  $\sigma$  [Kipfer 2001].

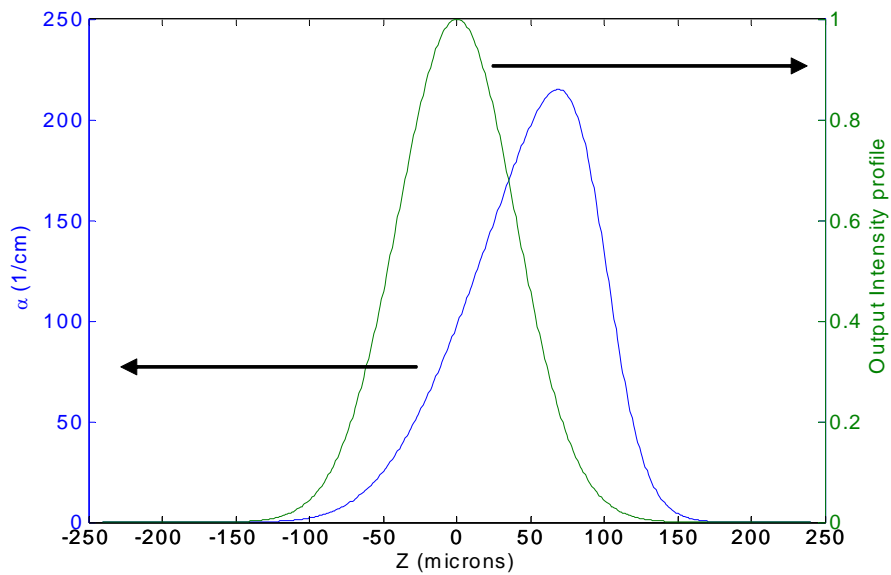


Fig.77: Plot of leakage rate versus distance and corresponding  $100\mu\text{m}$  width Gaussian output intensity profile.

Kipfer's formula, expressed as a function of the leakage rate to include the dependence of feature depth versus width shown in chapter 3, is given by

$$\alpha(z) = \sqrt{\frac{2}{\pi}} \frac{e\left(-\frac{2z^2}{\sigma^2}\right)}{\sigma \cdot \left(1 + \operatorname{erf}\left(\frac{\sqrt{2}}{\sigma} z\right)\right)} \quad (6.1)$$

where  $\operatorname{erf}(z) = \frac{2}{\sqrt{\pi}} \int_0^z e^{-t^2} dt$ . A plot of the coupling coefficient variation and corresponding output intensity profile is shown in Fig.77.

### 6.3 Backside micro-optical elements

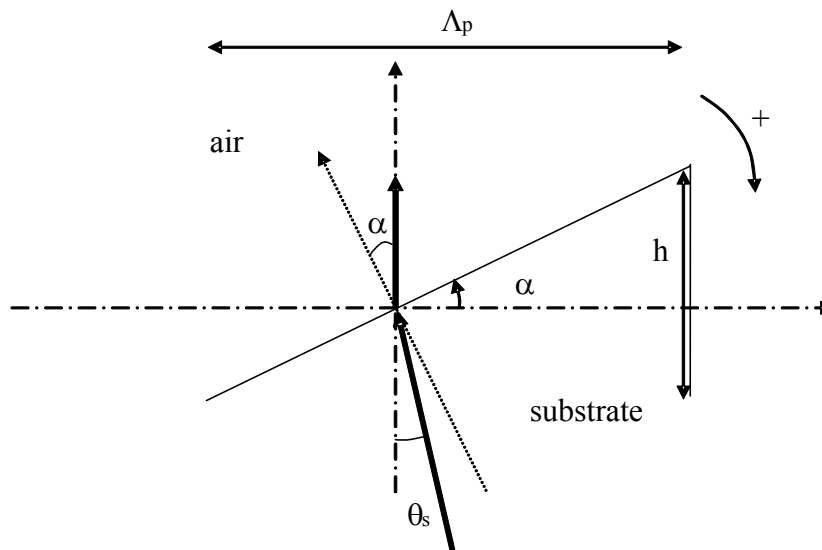


Fig.78: Prism angle needed to obtain vertical emission from the substrate.

A wavelength selective element such as a distributed Bragg reflector may be needed to obtain a

stable monochromatic output. In that case, many more functions can be integrated on the device substrate using diffractive optical elements, to form 2D spot array generators or vortex elements for example. The off-axis diffraction angle caused by the detuning of the second order grating coupler may be corrected using a phase function such as a prism on the device substrate. The angle of diffraction of light  $\theta_s$  in the GaAs substrate for the first order is given by

$$\sin \theta_s = \frac{n_{eff} - \frac{\lambda}{\Lambda}}{n_s} \quad (6.2)$$

where  $n_s$  is the substrate index of refraction,  $\Lambda$  the grating period, and  $\lambda$  the wavelength in vacuum. If  $\alpha$  is the prism angle (Fig.78), then the angle of diffraction in the air  $\theta_a$  must satisfy the equation

$$\sin(\alpha) = n_s \cdot \sin(\alpha - \theta_s) \quad (6.3)$$

Given the following parameters:  $\Lambda = 270\text{nm}$ ,  $\lambda = 980\text{nm}$ ,  $n_s = 3.52$ ,  $n_{eff} = 3.3$ , we get  $\alpha_p = -0.1374$  radians. In the case where the device is used as an optical amplifier, the prism angle can also be used in conjunction with a superimposed diffraction grating to fabricate an achromatic coupler [Spaulding 1991] that will correct the spatial dispersion introduced by the grating coupler for a bandwidth up to 10nm.

## **APPENDIX A: FDTD NUMERICAL FORMULAE**

Although a complete detailed analysis of the FDTD algorithm can be found elsewhere [Taflove 2000], we present here the equation used in the finite-difference time domain model of the grating structure to explain how the equations are implemented in our model. The symbols used in the derivation are defined below

J	Electric current Density (Amperes/meter <sup>2</sup> )
E	Electric field (Volts/meter)
H	Magnetic field (Amperes/meter)
D	electric flux density (coulombs/ meter <sup>2</sup> )
B	magnetic flux density (webers/meter <sup>2</sup> )
$\epsilon$	electrical permittivity (farads/meter)
$\epsilon_r$	relative permittivity
$\epsilon_0$	free-space permittivity ( $8.854 \times 10^{-12}$ farads/meter)
$\mu$	magnetic permittivity (henrys/meter)
$\mu_r$	relative permeability
$\mu_0$	free-space permeability ( $4\pi \times 10^{-7}$ henrys/meter)
$\sigma$	electric conductivity (siemens/meter)
$\sigma^*$	equivalent magnetic loss (ohm/meter)
C	Light velocity in vacuum (299,792,458 m/s)

The well-known general Maxwell's equations in time-domain may be written

$$\begin{cases} \varepsilon \frac{\partial \mathbf{E}}{\partial t} = \nabla \times \mathbf{H} - \mathbf{J} \\ \frac{\partial \mathbf{H}}{\partial t} = -\frac{1}{\mu_0} \nabla \times \mathbf{E} \end{cases} \quad (\text{A.1})$$

where

$$\mathbf{J} = \sigma \mathbf{E} \quad (\text{A.2})$$

And therefore one gets

$$\begin{cases} \varepsilon \frac{\partial \mathbf{E}}{\partial t} = \nabla \times \mathbf{H} - \sigma \mathbf{E} \\ \frac{\partial \mathbf{H}}{\partial t} = -\frac{1}{\mu_0} \nabla \times \mathbf{E} \end{cases} \quad (\text{A.3})$$

We will show next how the electric field is computed numerically from these coupled equations using approximate expressions of the derivative forms.

- E field derivation

We restrict the analysis to TE polarization and derive the equations used in the model for completeness.

$$\varepsilon \frac{\partial E_y}{\partial t} = \left( \frac{\partial H_x}{\partial z} - \frac{\partial H_z}{\partial x} \right) - \sigma E_y \quad (\text{A.4})$$

Using the approximations

$$\frac{\partial E_y}{\partial t} \cong \frac{E_y(t + \Delta t) - E_y(t)}{\Delta t} \quad (\text{A.5})$$

$$E_y \cong \frac{E_y(t + \Delta t) + E_y(t)}{2} \quad (\text{A.6})$$

and

$$\left\{ \begin{array}{l} \frac{\partial H_z}{\partial x} \cong \frac{H_z\left(x + \frac{\Delta x}{2}\right) - H_z\left(x - \frac{\Delta x}{2}\right)}{\Delta x} \\ \frac{\partial H_x}{\partial z} \cong \frac{H_x\left(z + \frac{\Delta z}{2}\right) - H_x\left(z - \frac{\Delta z}{2}\right)}{\Delta z} \end{array} \right. \quad (\text{A.7})$$

Using a uniform mesh  $\Delta x = \Delta z = \Delta r$ , taken to be 10nm in our case, one obtains

$$E_y(t + \Delta t) + \frac{\alpha \Delta}{2\varepsilon} E_y(t + \Delta t) = E_y(t) + \frac{\Delta}{\varepsilon} \left( \frac{-H_z\left(x + \frac{\Delta x}{2}\right) + H_z\left(x - \frac{\Delta x}{2}\right) + H_x\left(z + \frac{\Delta z}{2}\right) - H_x\left(z - \frac{\Delta z}{2}\right)}{\Delta r} \right) - \frac{\alpha \Delta}{2\varepsilon} E_y(t) \quad (\text{A.8})$$

The E field can be normalized to simplify the equations using the following expressions

$$\tilde{E} = \sqrt{\frac{\varepsilon_0}{\mu_0}} \bar{E} = \frac{1}{\eta_0} \bar{E} \quad (\text{A.9})$$

Equation (A.8) can then be rewritten as

$$\tilde{E}_y(t + \Delta t) = C^{Ey} \tilde{E}_y(t) + C^H \left( -H_z\left(x + \frac{\Delta x}{2}\right) + H_z\left(x - \frac{\Delta x}{2}\right) + H_x\left(z + \frac{\Delta z}{2}\right) - H_x\left(z - \frac{\Delta z}{2}\right) \right) \quad (\text{A.10})$$

with

$$\left\{ \begin{array}{l} C^{Ey} = \frac{\left(1 - \frac{\sigma\Delta t}{2\varepsilon_r\varepsilon_0}\right)}{\left(1 + \frac{\sigma\Delta t}{2\varepsilon_r\varepsilon_0}\right)} \\ C^H = \frac{\Delta t}{\varepsilon_r\sqrt{\varepsilon_0\mu_0}\Delta r\left(1 + \frac{\sigma\Delta t}{2\varepsilon_r\varepsilon_0}\right)} \stackrel{\text{stability factor}}{=} \frac{1}{2\varepsilon_r\left(1 + \frac{\sigma\Delta t}{2\varepsilon_r\varepsilon_0}\right)} \end{array} \right. \quad (\text{A.11})$$

using the stability factor

$$S = \frac{\Delta t}{\Delta r\sqrt{\varepsilon_0\mu_0}} = \frac{C\Delta t}{\Delta r} = 0.5 \quad (\text{A.12})$$

It can be shown that  $S \leq 1$  provides a stable solution of the numerical solution.

- H field derivation

Since the FDTD scheme is a full-vectorial solution of the electromagnetic problem, both electric and magnetic fields are solved simultaneously. We start from the time-domain equation

$$\frac{\partial \mathbf{H}}{\partial t} = -\frac{1}{\mu_0} \nabla \times \mathbf{E} \quad (\text{A.13})$$

Using the approximation

$$\frac{\partial H_x}{\partial t} \cong \frac{H_x(t + \Delta t) - H_x(t)}{\Delta t} \quad (\text{A.14})$$



and

$$\begin{cases} \frac{\partial E_y}{\partial x} \cong \frac{E_y\left(x + \frac{\Delta x}{2}\right) - E_y\left(x - \frac{\Delta x}{2}\right)}{\Delta x} \\ \frac{\partial E_y}{\partial z} \cong \frac{E_y\left(z + \frac{\Delta z}{2}\right) - E_y\left(z - \frac{\Delta z}{2}\right)}{\Delta z} \end{cases} \quad (\text{A.15})$$

one obtains

$$\begin{cases} H_x(t + \Delta t) = H_x(t) + \frac{\Delta t}{\sqrt{\varepsilon_0 \mu_0}} \frac{\tilde{E}_y\left(z + \frac{\Delta z}{2}\right) - \tilde{E}_y\left(z - \frac{\Delta z}{2}\right)}{\Delta z} \\ H_z(t + \Delta t) = H_z(t) - \frac{\Delta t}{\sqrt{\varepsilon_0 \mu_0}} \frac{\tilde{E}_y\left(x + \frac{\Delta x}{2}\right) - \tilde{E}_y\left(x - \frac{\Delta x}{2}\right)}{\Delta x} \end{cases} \quad (\text{A.16})$$

using the normalized electric field given in (A.9). Using the standard stability relationship for  $S=0.5$ , the resulting equations for the magnetic field are

$$\begin{cases} H_x(t + \Delta t) = H_x(t) + \frac{\tilde{E}_y\left(z + \frac{\Delta z}{2}\right) - \tilde{E}_y\left(z - \frac{\Delta z}{2}\right)}{2} \\ H_z(t + \Delta t) = H_z(t) - \frac{\tilde{E}_y\left(x + \frac{\Delta x}{2}\right) - \tilde{E}_y\left(x - \frac{\Delta x}{2}\right)}{2} \end{cases} \quad (\text{A.17})$$

## **APPENDIX B: TESTING SET-UP**

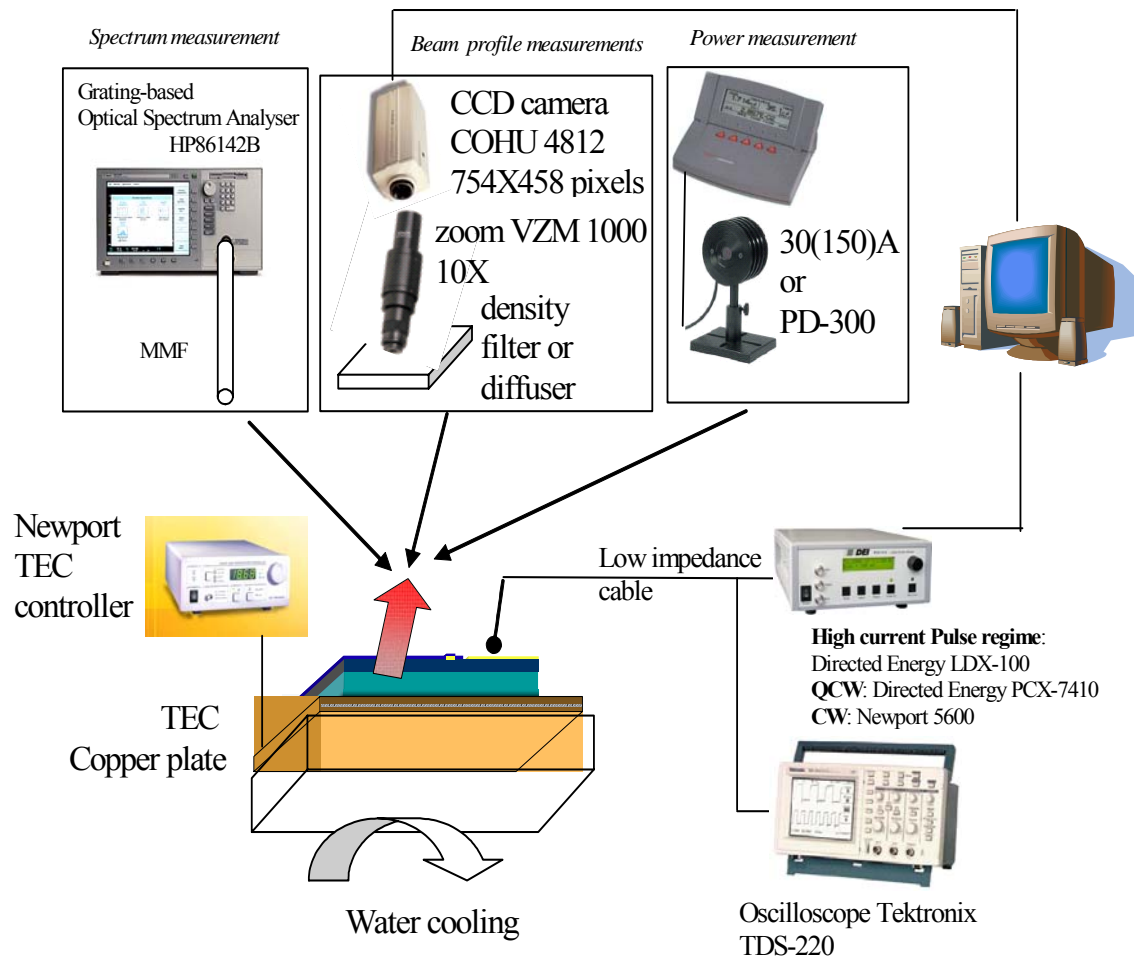


Fig.79: Diagram of testing set-up. The output from the surface-emitting device is captured for spectral, power, and spatial beam profile measurements.

## LIST OF REFERENCES

Afromowitz M.A. , Solid State Comm., Vol. 15, p. 59, 1974.

Agrawal G.P., J. Appl. Phys. Vol. 56, 11, pp. 3100-3109, 1984.

Agrawal G. P. and N. K. Dutta, *Semiconductor lasers*, 2<sup>nd</sup> edition. Kluwer Academic Publishers, 1993.

Al-Muhanna A., Mawst L. J., Botez D., Garbuzov D. Z., Martinelli R. U., and Connolly J. C., Appl. Phys. Lett., Vol. 73, p. 1182, 1998.

Alferov et al., Fiz. Tech. Poluprovod, 4, 832, 1974.

Basov N. G., Krokhin O.N., and Popov Y.M., Soviet Physics, JETP, 13, 1320, 1961.

Bates K. A., Li L., Roncone R. L., and Burke J. J., Appl. Opt., Vol. 32, p. 2112, 1993.

Berenger J.P., J. Comput. Phys., Vol. 114, p. 185, 1994.

Bernard C.G., Endeavour, Vol.26, p.79, 1967.

Bedford R., Luo H., and Fallahi M., IEEE Photon. Techn. Lett. Vol. 12, 8, 2000.

Bedford R., Fallahi M., IEEE J. of Quant. Electron. Vol. 38, p.716, 2002.

Bernard M. G. and Duraffourg G., Phys. Status Solidi, 1, 699, 1961.

Born M. and Wolf E., *Principles of Optics*, Sixth edition, Cambridge University Press, 1980.

Broberg B. and Lindgren S., J. Appl. Phys. Vol. 55, 9, pp. 3376-3381, 1984.

Burnham R., Scifres D., and Streifer W., IEEE J. Quant. Electron., Vol. 11, p. 439, (1975).

Causa, F., Sarma, J., and Balasubramanyam, R., IEEE transactions on electron devices, Vol. 46, 6, p. 1135, 1999.

Carlson N.W., Abeles J.H., Bour D.P., Liew S., and Reichert W.F., IEEE Photon. Techn. Lett. Vol. 2, p.708, 1990.

Carlson, N.W., IEEE J. of Quant. Electron., Vol.28 p. 1884, 1992.

Clapham P.B. and Hutley M.C., Nature, Vol. 244, p.281, 1973.

Cooperman S.S., Choi H.K., Sawin H.H., and D.F. Kolesar, J. Vac. Sci. Technol. B Vol. 7, p. 41, 1988.

Dai Z., Michalzik R., Unger P., and Ebeling K. J., IEEE J. of Quant. Elect., Vol. 33, 12, p. 2240, 1997.

Delepine S., Gerard F., Pinquier A., Pasquier J., Locatelli D., Chardon J.P., Bissessur H. K., Touche N., Boubal F. R., and Salet P., IEEE J. of Select. Topics in Quant. Elec. Vol. 7, 2, p. 111, 2002.

Du G., Xu C., Liu Y., Zhao Y., and Wang H., IEEE J. of Quant. Electron., Vol. 39, p.149, 2003.

Erdogan T. and Sipe J.E., J. of Opt. Soc. Am. A, Vol. 13, p. 296, 1996.

Eriksson N., Hagberg M., and Larsson A., IEEE Photon. Tech. Lett., Vol. 7, 12, p. 1394, 1995.

Eriksson N., Hagberg M., and Larsson A., J. Vac. Sc1. Technol. B Vol. 14, p. 184 (1996).

Eriksson N., Larsson A., Uemukai M, and Suhara T., IEEE J. of Quant. Elec., Vol. 34, p. 1095, 1998.

Eriksson N., Bengtsson J., Li M., Modh P., and Larsson A., IEEE photonics technology letters, Vol. 9, p. 1570, 1997.

Eriksson N., Modh P., and Larsson A, IEEE J. of Quant. Elec., Vol. 37, p. 1095, 2001.

Evans G.A., Bour D.P., Carlson N.W., Amantea R., Hammer J.M., Lee H., Lurie M., Lai R.C., Pelka P.F., Farkas R.E., Kirk J.B., Liew S.K., Reichert W.F., Wang C.A., Choi H.K., Walpole J.N., Butler J.K., Jr Ferguson W.F., DeFreez R.K., and Felisky M., IEEE J. of Quantum Electron.

Vol. 27, p. 1594, 1989.

Evans G.A., Bour D.P., Carlson N.W., Amantea R., Hammer J.M., Lee H., Lurie M., Lai R.C., Pelka P.F., Farkas R.E., Kirk J.B., Liew S.K., Reichert W.F., Wang C.A., Choi H.K., Walpole J.N., Butler J.K., Ferguson W.F. Jr., DeFreez R.K., and Felisky M., IEEE J. of Quant. Electron., Vol. 27, p. 1594, 1991.

Evans G.A., Nils W. Carlson, and J. M. Hammer, Surface-emitting semiconductor laser and arrays, Chapter 4 p.119-21, 1993.

Feng Y., Li M., Chow-Chong P., Marshall P., Eskin S., and Davies M., IEEE Photonics Technology Letters, Vol. 10, No.12, pp. 1682-1684, 1998.

Fu Y., Bryan N.K.A., and Shing O.N., IEEE Photon. Technol. Lett. Vol. 12, 9, p. 1213, 2000.

Fu Y. and Bryan N. K. A., IEEE Trans. on Semicond. Manufact. Vol. 15, p. 2, 2002.

Fukuda M., *Reliability and degradation of semiconductor lasers and LEDs*, Chap. 4, Boston MA, Artech House, 1991.

Fukuda M., Okayasu M., Temmyo J., and Nakano J., IEEE J. of Quantum Electron., Vol.30, 2, pp. 471-476, 1994.

Gottscho R.A., Jurgensen C. W., and Vitkavage D. J., J. Vac. Sc1. Technol. B Vol. 10, p. 2133, (1992).

Grann E.B., Moharam M.G., and Pommet D., J. Opt. Soc. Am. Vol. 11, p. 2695, 1994.

Hagberg M., Eriksson N., Kjellberg T., and Larsson A., Opt. Lett., Vol. 20, p.180, 1995(a).

Hagberg M., Eriksson N., Kjellberg T., and Larsson A., Microelec. Eng. Vol. 27, p. 435, 1995(b).

Hagberg M., Jonsson B., and Larsson A., J. Vac. Sci. Technol. B, Vol. 12, p. 555, 1993.

Hagberg M., Eriksson N., Larsson A., IEEE J. of Quant. Electron., Vol. 32, , p.1596, 1996.

Hedlund C., Blom H.O., and Berg S., J. Vac. Sci. Technol. A Vol. 12, p. 1962, 1994

Higuchi M., J. of Electroch. Soc., Vol. 136, p. 2710, 1989.

Jiang J., Smoski O., Roychoudhuri C., Portnoi E., Venus G., Gadjiev I., and McKillop J., “Broad tunability of grating surface emitting laser with external cavity”, Electron. Lett., vol. 35, pp. 1847-1848, 1999.

Kanamori Y., Ishimori M., and Hane K., IEEE Photon. Technol. Lett., Vol. 14 p. 1064, 2002.

Karlsson M., Nikolajeff F., Vukusic J., Martinsson H., Bengtsson J., and Larsson A., IEEE Photon. Technol. Lett. Vol. 15, p. 359, 2003(a).

Karlsson M., Nikolajeff F., Opt. Exp. Vol. 11, p.192, 2003(b).



Kawano K. and Kitho T., *Introduction to Optical Waveguide Analysis: Solving Maxwell's equation and the Schrodinger equation*. Wiley-Interscience, 2001.

King O., Erdogan T., Wicks G.W., Hall D.G., . Anderson, D. Costello, and M. J. Rooks, *J. Vac. Sc1. Technol. B* Vol. 10, 6, pp. 2974-2978, 1992.

Kim K., Lee S., Smolski O., and Delfyett P. J., *Opt. Lett.*, Vol. 29, p. 1273, 2004

Kipfer P., Collischon M., Haidner H., Schafer H., Schwider J., *Optik*, Vol. 112, p. 77, 2000.

Kjellberg T., Hagberg M., Eriksson N., and Larsson A., *IEEE Photon. Techn. Lett.* Vol. 5, p. 1149, 1993.

Kotani H., Yakushiji V, Harada V, Tsukamoto V, and Nishioka V, *J. Electrochem. Soc.* Vol. 130, p. 645, 1983.

Kristjansson S., Li M., Eriksson N., Hagberg M., Killius K.J., and Larsson A., *IEEE Photon. Tech. Lett.* Vol. 9, 4, pp.416-418, 1997.

Kuo Y. and Crowe J. R., *J. Vac. Sc1. Tecnol. A*, Vol. 8, p. 1529, 1990.

Kyser D. F. and Viswanathan N. S., *J. Vac. Sc1. Technol.* Vol. 12, p. 1305, 1975

Lang R.J., Hardy A., Parke R., Mehuys D., O'brien S., Major J., and Welch D., *IEEE J. Quant. Elec.* Vol. 29, pp. 2044-2051, 1993.

Larsson A., Eriksson N., Kristjansson S., Modh P., Uemukai M., Suhara T., and Nishihara H., Proceedings of SPIE conference on Testing, Packaging, and reliability of semiconductor laser IV, Vol. 3626, p. 190, 1999.

Liau Z.L., Walpole J.N., Missaggia L.J., and Mull D.E., Appl. Phys. Lett., Vol. 56, p.26, 1990.

Liao T., Sheard S., and Yang G., Opt. Comm. Vol. 137, p.1, 1997.

Liao T. and Sheard S., Appl. Opt. Vol. 37, p. 1776, 1998.

Lee J.W., Lim Y.T., Baek I.K., Yoo S.Y., Cho G.S., Jeoin M.H., Leem J.Y., and Pearton S.J., Appl. Surf. Sci. No. 233, p. 402, 2004.

Lee T.P., Burrus C.A. Jr, and Miller B.1., IEEE J. of Quant. Electron., Vol. 9, p. 820, 1973.

Lee T.P., Burrus C., Copeland J., Dentai A and Marcuse D., J. of Quant. Electron. Vol. 18, p. 1101, 1982.

Lehmann H. W. and Widmer R. , J. Vac. Sci. Technol. Vol. 15, p. 319, 1978.

Li M., Hagberg M., Bengtsson J., Eriksson N., and Larsson A., IEEE Photo. Tech. Lett., Vol. 8, 9, pp. 1199-1201, 1996.

Liau Z. L. and Walpole J. N., Appl. Phys. Lett., Vol. 46, p. 115, 1985.

Liau Z.L., Walpole J.N., Missaggia L.J., and D.E. Mull, Appl. Phys. Lett., Vol. 56, p. 1219, 1990.

Luo H., Kasunic K.J., Macomber S.H., Bedford R., Moloney J.V., and M. Fallahi, IEEE J. Select. Topics in Quant. Elect., Vol. 6, 4, pp.594-600, 2000.

Macomber S.H., Mott J.S., Schwartz B.D., Setzko R.S., and Logue J.E., Proceedings of IEEE-LEOS Annual Meeting, Vol. 1, pp. 117-118, 1996.

Maeda T., Lee J.W., Shul R.J., Han J., Hong J., Lambers E.S., Pearton S.J., Abernathy C.R., and Hobsn W.S., Appl. Surf. Sci. No. 143, p. 174, 1999.

Marciante J. R. and Agrawal G. P., IEEE J. Quantum Electron., Vol. 32, p. 590, 1996.

Martinelli R., Li J., Khalfin V., Braun A. M., Willner B. 1., Harvey M., Shellenbarger Z., and Abeles J. H., Proceedings of the OSA Conference on Laser Electro-Optics/International Quantum Electronics CLEO/QELS, paper CTuC1, 2004.

Martinsson H., Bengtsson J., Ghisoni M., and Larsson A., IEEE Photon. Tech. Lett. Vol. 11, 5, pp. 503, 1999.

Mehuys D., Parke R., Waarts R.G., Welch D.F., Hardy A., Streifer W., and Scifres D.R., IEEE J. Quant. Electron., Vol. 27, p.1574, 1991 (a).

Mehuys D., Hardy A., Welch D.F., Waarts R.G., Parke R., IEEE Photon. Technol. Lett., Vol. 3, p.342, 1991 (b).

Mehuys D., O'Brien S., Lang R.J., Hardy A., and Welch .F., Electron. Lett. Vol. 30, p. 1855, 1994.

Miyanaga S. and Asakura T., Appl. Opt., Vol. 20, p.688, 1981.

Modh P., Backlund J., Eriksson N., Bengtsson J., Kristjansson S., and Larsson A., Opt. Lett., Vol. 27, 8, p. 574, 2002(a).

Modh P., Backlund J., Bengtsson J., Larsson A., IEEE 18th International Semiconductor Laser Conference., 2002(b).

Modh P., Backlund J., Bengtsson J., Larsson A., Shimada N.,and Suhara T., Appl. Opt. Vol. 42, p.4547, 2003.

Moharam M.G., E.B. Grann and Pommet D.A., J. Opt. Soc. Am. A, Vol. 12, p. 1068, 1995.

Oehrlein G.S. and Williams H.L., J. Appl. Phys. Vol. 62, p. 662,1987

Ono Y., Kimura Y., Ohta Y., and Nishida N., Appl. Opt. Vol. 26, p. 1142, 1987.

Ou S.S., Jansen M., Yang J. J., Mawst L. J., and Roth T. J., Appl. Phys. Lett., Vol. 52, p.2085, 1991.

Parke R., Welch D., Hardy A., Lang R., Mehuys D., O'Brien S., Dzurko K., and Scifres D., IEEE Photonics Technology Letters Vol. 5, p. 297, 1993.

Pichthumani M., Hockel H., Mohammed W., and Johnson E.G., Appl. Opt., Vol. 41 , 29, pp. 6176-6181, 2002.

Pommet D. A., Moharam M. G. and Grann E. B., J. Opt. Soc. Am. A, Vol. 11, p. 1827 1994.

Raguin D.H. and Morris G.M., Appl. Opt. Vol. 32, p.2582, 1993.

Rakhshandehroo M. R. and Pang S. W., J. Vac. Sci. Technol. B, Vol. 14, p.612, 1996.

Rashed A.M., Williams K.A., Penty R.V., White I.H., Heard P.J., Day J.C.C., and Allen G.C., Allen, in *Digest of Conference on Lasers and Electro-Optics (CLEO/Pacific Rim)* (Optical Society of America, Washington, D.C.), p. 1092, 1999.

Reinhart F., Logan R. and Shank C., Appl. Phys. Lett., vol. 27, p. 45, 1975.

Reisman A. and Rohr R., J. of Electroch. Soc., Vol. 111, p. 1425, 1964.

Rastani K., Orenstein M., Kapon E., and Von Lehmen A. C., Opt. Lett., Vol. 16, p. 919, 1991.

Richter I., Sun P.C., Xu F., and Fainman Y., Appl. Opt. Vol. 34, p. 2421 (1995).

Rytov S.M., Sov. Phys. JETP Vol. 2, p.466, 1956.

Sacks Z.S., Kingsland D.M., Lee R., and Lee J.F., IEEE Trans. Anten. And prop., Vol. 43, p. 1460, 1995.

Scifres D. R., Burnham R.D., and Streifer W., Appl. Phys. Lett. Vol. 26, 2, p. 49, 1975.

Sheard S., Liao T., Yang G., Prewett P., and Zhu J., Appl. Opt. Vol. 36, p. 4349, 1997.

Sheard S. J., Liao T., Yang G., Prewett P. R., and Zhu J. G., in *Diffractive Optics and Micro-Optics*, Vol. 5 of 1996 OSA Technical Digest Series, Optical Society of America, Washington, D.C., p. 360, 1996.

Shiraishi K., Oyama N., Matsumura K., Ohishi I., and Suga S., J. of Lightwave Technol. Vol. 13, p. 1736, 1995.

Spaulding K. E. and Morris G. M., Appl. Opt., Vol. 30, p. 1096, 1991.

Spitzer W. G., and Whelan J. M., Phys. Rev. Vol. 114, p. 59, 1959.

Stegmüller B., Westermeier H., Thulke W., Franz G., and Sacher D., IEEE Photon. Tech. Lett., Vol. 3, No.9, pp. 776, 1991.

Streiffer W., Scifres D.R., and Burnham R.D., Appl. Phys. Lett. Vol. 40, No.4, p.305, 1982.

Suhara T. and H. Nishihara, Opt. Commun., vol. 19, no. 3, p. 353, 1976.

Suhara T., Okada K., Saso T., and Nishira H., IEEE Photon. Tech. Lett. Vol. 4, p. 903, 1992.

Stegmüller B., Westermeier H., Thulke W., Franz G., and Sacher D., IEEE Photon. Tech. Lett., Vol. 3, p. 776, 1991.

Streiffer W., Scifres D.R., and Burnham R., IEEE Journal of Quant. Electron., Vol. 12, p. 422, 1976.

Taflove A. and Hagness S.C., *Computational Electrodynamics, the finite-difference time-domain method*, Second edition. Chapter 3 pp.67-99. Artech House, Boston London, 2000.

Tamir T. and Peng S.T., Appl. Phys. Vol. 14, p. 235, 1977.

Tiberio R.C., Porkolab G.A., Johnson J.E., Grande W.J., L.C. Rathburn, E.D. Wolf, H.G. Craighead, R.J. Lang, A. Larsson, S. Forouhar, and J. Cody, J. Vac. Sci. Technol. B Vol.8, p. 1408, 1990.

Touam T. and Najafi S. 1., Appl. Opt. Vol. 36, p. 2554, 1997.

Toyota H., Yu W., Okano M., Omori S., and Yotsuya T., in OSA Trends in Optics and Optoelectronics (TOPS) Vol. 75, Diffractive Optics and Micro-Optics, OSA Technical Digest, Washington DC (2001), p.222.

Turner J.J., Chen B., Yang L., Ballantyne J.M., and Tang C.L., Appl. Phys. Lett., Vol. 23, p. 333, 1973.

Unaxis Inc., Chip Magazine, No. 30, 2003.

Vaissié L. and Johnson E. G., Opt. Eng. Vol. 41, p. 1821, 2002.

Vaissié L., Mohammed W., and Johnson E. G., *Opt. Lett.*, Vol. 28, p. 651, 2003

Vaissié L., Smolski O., and Johnson E.G., Submitted to *Optics Letters*, 2004(a).

Vaissié L., Smolski O, Metha A., and Johnson E. G., Submitted to *IEEE Photonics Technology Letters*, 2004(b).

Walker C.L., Bryce A.C., and Marsh J.H., *IEEE Photon. Techn. Lett.* Vol. 14, p. 1391, 2002.

Walpole J.N., Donnelly J.P., Taylor P.J., Missaggia L.J., Harris C.T., Bailey R.J., Napoleone A., Groves S.H., Chinn S.R., Huang R., and Plant J., *IEEE Photon. Technol. Lett.*, Vol. 14, p. 756, 2002.

Welch D. F., Mehuys D., Parke R., Waarts R., Scifres D. and Streiffer W., *Electron. Lett.* Vol. 26, 17, p. 1327, 1990 (a).

Welch D.F., Parke R., Hardy A., Waarts R., Streiffer W., and Scifres D.R., *Elect. Lett.* Vol. 26, 11, p. 758, 1990 (b).

West L. C., Roberts C., and Piscani E., in *Integrated Photonics Research Technical Digest*, Optical society of America, 1996.

Westerman R. and Johnson D., *Chip No.5*, p.16, 2001.

Wong V. V. and Swanson G. S., *Appl. Opt.* Vol. 32, p. 2502, 1993.



Wu C., Svilans M., Fallahi M., Makino T., Glinski, J., Maritan, C., and Blaauw, C., *Elect. Lett.* , Vol. 27, 20, 1991.

Yariv A, *IEEE J. Quant. Electron.*, Vol. 9, p. 919, 1973.

Yee K.S., *IEEE Trans. Antennas and Propagation*, Vol. 14, p. 302, 1966.

Yoda H. and Shiraishi K., *J. of Lightwave Technol.* Vol. 19, 12, pp. 1910-1917, 2001.

Young R. J., Cleaver J. R. A. and Ahmed H., *Microelec. Eng.*, Vol. 11, p. 409, 1990.

Zhang H.L., Luo G. P., Seetharaman A., Johnson P., Le H. Q., in *Digest of Conference on Lasers and Electro-Optics (CLEO/QELS)* (Optical Society of America, Washington, D.C.), paper CMZ4, 2004.

Zhao Y., Han W., Song J., Li X., Liu Y., Gao D., and Du G., Cao H. and Chang R. P. H., *J. of Appl. Phys.* Vol. 85, p. 3945, 1999.

Zory P. and Comerford L., *IEEE J. Quant. Electron.*, Vol. 11, p. 451, 1975.